Mathematical modelling to predict exclusion and safety zones around LNG terminals

Alan Esteves, PhD (Senior CNPq Researcher of the Mechanical Engineering Department at PUC-Rio)
José Alberto Parise, PhD (Professor of the Mechanical Engineering Department at PUC-Rio)
Antonio Cordovil (Chemical Engineering Department at PUC-Rio)
Edwin Campos, MSc (Mechanical Engineering Department at PUC-Rio)
Issue: November 26, 2017

1. Background

Liquefied natural gas (LNG) is natural gas (NG) cooled to the point where it liquefies, which takes place at -162 °C at atmospheric pressure. The liquefaction reduces the volume of the gas approximately 600 times, depending on the molar mass of the gas (which is typically a mixture of gases). This process is often the most economical way to store and transport gas over long distances – gas pipelines are more feasible for shorter distances. Liquefaction makes it possible to move NG among continents in dedicated vessels (carriers) built specially for this purpose (Blackwell and Skaar, 2009).

To make this possible, energy organizations have built highly interconnected and dependent operations, forming the so-called 'value chain' (or 'chain-of-supply'), as depicted in Fig. 1.

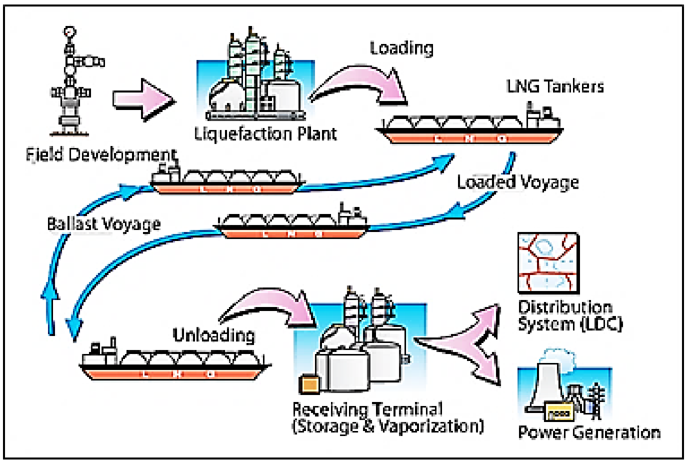

Fig. 1 – LNG value chain – from the well to the consumer
Available: https://www.ihrdc.com/els/po-demo/module15/mod_015_02.htm Access: 23 Mar 2016

In this chain, the associated gas produced in offshore fields up to 200-250 km from the coast, goes to a separation from the oil and water in a rig or FPSO[1] unit. In that unit, the hydrates eventually formed are withdrawn from the gas, which is then dried, compressed and typically piped to facility on the coast. In an onshore NGPU[2] the gas is processed primarily to separate 'heavier' fractions (C_2^+) and liquefied in another facility usually on the same site, called 'baseload plant'[3]. There, the liquefied gas is stored usually in atmospheric and cryogenic dome tanks. If the field is of non-associated gas, and distant 200-250 km or more from the shore, the gas is processed offshore in an FLNG[4] vessels, stored in the LNG tanks of this floating unit and offloaded to a carrier docked ship-to-ship[5], in tandem[6] by means of cryogenic hoses or cryogenic booms (boom loading system) (Patel, 2009).

The LNG industry has operated with an excellent safety record. However, LNG stakeholders recognize that some incidents involving LNG are possible, including potential terrorist actions. Despite of all the efforts/resources applied to make this industry a record maker in safety/security matters; it is still it is possible to have accidents with dangerous outcomes.

The objective of the work present here is to provide a tool to help reduce subjectivism in the decision making process regarding the location of LNG terminals, providing a solid foundation for the decisions. An exhaustive research work through six decades of the open literature showed no evidence that all relevant issues had been incorporated and integrated into a one single model (Esteves and Parise, 2011, 2013a,b). Giving a step ahead in this direction, the present work starts at and expands from previous results found by Esteves (2010), which connected pool spread to pool fire modellings.

[1] *Floating, Production, Storage and Offloading.*
[2] *Natural Gas Processing Unit*.
[3] Plant of great capacity, usually above 2 MTPA (*millions of tonnes per annum*).
[4] *Floating Liquefied Natural Gas*.
[5] Portside or starboard.
[6] In line, usually bow-to-bow.

2. Executive summary

Keywords: Mathematical modelling; Prediction; Exclusion and safety zones; LNG terminals

This research report innovates coupling the spill model from Fay/MIT (2003) to a non-premixed turbulent combustion pool fire from Raj/TMS (2007). We considered three different zones of a fire column with the surface emissive power (SEP) varying with the height of the fire solid flame. Our model uses semicircular pool spill/spreading of LNG onto the sea, as presented by Fay/MIT (2003), in which the fire plume tilts by the action of wind. However, our numerical results consider pool diameters varying from 10 to 500 m, which is a wider range when compared to similar models.

During the benchmarking of our model, against previous evaluations, we adopt tear diameters of 1 m and 5 m. We assume that an LNG carrier has its hull stricken by another ship during loading/unloading operation at a LNG coastal cryogenic terminal. Five additional models are coupled to calculate the pool fire SEP. The first is about the configuration factor between the tilted flame and the potential damage targets (individuals and/or assets) near the terminal. Second, deals with the intervenient atmospheric transmissivity that attenuates the thermal flux in its path length. The following considers the thermal flux emitted by the pool fire and the correspondent downwind hazard distances in comparison with international regulation, in order to define the terminal location. This fourth model refers to the percent vulnerabilities of individuals and assets, corresponding to each of the incident thermal fluxes considered. In addition, the fifth is about the effective time to escape from the considered thermal fluxes to search for shelter.

We compared our work against previous models. We ran our model with input data from ABS (2004), FERC (2004) and SNL (2011), and our results matched. In the same fashion, partial calculations of intermediate steps of our model when compared to the results of other references in the literature, e.g., Fay (2003), Raj/TMS (2007a,b; 2006), ABS (2004), FERC (2004), Hightower (2007), SNL (2004, 2008a,b, 2011), Mizner and Eyre (1982), Raj at al. (1979), presented equally good predictions.

To the author's knowledge, the existing literature does not provide a robust set of six models integrated into a single computational tool. Thus, our integrated model facilitates LNG siting studies and helps reduce subjectivism in the decision siting studies and helps reduce subjectivism in the decision making process by integrating the analysis, from the tear to the downwind distances.

We use the platforms EES®, Mathtype6.9® and Microsoft Advanced Excel® to write, integrate and systematize all the equations of the present work. The objective is to couple all calculations in an only one model of low computational cost to facilitate applications in the LNG industry. This research addresses the phenomenological fundaments, the mathematical modelling of pool fires and the thermal radiation hazards emitted by a fire of an LNG release.

It includes a review of modern literature on assessment of experimental methodologies, covering the following topics:

(i) The fluid mechanics of the pool spill and spreading. That means, the LNG release rate disgorged from a tear perpetrated against hulls of LNG carriers moored at a terminal and the subsequent spread of an unconfined pool of a cryogenic fluid onto a sea of quiescent waters;
(ii) Vapor generation due to unconfined LNG spills on water;
(iii) Subsequent pool fire of turbulent diffusion combustion;
(iv) Thermal radiation emitted by pool fires on water;
(v) Propagation of the radiation fields interacting with atmospheric transmissivity and striking on vulnerable resources surrounding the LNG terminal;
(vi) Prediction of downwind distances to support decision making aiding to define exclusion zones around these terminals;
(vii) Prediction of the effects of thermal radiation and vulnerability (%) of resources (people and structures) struck by these radiations.

Obviously, the approach presented here provides only estimates of the potential consequences associated with spills of LNG. Actual incidents may vary in nature due to variability in numerous assumptions used during the modeling.

When one envisages large releases from LNG carriers, some important issues arise. To name a few, we could cite:

- In the open literature, until now and to the our best knowledge, no release model was found to describe the actual structure of an LNG carrier; multiple barriers caused by cargo tanks and/or double hulls provided by modern ships;
- Even considering quiescent waters of a LNG terminal, no reliable model was found to compute the effects of currents and/or waves on a large pool of the cryogenic spreading on the sea;
- Only a few experimental tests exist on industrial scale. One can cite China Lake (Cal.), Montoir (France) and Albuquerque (N. Mex.), resulting in a relative scarcity of data to validate models of LNG spills on water; furthermore, to date, no experimental data exist, for spills/pool fires with the diameter range as big as the ones considered in the present work (10-500 m).

When dealing with limitations that exist in the models used in this report, we followed standard industry practices of adopting conservative assumptions. More research and more large-scale experiments are still necessary to develop and validate models that are more refined.

When applying the results and findings of the present work, one should take care to consider specific and actual local/atmospheric conditions. This work did not consider any sequential/natural order or chronology of the events that could lead or build up to an incident or an eventual outcome; neither considered their occurrence probabilities. Consequently, this report does not quantify a measure of risk to the public. Therefore, a thorough risk assessment would be necessary in order to consider both the frequencies and consequences of hazardous events of the different scenarios considered. Given the uncertainties and the

conservatism of the models found in the literature, it should not be assumed that the levels of hazards found with this report could be considered as assured outcomes of LNG vessel releases.

This report centers the present state of the science for modeling potential releases from LNG carriers, but this state nevertheless is in a continuous evolution. There is room for debates and sometimes controversies concerning the most appropriate way to model possible outcomes of incidents. That means that newer and better models/approaches there will exist in the times to come. However, practical and defendable guidance are necessary to aid, as much as possible, the best understanding of the current scientific state. For events with intrinsic limitations, reasonable decision-making criteria are necessary, and the present work aims at providing models/approaches that adds subsides to terminals siting decisions.

While studying the results of this report, readers should keep in mind the following key points (ABS, 2004; FERC, 2004):

- Risk perception and risk tolerability are complex matters. Public, individuals or groups of individuals perceive and react differently to risk threats, which depend on a series of factors/circumstances. In a broad sense, it represents a subjective issue with no clear "right" or "wrong" answers. Even with the extremely detailed information available, it is common for different individuals to have different behaviors. This report does not consider any judgment of value on what or how public should or should not tolerate the risks;
- Risk context demands more information than the evaluation of consequences only. At least three aspects are necessary to define the risk question: (i) what would be necessary to make a process go wrong. (ii) If it happens, how great could the expected consequences be? (iii) How likely are the losses expected to occur? This research report intends to focus on the second aspect only. Decision making about a given accident scenario should consider both the expected frequency with which such scenario may occur and the potential consequences thereof. Authorities that strongly regulate LNG activity (carriers, terminals and associated equipment and installations) Layers of protection and redundancies are required by in order to prevent/avoid unexpected accidents or terrorism threats. Similarly, the present document does not address these concerns, which are important to the complete risk issue;
- Models are just an approximation of reality - Models/approaches represent a coherent set of tools for decision-making; however, they carry intrinsic uncertainties, and their application must be consistent with premises, governing assumptions and constraints. In some cases, the industry and scientific community's experience and comprehension of fundamental phenomena are more important than the scientific knowledge used to describe the phenomena analytically;
- Models are means to aid decision making – The central point is to provide plausible information regarding a LNG facility siting. Models do not make decisions for players; they must integrate and consider all information on many different aspects of the problem to form a consistent tool basis for this process.

3. Structure and methodologies used in the present research report

This report presents and discusses the research, modelling results proposing an alternate approach to calculate the surface emissive power of the flame.

Chapter 4 describes the modelling of the LNG depleting/leaking from a carrier cargo tank, its spreading onto a sea of quiescent waters of a terminal. In this scenario, the moored carrier hull can be stricken, forming semicircular pools (transited to circular) around the tear. Chapter 5 models the pool fire with non-premixed turbulent combustion, providing four governing parameters of a pool fire: combustion Froude number, fire column (L_V/D_{pci}), drag and tilt.

Chapter 6 calculates the flame surface emissive power and the subsequent phenomena. After the generation of the thermal flux, it interacts with the atmospheric air, scatters, abating its strength before striking on targets. Depending on the relative positions of flame and targets, they will receive different fluxes due to the air transmissivity. This chapter also presents a discussion about the coupling of these parameters.

Chapter 7 models the radiation effects on individuals and assets around an LNG terminal. It predicts exposure duration, reaction and escape times for each level of vulnerability.

Chapter 8 deals with the evaluation of exclusion, safety and security zones, as well as the selection of levels of thermal radiation. The criteria to define exclusion zones consider the selection of radiation levels, human exposures and effects on structures. It presents highlights on the American and European LNG standards. This chapter discusses siting criteria and exclusion zones, according to USA standards and regulations. In the same fashion, it presents the application of the Canadian Standard Z276-01 and Nova Scotia LNG Code of Practice.

Chapter 9 discusses thoroughly the results of the pool spill/spreading and combustion. The computational program developed in this report calculates the incident thermal flux and vulnerabilities at a given downwind distance (path length). If the thermal flux surpasses prescribed values, using an iterative process it is possible to determine new downwind distances, until it matches those requirements. The chapter covers comparisons with literature for 1 m² and 5 m² tears on the carrier hull, with membrane carriers of 125,000 and 265,000 m³.

Chapter 10 models the downwind distances. Using the same input data, we compared our results with the results of ABS (2004), FERC (2004), and SNL (2004, 2008, 2011). Our work matched fairly the corresponding ones obtained by the three Organizations. We also present a supplementary comparison of this report, adopting a time average *SEP*, to those found with constant *SEP* used by ABS (2004) and FERC (2004) (265 kW/m²), SNL (2004,2008) (220 kW/m²) and SNL (2011). (Average: 286 kW/m², with parametric variation between 239 and 337 kW/m²). With time-average *SEP*s of 111 kW/m² (tear of 1 m) and 106 kW/m² (tear of 5 m), the present work found downwind distances about half of those found by the three Organizations.

Chapter 11 discusses the hazards and impacts of the outcome effects on external public and resources. Chapter 12 presents a general guidance about risk management for water LNG operations. Chapter 13 closes the Report dealing with vulnerability analysis for lethality with protection. The results are plot on satellite photos for the concentric circles of the downwind distances, corresponding to the thermal fluxes 38, 25, 12 and 5 kW/m² for tears of 1 and 5 m, and the respective effective times to seek shelter.

4. Mathematical model for the cargo tank depletion and pool spill/spreading

4.1. Introduction

The spill/spreading is modeled with conservative integral formulation, having as main parameters the tear area, the maximum area of the spilled pool and the discharge and vaporization times of cryogenic at sea. The flow assumes tears areas of 1-100 m², consistent with current industry practices, and considers the forming of semicircular pools around vessels hulls, having the tears as its center point.

The modeling of the thermal plume includes circular pools (converted from semicircular ones based on the mass conservation) with diameters between 10 m and 500 m, from bow to stern, consistent with the lengths of the current ships. The combustion model considers combustion zones and the intermittence of the thermal plume.

The tool also provides a consistent and robust framework for the development of dimensionless scale parameters, allowing the user to correlate and extrapolate the length of the visible plume, with the thermal plume's tilt and drag, with its surface emissive power and mass flow rate of vaporization of the cryogenic fuel within the pool. Thus, the model also calculates: (i) the axial variation of emissive power with the height of the visible plume. (ii) the fuel burning along the 'light' zone at the base of the fire. (iii) the thermal radiation transport within the fire column, emitted from gray gases and soot particles in the combustion zone, considering the emission and absorption in the optically thin and thick regions of the thermal plume (Esteves, 2011, 2010).

For such a purpose, we supposed that just after the beginning of the spill/spreading, an immediate pool fire would start, fed by the flame's combustion due to turbulent diffusion. The geometry of L_v/D_{pci}, i.e., the ratio between the length of the visible fire column and the diameter of the circular pool, which supports combustion of this column in the sea and their average radiant surface emissive power, are then modelled varying with the height over the thermal plume axis.

Time average surface emissive power of fire column generates radiation fields. They propagate, attenuates in the environment with full hemispherical transmissivity of the atmosphere. To spread in the atmosphere the heat flow is supposed to strike on vulnerable resources around the marine terminal, located at a certain distances from the tear perpetrated on the side hull of the struck carrier.

The maximum acceptable of radiation levels are important since they define the location of vulnerable resources in relation to a LNG terminal. They also provide subsides for eventual compensatory measures (trade-offs) that may be or not adopted by the authorities and communities to mitigate the effects of this radiation.

Some international standards[7] establish these maximum radiation levels. Institutions and laboratories of international research, TNO, SNL, HSE, to name just a few, developed experiments and acquired data from past accidents to describe the dose-response relationship in terms of percentage of the vulnerable resources affected. That is, to a level of radiation emitted by the flame (dose), one can determine the percentage of the affected resource (response) to first-degree, second degree burns and lethality. Therefore, the present model intends to collapse all of these parts in only one tool aiming assessing these zones.

4.2. The physics of the cargo tank depletion and pool/spreading

In the model presented in this document, we assume that the tear penetrates the inner and outer hulls, all layers of insulation, and the cargo tank itself. These assumptions and others presented herein are consistent with the best practices in modelling LNG spills on water. They are necessary because of several issues that still are under full research and modelling now. They are:

- In transoceanic vessels, the transportation/storage of LNG is with insulated and dedicated cargo tanks installed within hulls. The current best practice in modelling spills from these similar vessels considers that a tear severs the inner and outer hulls, the layers of insulation, and the cargo tank itself. There are no detailed models that take into account releases through multiple hulls and/or the effect of the released fluid into the spaces between the hulls;
- The tear is assumed to happen just above the sea water line;
- Neither LNG nor seawater will be spilled into the void spaces between both hulls;
- The bottom edge of the tear is supposed to be coincident with the sea water line, avoiding that the submerged edge may cause water entering the tank or the LNG leaving the tank through the hole, freezing the water rapidly; if that occurs, there will be heat transfer from water, vaporizing more LNG inside the tank. This may result in pressure increase in the tank, thereby expelling more LNG (and water that entered the tank) out of the hole;
- The gravity drives LNG outflow from the tear, and it is time dependent. Therefore, the flow rate decreases as the height of the liquid above the tear decreases, ceasing when the level of the liquid reaches the lower edge of the tear. We assume a conservative approach considering the LNG flow rate as constant and equal to the flow rate at the beginning of the outflow, i.e., when $t = 0$;
- A physical phenomenon may occur with large diameter tears: the liquid deployment rate may be higher than the vapor generation rate inside the tank, or there is admission of air at a given rate into the tank through vacuum relief valves. Thus, partial vacuum may be created within the tank, reducing the deployment rate and even causing damages to the cargo tank, if not designed for vacuum conditions;

[7] (IMO SIGGTO, MARAD, USCG, USA, Canada, Europe, Japan, etc.

- In case of large diameter tears, there will be no liquid deploying with rates above that of vapor generation inside the tank, nor that of air being admitted into the tank through vacuum relief valves creating vacuum within the tank;
- Since the space between the double hulls is not here taken into consideration, the double hull is assumed to be compacted in only one, the outflow rate may be overestimated;
- When the tear happens below the sea water line, the physics is more complicated, this explains why this hypothesis has not been taken into consideration in the scope of the present modelling, providing that:
  - Up to a certain level below the water line, the cryogenic tank pressure will be higher than the water pressure, so LNG will flow outwards from the tear and vaporize vigorously by the time it gets in contact with the water;
  - If the tear takes place deeper from this line or when the LNG within the cargo tank depletes more, the tank and water pressures will match. In this case, water may enter through the hole. The water may freeze rapidly, and the heat transferred from water would vaporizes more LNG (and possibly force the water that entered the tank) out the hole;
  - Another possibility is for both LNG/seawater spilling into the void spaces between the hulls.

4.3. Semicircular pool spill/spreading

Based on Esteves and Parise (2013a,b) and Esteves (2010), this work adopts the formal protocol of MKOPSC (2008). It is representative and robust, since it compares focus, formulation, confidence interval, limitations, results, accuracies, strengths and weaknesses.

Fay's (2003) orifice model proved to be the most suitable and reliable for the present purposes of LGN industry. It covers whole hull areas in today's LNG carriers from 1 to 100 m². It expresses the maximum pool area and the vaporization time as functions of only one dimensionless flow parameter, $0 \le \Upsilon \le +\infty$ which depends on $\langle \dot{y} \rangle$.

The model considers the carrier geometric dimensions, the heat transfer process, and only one dimensionless empirical constant, ß, which simplifies the modeling. Fay's (2003) model is in accordance with the reality of current LNG carriers, which capacities vary from 125,000 to 265,000 m³ (SNL, 2008a,b). Figure 2 presents the geometry sketch of the damaged LNG carrier.

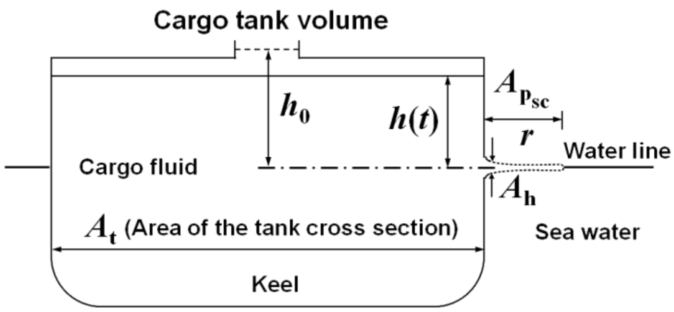

Fig. 2 - Membrane or prismatic cargo tank of a LNG carrier - Adapted from: Fay (2003) and Esteves (2010)

4.4. The spill/spreading fundamental governing equations

Slattery (1972) describes the conservation of mass and linear momentum by Equations (1) and (2): such as

$$\underbrace{\dot{M} \equiv \frac{D}{Dt} \iiint_{V_{(m)}(t)} \rho dV_{(m)}(t) = 0}_{\text{Rate of change of material particles accumulation within the material control volume}} \tag{1}$$

$$\underbrace{\frac{D}{Dt} \iiint_{V_{(m)}(t)} \rho u_i dV_{(m)}(t)}_{\text{Rate of change of the linear momentum}} = \underbrace{\iiint_{V_{(m)}(t)} \rho f_i dV_{(m)}(t)}_{\text{Resultant of the body forces}} + \underbrace{\iiint_{V_{(m)}(t)} \frac{\partial}{\partial x_j} T_{ij} dV_{(m)}(t)}_{\text{Resultant of the surface forces}} \tag{2}$$

The Navier-Stokes equation governs the conservation of linear momentum of a cryogenic fluid material particle following the flow movement in the pool. The fluid is assumed to be Newtonian with constant properties (ρ, λ and μ), and with pressure P at a distance χ . Using indicial notation one describe the Eq. (2) as

$$\underbrace{\frac{D}{Dt}(\rho u_i)}_{\substack{\text{Total acceleration}\\ \text{of the fluid}\\ \text{material particle}\\ \text{per unit of volume}}} = \underbrace{\rho f_i}_{\substack{\text{Body forces}\\ \text{per unit of}\\ \text{volume}}} - \underbrace{\frac{\partial P}{\partial x_i}}_{\substack{\text{Pressure forces}\\ \text{per unit of}\\ \text{volume}}} + \underbrace{\left(\lambda + \tfrac{1}{3}\mu\right)\frac{\partial}{\partial x_j}\frac{\partial u_i}{\partial x_i}}_{\substack{\text{Maximum net convective}\\ \text{effects experimented}\\ \text{by the the fluid viscosity}\\ \text{per unit of volume}}} + \underbrace{\mu \frac{\partial^2 u_i}{\partial x_i^{\,2}}}_{\substack{\text{Viscous forces}\\ \text{per unit of}\\ \text{volume}}} \tag{3}$$

A boiling LNG pool is insulated from the sea substrate by a thin film of LNG vapor (due to the Liedenfrost effect) of much lower viscosity than that of water or LNG (Fay, 2007). Therefore, the spread of an evaporating LNG pool is essentially an inviscid flow with nearly frictionless motion (Fay, 2003). Thus, $\lambda + \frac{1}{3}\mu \approx 0$ in the convective term, as well as the viscosity diffusion effects are negligible, so $\mu\left[\nabla^2 \mathbf{u}\right] \equiv \mu\left(\partial^2 u_i / \partial x_i^2\right) \approx 0$. The emerging cryogenic cargo fluid floats over the seawater surface, and forms a semicircular pool that spreads horizontally centered at the hull tear. A subsequent and immediate ignition of a non-premixed pool fire is supposed to occur. Hence, the effects of the body forces will barely have enough time to occur and, therefore, one can consider that $\rho f_i \approx 0$. Under this circumstance, Eq. (3) becomes $-D/Dt(\rho u_i) = \partial P / \partial x_i$.

The cargo tank deployment is supposed to take place at atmospheric pressure without significant variation as the pool spreads, hence, $\partial P / \partial x_i \approx 0$. Considering the momentum conservation, the Euler equation applies along a radial streamline (Fay, 2003,2006,2007). At each point along of this line, to which u_i is tangent, the total acceleration of a fluid material particle, Du_i / Dt , spreads it within the pool, following the motion. The Euler's material acceleration describes this movement written as

$$a_i \hat{\mathbf{e}}_i = \frac{D}{Dt}(\rho u_i)\hat{\mathbf{e}}_i = \frac{\partial u_i}{\partial t}\hat{\mathbf{e}}_i + u_i \hat{\boldsymbol{\delta}}_{ij}\frac{\partial u_k}{\partial x_j}\hat{\mathbf{e}}_k = \frac{\partial u_i}{\partial t}\hat{\mathbf{e}}_i + u_j \frac{\partial u_i}{\partial x_j}\hat{\mathbf{e}}_i \Rightarrow \frac{Du_i}{Dt} = \frac{\partial u_i}{\partial t} + u_j \frac{\partial u_i}{\partial x_j} \tag{4}$$

where $\hat{\boldsymbol{\delta}}_{ij} \equiv \left\{\delta_{i,j}\right\}$ is the second order tensor of the Kröenecker's delta. For this sort of nearly frictionless flow, Fay/MIT's (2003) model considers that it is possible to have an exact solution of the Euler's equation along a radial streamline. In cylindrical coordinates, assumes that a fluid material particle spreads horizontally and it is in the position $r = |\mathbf{r}|$. It is supposed to have a movement at a fixed radial speed starting at the origin of the spill, and the equation that describes this movement is given in cylindrical coordinates by (Fay, 2003,2006,2007; Hoult, 1972a,b):

$$a_i = \frac{Du_i}{Dt} = \frac{\partial u_i}{\partial t} + u_j \frac{\partial u_i}{\partial x_j} \quad \Rightarrow \quad \frac{Du}{Dt} = \frac{\partial u}{\partial t} + u\frac{\partial u}{\partial r} \quad \text{(on the streamline)} \tag{5}$$

Hoult (1972a,b) developed a self-similar solution to Euler's equation along a radial streamline with mass conservation for inertial-gravity spread, in terms of a dimensionless similarity variables, as a function of the independent variables, as follows (Fay, 2007):

$$\frac{\partial u}{\partial t} + u\frac{\partial u}{\partial r} + g\Delta \frac{\partial \bar{\delta}}{\partial r} = 0 \tag{6}$$

MKOPSC (2008) assumes that $\bar{\delta}$, the average thickness (m) of the pool, is a function of time, and Fay (2003) considers as it having an average value. Although the LNG pool continues to burn with any thickness (Lehr and Simecek-Beatty, 2004) until all the fuel is exhausted (Johnson and Cornwell, 2007), the thickness is not constant. For a LNG slick, the length scale is tiny (mm) when compared to a semicircular pool with a radius of 339 m mentioned by Fay (2003), suggests that $\partial \bar{\delta} / \partial r \approx 0$. Combining Eqs (5) with (6) gives the deceleration (m/s²) of a material particle where the energy of the fluid deployed from cargo tank is integrally transferred to the pool spreading movement on the sea, so Euler's equation can be written as (Fay, 2007):

$$\frac{Du}{Dt} \equiv \frac{\partial u}{\partial t} + u\frac{\partial u}{\partial r} = 0 \quad \Rightarrow \quad -\frac{\partial u}{\partial t} = u\frac{\partial u}{\partial r} \tag{7}$$

In other words, this equation considers then that the total acceleration of a fluid material particle, Du/Dt along the streamline is equal to zero.

4.5 The physics of the model and its equations

Besides Eq. (7), Fay (2003) defines a time scale (t_d) that determines the time elapsed of the outflow from the cargo tank tear. The orifice model of Fluid Mechanics state that the magnitude of the outflow velocity through the tear at or close to the water line is determined as a function of $\sqrt{g h_0}$ (Woodward and Pitblado, 2010; Mannan et al., (2008). Thus, the outflow volumetric flow rate of the spilled LNG is given by $\sqrt{g h_0}\, A_\mathrm{h}$ which multiplied by the discharge time, t_d gives a volume that, from the mass conservation, must be equal to the volume discharged $V_0 = A_\mathrm{t} h_0$. The initial value of $h(t)$ inside the cargo tank is h_0 , and both of them counted above the waterline, as depicted in Fig. 2. When a rupture occurs in the carrier hull, the carrier is supposed to be loaded at full capacity, operating in quiescent waters of a terminal. The whole cargo holds in a carrier equipped with membrane or prismatic cargo tanks of constant cross sectional area, A_t .

In the present formulation, we are assuming a number simplifying hypotheses, neglecting the occurrence of some phenomena. One can mention: (i) vacuum pressure inside the cargo tank, usually less than ≈ 115 kPa (Qiao et al., 2006);(ii) vacuum breaker and air entering the cargo tank through the breach; as well as (iii) RPTs, as a result of cryogenic thermodynamic flash due to eventual water entrance into the cargo and ballast tanks during the spill.

The MKOPSC (2008) considers the effects of cargo tank pressure as of low to medium importance on the prediction of liquid outflow from the ship. Otherwise, this work considers it as being altered by the potential pressure changes associated with the LNG release, flash, heat ingress through the inner tank walls, etc. (Woodward and Pitblado, 2010; MKOPSC, 2008; Lehr and Simecek-Beatty, 2004). Therefore, it can be expressed as:

$$t_\mathrm{d} \approx \frac{A_\mathrm{t} h_0}{\sqrt{g h_0}\, A_\mathrm{h}} = \left(\frac{A_\mathrm{t}}{A_\mathrm{h}}\right)\sqrt{\frac{h_0}{g}} \tag{8}$$

The pool of LNG evaporates by a boiling and/or fire processes and the deployment cannot take place in a time shorter than t_d. The express the tank depletion we express the vaporization (or regression) velocity $\langle \dot{y} \rangle$, as a function of the mechanisms that vaporizes the cryogenic fluid. Fay (2003) defines a set of equations to calculate the pool radius varying with the discharge time from the carrier cargo tank, the subsequent evaporation of the LNG volume, V_p , spilled during the pool formation and the maximum semicircular pool area, $A_{\mathrm{p_{sc}}}^{\max}$, leading to

$$-\left[\frac{\partial}{\partial t}\left(h A_\mathrm{t}\right)\right]_{A_\mathrm{h},\langle \dot{y} \rangle} = \sqrt{2 g h}\, A_\mathrm{h} \tag{9}$$

$$\left(\frac{\partial V_\mathrm{p}}{\partial t}\right)_{A_\mathrm{h},\langle \dot{y} \rangle} = \sqrt{2 g h}\, A_\mathrm{h} - \langle \dot{y} \rangle A_{\mathrm{p_{sc}}}^{\max} \tag{10}$$

$$\left[\frac{\partial\left(\pi R_\mathrm{p}^{\,2}/2\right)}{\partial t}\right]_{A_\mathrm{h},\langle \dot{y} \rangle} = \left(\frac{\partial R_\mathrm{p}}{\partial t}\right)_{A_\mathrm{h},\langle \dot{y} \rangle} = \left(\frac{ß}{\pi}\right)\sqrt{2\pi g V_\mathrm{p} \Delta} \tag{11}$$

Equations (1), (2), (9), (10) and (11) define, therefore, the time line of the discharge from the carrier cargo tank and the subsequent formation and vaporization of the semicircular pool. For the current carriers, the cargo tank geometry described in Fig. 2 and its cross sectional area can be estimated as (Fay, 2003)[8]. With the equations (12)-(15) correlating density effects and the carrier geometry, one has:

$$\Delta = \frac{\rho_\mathrm{w} - \rho_\mathrm{l}}{\rho_\mathrm{w}} \tag{12}$$

[8] From this time forward, we will write the units in the S.I. system.

$$V_0 = A_t h_0 \tag{13}$$

$$CTV = \frac{CVC}{NT} \tag{14}$$

$$A_t = 0.5192\left(CTV/DR\right) \approx 0.52\left(CTV/DR\right) \tag{15}$$

Fay (2003) also proposed some input data, such as an axi-simetrical pool spread dimensionless parameter, $ß = 4/\sqrt{3} = 2.31$; experimental vaporization velocity $\langle \dot{y} \rangle = 0.000667$ m/s; the ship draft $DR = 11.8$ m as the distance between the ship's keel and the liquid surface; the capacity of cargo vessel $CVC = 125{,}000$ m , $CTV = 25{,}000$ m for each one of the $NT = 5$ cargo tanks; h_o = 13 m and Δ = 0.58. Fay (2003) developed another dimensionless flow parameter, Υ, correlating $ß$, Δ, $\langle \dot{y} \rangle$ and the cargo tank geometry, h_o, A_t and A_h as well:

$$\Upsilon = ß\sqrt{2\pi\Delta}\,\langle \dot{y} \rangle \sqrt{\frac{h_0}{g}} \cdot \frac{A_t^{3/2}}{A_h^2} \tag{16}$$

The parameter Υ varies in the interval $0 < \Upsilon < +\infty$ defining the LNG flow through the tear on the ship's hull and the pool spreading in the transient and quasi-steady regimes. Fay (2003) developed some correlations for this parameter and some remarkable values are discussed:

- If $\Upsilon >> 1$, i.e., for small orifice $\left(A_h << 1\text{m}^2\right)$, during a very small interval, the flow through the tear starts as transient, stabilizes as quasi-steady state, and continues so until the entry of LNG into the pool balances the pool evaporation. During this period, the pool shrinks almost linearly with time, as confirmed by Johnson and Cornwell (2007), and reaches zero when ceases the tank deployment;
- If $\Upsilon \to \infty$, the orifice size approaches zero $\left(A_h \to 0\right)$, the transient phase of the flow becomes negligible and the quasi-permanent flow takes most of the time, except in the beginning, when the outflow is established;
- As Υ decreases, the parameter approaches a critical value, $\Upsilon_{crit} = 1.784$, and when the dimensionless time equals $\sqrt{2}$, the transient phase takes all outflow duration time;
- If the dimensionless time is much lower than $\sqrt{2}$, the governing equations need to be integrated numerically;
- If , $\Upsilon << \Upsilon_{crit} = 1{,}784$, the governing equations need to be integrated as well;
- If $\Upsilon << 1$, i.e., for very large tears on the ship's hull, $\left(A_h >> 1\text{ m}^2\right)$, the outflow takes place very rapidly, and the pool spreads and vaporizes (Fay, 2003), reaching a maximum value, shrinking monotonically from this maximum forward.

Fay (2003) published some values of Υ, such as $\Upsilon \gg 1$, $\Upsilon = 30$, $\Upsilon = 10$, $\Upsilon = 3$, $\Upsilon = 1.784$, $\Upsilon = 1$, $\Upsilon = 1/3$, $\Upsilon \ll 1$, correlating them to the dimensionless variables of the flow: dimensionless maximum area of the pool, $a^{*,\max}$ dimensionless vaporization time, t_v^* and the product between both, $a^{*,\max} \bullet t_v^*$. Then, the model holds in the entire spectrum of Υ, as shown in Table 1.

Table 1 – Values of the flow parameter
Adapted from: Fay (2003)

Parameter	**Flow parameter - Υ (-)**							
	<< 1	**1/3**	**1**	**1,784**	**3**	**10**	**30**	**>>1**
$a^{*,\max}$	$1.155\sqrt{\Upsilon}\left(1+0.463\Upsilon\right)$	0.661	1.113	1.431	1.716	2.233	2.521	2.828
t_v^*	$\left(1.493/\sqrt{\Upsilon}\right)+0.304$	2.875	1.775	1.414	1.414	1.414	1.414	1.414
$a^{*,\max} \bullet t_v^*$	$1.724+0.351\sqrt{\Upsilon}$	1.899	1.976	2.024	2.427	3.157	3.565	4.000

Values of Υ in the interval $\Upsilon << 1$ (and, consequently, $\Upsilon \leq 1/3$), Fay (2003) model proposes three continuous equations for the parameter Υ and the dimensionless variables $a^{*,\max}$, t_v^* and $a^{*,\max} \bullet t_v^*$:

$$a^{*,\max} = 1.155\sqrt{\Upsilon}\left(1+0.463\Upsilon\right) \tag{17}$$

$$t_{\mathrm{v}}^{*} = \left(1.493/\sqrt{\Upsilon}\right) + 0.304 \tag{18}$$

$$a^{*,\max} \bullet t_{\mathrm{v}}^{*} = 1.724 + 0.351\sqrt{\Upsilon} \tag{19}$$

For $\Upsilon > 30$ ($\Upsilon \gg 1$) Fay (2003) used dimensionless asymptotic values of 2.828, 1.414 and 4, respectively, for $a^{*,\max}$, t_{v}^{*} and $a^{*,\max} \bullet t_{\mathrm{v}}^{*}$. However, for Υ in the interval $1/3 < \Upsilon < 30$, Esteves (2010) and Esteves and Parise (2013a,b), differently from the values of Table 1, used approximated continuous functions to calculate Υ . Figures 3 and 4 present ahead the corresponding equations (20) and (21).

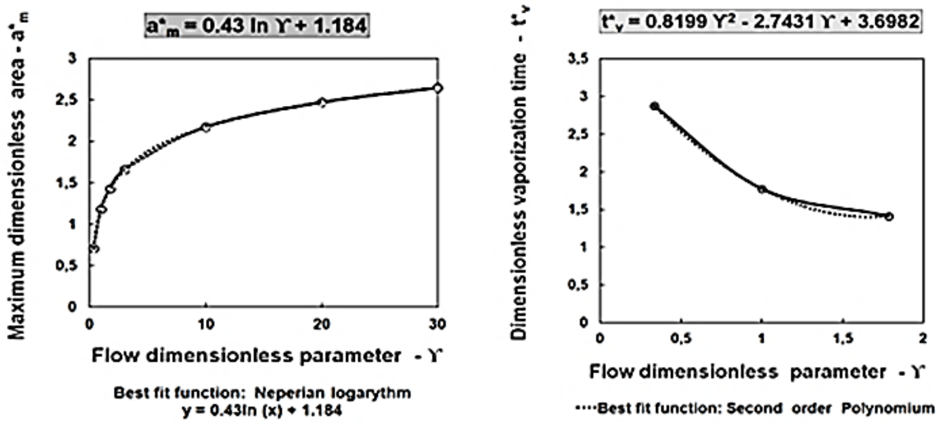

Figs. 3 and 4 – Continuous curves for the Eqs. (20) and (21), respectively. Source: Esteves (2010)

$$a^{*,\max} = 0.43\ln\Upsilon + 1.184 \tag{20}$$

$$t_{\mathrm{v}}^{*} = 0.8199\Upsilon^{2} - 2.7431\Upsilon + 3.6982 \tag{21}$$

Table 2 presents the comparison for the calculated values of $a^{*,\max}$, t_{v}^{*} and Υ , with the corresponding variables of the Table 1 for the interval $1/3 \le \Upsilon \le 30$. We use the colors dark grey and light grey, respectively, for $a^{*,\max}$ and t_{v}^{*} .

Table 2 – Parameters of Eqs. (17) to (21)
Source: Esteves (2010)
Obs.: (¹) Calculated with Eq. (17) (²) Calculated with Eq. (18)

Υ (-)	$a^{*,\max}$ (-)			t_{v}^{*} (-)		
	From Table 1	**Eq. (20)**	**Deviation (%)**	**From Table 1**	**Eq. (21)**	**Deviation (%)**
0.001	0.037 (1)	-	-	47.517 (2)	-	-
0.010	0.116 (1)	-	-	15.234 (2)	-	-
0.100	0.382 (1)	-	-	5.025 (2)	-	-
0.333	0.661	0.712	+7.7	2.875	2.875	0
0.000	1.113	1.184	+6,4	1.775	1.775	0
1.784 (critical)	1.431	1.433	+0.1	1.414	1.414	0
3.000	1.716	1.656	-3.3	1.414	-	-
1.000	2.233	2.174	-3.8	1.414	-	-
20.000	2.472	2.472	0	1.414	-	-
30.000	2.520	2.647	+5.0	1.414	-	-
≫ 30.000	2.828	-	-	1.414	-	-

Esteves (2010) uses the values of Υ, 0.001, 0.01 and 0.1 (below 1/3), and >>30, to illustrate the application of Eqs. (17) and (18) to calculate, respectively, $a^{*,\max}$ and t_{v}^{*}. Eqs. (20) and (21) adopt the interval $1/3 \le \Upsilon \le 30$, to calculate the results of $a^{*,\max}$ and t_{v}^{*} to compare with the corresponding values of the Table 1. Table 2 shows the percent deviations varying between +7.7% and 5% for $a^{*,\max}$, and 0% for t_{v}^{*} between $1/3 \le \Upsilon \le 1.784(\text{critical})$.

Below and above these limits, t_{v}^{*} is not sensitive. At critical point, the flow starts to decelerate due to interaction with the sea, by vaporization and turbulence. From this point (1.784) downwards, the pool spreads more slowly until it reaches its maximum area, decreasing asymptotically and monotonically. In the original model, Fay (2003) used the tear diameter varying between 1 and 100 m², as the present work. Additionally, we made tests using the carrier geometries of Fay (2003) (125,000 m³) and SNL (2008a,b) (265,000 m³) in the interval $1/3 \le \Upsilon \le 30$. The purpose was to verify if Eqs. (20) and (21) would introduce uncertainties in the remaining of the modelling. The vaporization velocities used in the tests were 0.00021 (2.1 x 10^{-4}) m/s and 0.0011 (11 x 10^{-4}) m/s and tear diameters varied between 1 and 100 m². The results were compatible as depicted in the Figs.5 and 6.

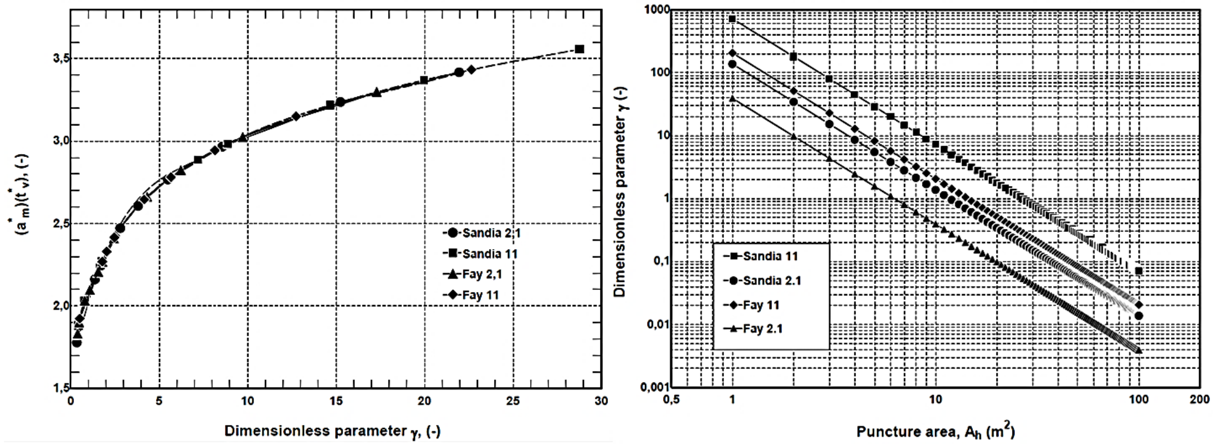

Figs. 5 and 6 – Adherence test for the Eqs. (20) and (21) respectively

Expressing then $A_{\mathrm{p_{sc}}}^{\max}$ and t_{v} in terms of $a^{*,\max}$, t_{v}^{*} and Υ, according to Fay (2003), one has:

$$A_{\mathrm{p_{sc}}}^{\max} = \left(\frac{A_{\mathrm{h}} \sqrt{g h_0}}{\langle \dot{y} \rangle} \right) a^{*,\max} = \left[\frac{ß^2 (2\pi\Delta) g (h_0 A_{\mathrm{t}})^3}{\langle \dot{y} \rangle^2} \right]^{1/4} \frac{a^{*,\max}}{\sqrt{\Upsilon}} \tag{22}$$

$$t_{\mathrm{v}} = \left(\frac{A_{\mathrm{t}}}{A_{\mathrm{h}}} \right) \sqrt{\frac{h_0}{g}}\; t_{\mathrm{v}}^{*} = \left[\frac{h_0 A_{\mathrm{t}}}{ß^2 (2\pi\Delta) g \langle \dot{y} \rangle^2} \right]^{1/4} t_{\mathrm{v}}^{*} \sqrt{\Upsilon} \tag{23}$$

$$D_{\mathrm{p_{sc}}} = 2\sqrt{\frac{A_{\mathrm{p_{sc}}}}{\pi}} \tag{24}$$

4.6. Critical, upper and lower bound values of the pool spill/spreading

When the deployment flow through the tear transit from slow to fast, respectively, with small and large holes, with, critical parameters can be calculated, so

$$A_{\mathrm{h}_{\mathrm{cr}}} = 0.749\left[\frac{ß^2(2\pi\Delta)\langle\dot{y}\rangle^2 h_0 A_{\mathrm{t}}^3}{g}\right]^{1/4} \tag{25}$$

$$A_{\mathrm{p}_{\mathrm{sc,\,cr}}}^{max} = 1.071\left[\frac{ß^2(2\pi\Delta)g\left(h_0 A_{\mathrm{t}}\right)^3}{\langle\dot{y}\rangle^2}\right]^{1/4} \tag{26}$$

$$t_{\mathrm{v}_{\mathrm{cr}}} = 1.889\left[\frac{h_0 A_{\mathrm{t}}}{ß^2(2\pi\Delta)g\langle\dot{y}\rangle^2}\right]^{1/4} \tag{27}$$

$$D_{\mathrm{h}_{\mathrm{cr}}} = 2\sqrt{\frac{A_{\mathrm{h}_{\mathrm{cr}}}}{\pi}} \tag{28}$$

$$D_{\mathrm{p}_{\mathrm{sc,\,cr}}} = 2\sqrt{\frac{A_{\mathrm{p}_{\mathrm{sc,\,cr}}}}{\pi}} \tag{29}$$

According to Fay (2003), these values define the difference between flow regimes quasi steady-state (the most) from transient ultra-fast regimes which occur, respectively, with small and large tears on the ship's hull. Upper and lower bounds of can also be determined for $A_{\mathrm{p}_{\mathrm{sc}}}^{\max}$ and t_{v} for instantaneous deployments when Υ approaches zero, with $ß = 4/\sqrt{3} \approx 2.31$, such as according to this author:

$$A_{\mathrm{p}_{\mathrm{sc,ub}}}^{\max} \leq 2.58\left[\frac{g\Delta\left(h_0 A_{\mathrm{t}}\right)^3}{\langle\dot{y}\rangle^2}\right]^{1/4} \tag{30}$$

$$t_{\mathrm{v}_{\mathrm{lb}}} \geq 0.785\left(\frac{h_0 A_{\mathrm{t}}}{g\Delta\langle\dot{y}\rangle^2}\right)^{1/4} \tag{31}$$

4.7. Transition from semicircular to circular pool

Item 5 assumes combustion of circular pools, while spill/spreading model considerers them as semicircular. A transition from one to another should be set. Now withstanding that: (I) there is conservation of the mass, energy and linear momentum; (ii) density of the cryogenic remains constant in the pool, (iii) pool thickness is constant, and (iv), the area of the pools is the same in both cases during the transition (FERC, 2004; Fay, 2003; Luketa-Hanlin, 2006; ABS, 2004; SNL, 2004; Opschoor, 1980; MKOPSC, 2008), then one has:

$$A_{\mathrm{p_{sc}}}^{\max} = A_{\mathrm{p_{ci}}}^{\max} \Rightarrow \frac{1}{2}\frac{\pi}{4}D_{\mathrm{p_{sc}}}^2 = \frac{\pi}{4}D_{\mathrm{p_{ci}}}^2 \Rightarrow D_{\mathrm{p_{sc}}} = 2\left(\frac{2}{\pi}A_{\mathrm{p_{sc}}}^{\max}\right)^{1/2} \Rightarrow R_{\mathrm{p_{sc}}} = \frac{1}{2}D_{\mathrm{p_{sc}}} \tag{32}$$

this leads to

$$D_{\mathrm{p_{sc}}} = \sqrt{2}\,D_{\mathrm{p_{ci}}} \approx 1.414 D_{\mathrm{p_{ci}}} \Rightarrow D_{\mathrm{p_{ci}}} = \frac{1}{\sqrt{2}}D_{\mathrm{p_{sc}}} \approx 0.7071 D_{\mathrm{p_{sc}}} \tag{33}$$

Equation (33) defines a circular pool. This is equivalent to a semicircular pool as calculated by Fay's (2003) model. Geometrical and thermal characterization of the fire model may use this input data. Taking the maximum value of the pool area given by Eq. (22)

and considering that $A_{\mathrm{p_{sc}}}^{\max} = A_{\mathrm{p_{ci}}}^{\max}$ from Eq. (32), one can calculate the maximum diameters corresponding to the upper bound limits of the semicircular and circular pools. For an instantaneous spill, one has

$$D_{\mathrm{p_{sc,ub}}} \le 2\left(\frac{2}{\pi} A_{\mathrm{p_{sc,ub}}}^{\max}\right)^{1/2} \Rightarrow D_{\mathrm{p_{ci,ub}}} \le 2\left(\frac{1}{\pi} A_{\mathrm{p_{sc,ub}}}^{\max}\right)^{1/2} \tag{34}$$

5. Mathematical model for the pool fire with non-premixed turbulent combustion

5.1. Introduction

The model equations presented ahead, are in accordance with Esteves (2010) and Esteves and Parise (2013a,b). The multi-zone model is based on models from TMS (2006), also reported in Raj (2007a,b,c) and Fay (2006), proved to be the most adequate to the present objective, which considers circular pools with diameters varying between 10 and 500 m, compatible with what is expected to occur with the current carriers. These models consider that the thermal plume has its 'visible' height of the flame composed by different combustion and intermittency zones as depicted in Fig. 7.

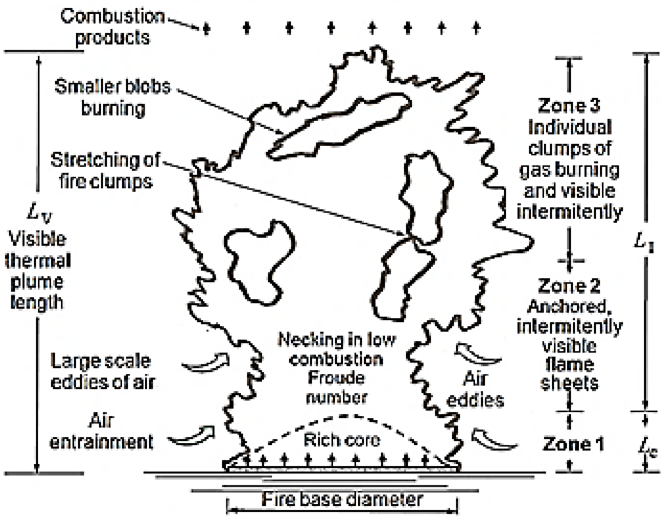

Fig. 7 - Sketch of the thermal plume. Source: Esteves and Parise (2013a,b). Adapted from: Raj (2007a,b)

They represent a good compromise between conciseness, accuracy and low computational efforts, as well as having their simulation results validated against Montoir and Lake Charles field tests, following the current trend in the LNG industrial practice.

The plume is composed of three zones. (i) The lowest part, $L_{\mathbb{C}}$, considers that the combustion is 'clean', (ii) the middle zone, $L_{\mathbb{I}}$, where the plume pulsates intermittently, (iii) and the highest part which contains its tips, where combustion products are drafted from the fire column by buoyancy. This is a time averaged geometric *loci* of the visible height of the thermal plume. The three zones added form the 'visible' plume length, $L_{\mathbb{V}}$ (m) which is its time average height. The diameter of the plume firebase is $D_{\mathrm{p_{ci}}}$.

5.2. The physics of the pool fire models

The 'visible flame' $L_{\mathbb{V}}$ corresponds to the sum of the 'combustion zone' (zone 1) of length $L_{\mathbb{C}}$ with the 'thermal plume zone', $L_{\mathbb{I}}$. This zone starts at the upper edge of the combustion zone where all fuel is consumed, and there is no additional increase in the thermal energy flow, although the mass and linear momentum flows continue to increase. On the lateral side of the flame, the continuous air supply induces drops in temperature, combustion products concentration and upward axial velocity. The flame envelope that is visible in this zone is the outer layer of the fuel vapors being burned. In pool fires of large diameter, this portion is practically thin from the optical point of view and irradiates with high temperature (Raj, 2007c). Just above the region of full combustion, comes the zone 2 where the flame is considered to be "anchored" to the base, but presents a less efficient combustion zone in large diameter pool fires.

The physics of the solid flame model can be complemented as presented in the Fig. 8. In the combustion zone, fresh fuel and air are mixed and react in stoichiometric proportions to form combustion products.

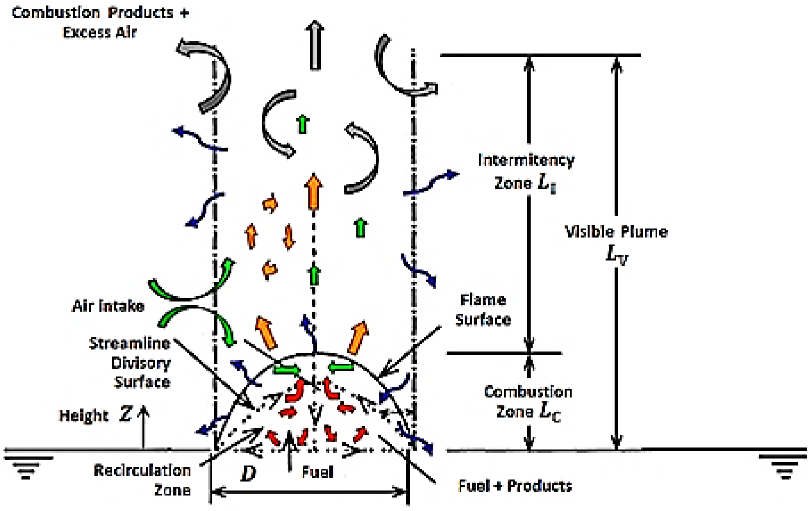

Fig. 8 – Sketch of the two zones model proposed by Fay (2006).
Labels: **Green**: side air intake; **Blue**: emitted thermal radiation; **Red**: vaporized fuel, within the combustion zone
Orange: vaporized fuel outside the combustion zone; **Gray**: smoke
Adapted from: Fay (2006)

In the bottom region of the fire, $L_{\mathbb{C}}$, the vapor combustion is vigorous and very efficient. The axial velocity of the fuel gases accelerates rapidly in the vertical direction, in the same fashion as the mass, momentum and thermal energy. Unlike flares flames, where the fuel flow provides initially a considerable upward of linear momentum flow, the fuel vapor flow in a pool fire is mixed by means of whirls in the recirculation zone. Figure 9 (a) presents fire whirls produced in field experiments with JP4 and JP8 fuel fires in the presence of wind (SNL, 2011; Tieszen et al. 1996), Figures 9(b)(c) show the register of an laboratory experiment to study fire whirls initiated as pool fires on a water surface, exploiting the high-efficiency of fire whirls for oil-spill remediation.

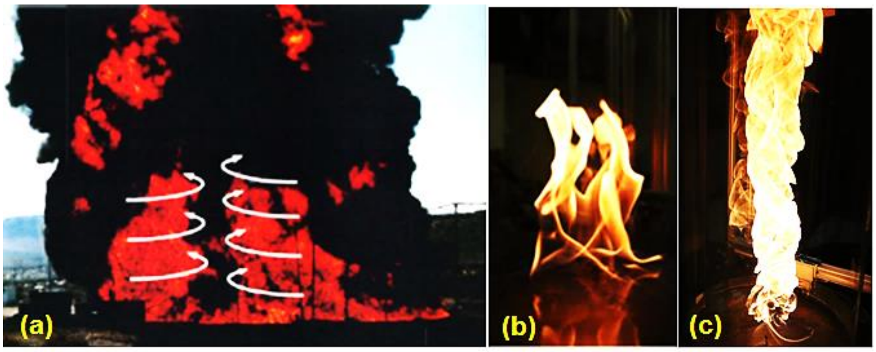

Fig. 9 (a) – Fire whirls induced by wind. (Source: SNL, 2011).
Fig. 9 (b) - The very first moment of the evolution from a pool fire into a whirl over water
Pool fire is formed following ignition.
Fig. 9 (c) - Fire whirl develops subsequently.
[Source: Xiao et al. (2016).
Available in: https://arxiv.org/abs/1605.01315. Access: 23 Febr 2017.

5.2.1. The vorticity conservation within the fire column

Two main phenomena govern the mechanics of the fluids (fuel, gases and soot) within a fire column: vorticity (whirls/recirculation) and vortex strain/stress. The structure of fire whirls due to the vorticity within the fire column consists of an upward convective current generated by the fire and a swirling motion (vorticity) generated via interaction of an ascending hot plume with ambient air (SNL, 2011).

Such vortex structures can occur at regular intervals from side to side of the pool edge, which magnitude is considered roughly as of half a diameter in extension. In addition, chances are that they can happen in pairs or alternating from side to side from the pool edge. The whirls that form is expected to increase the combustion rates generating more soot removal and, therefore, high *SEP* values within the flame structure.

The upper surface (meniscus) of the recirculation zone is a current surface. It separates the external flow that moves inwardly and upwards toward the fire top (orange and green arrows). It circulates downstream near the axis of the fire column carrying fuel towards outside its surroundings along the surface (red arrows). This recirculation zone may be thought of as that of a wake formed at the borders of a rigid body, where the shearing of the external flow which is withdrawn from the body, induces a low speed recirculation on the wake.

The intermittent black smoke formed in zone (2) begins to obscure partially the heated core of the flame (Raj, 2007c). The narrowing of the flame after the 'bottleneck' is formed with high Froude numbers, due to the entrance of air in the lateral of the flame with large scale eddies, causing shrinking of the local diameter of the pool fire envelope.

In this zone, the flame pulsates (Raj, 2005) due to the internal mixing of not burned vapors from pyrolysis, or partially burned from the combustion zone. This takes place because of the insufficiency of oxygen in the central core, caused by the whirls/recirculation that occurs due to buoyancy. At the end of zone (2), the flame begins to stretch the vortex structures (vortex shedding), and an increase in the shedding rate can then lead to an abrupt extinction of the combustion process (Silva, 2004).

Turbulent diffusion flames comprise two distinct time scales (Warrants et al. (1999). In the beginning of the fire, fuel and oxidizer are separate, mixing each other by diffusion as the time goes by; this process takes place in the same region, but with two different time scales, chemical (molecular) and mechanical (diffusion) to cope with flame stability and extinction.

These two time scales t_{chem} (chemical reaction) and t_{diff} (mechanical gas diffusion) are strongly dependent on the reactants properties and flow regime (SNL, 2011). The first is much faster than the second is, except near flame extinction is.

As the flow reaches turbulent velocities t_{diff} tends to decrease, and a critical flow velocity may govern the process; in this case, chemical reaction cannot support the fuel/oxidant demand, giving place to the flame extinction. The Damkhöler number, Da = t_{iff}/t_{hem}, governs the flame extinction process. When these two times are of the same order of magnitude, it is necessary to consider a finite chemical rate, therefore t_{chem} limits the combustion rate during the extinction time.

To comprehend the phenomenon that occurs in turbulent diffusion flames, it is necessary to compare to what happen in laminar flames. According to Cant (1999), a physical quantity of interest in the drawing may be the vector $\hat{\mathbf{n}}$ normal to the flame surface based on the gradient of the progress of combustion chemical reaction, r and oriented in the direction of flame propagation, such that $\hat{\mathbf{n}} = -[\nabla r]/\|[\nabla r]\|$.

Another important quantity to model is the tangential and local strain rate of the flame plane, since it affects local propagation rate of the turbulent flames. Then the tensor $\bar{\bar{\boldsymbol{\sigma}}}$ of the net stretching rate, $\{\sigma_{ij}\} = \frac{1}{2}\{\partial u_j/\partial x_i - \partial u_i/\partial x_j\}$, is computed in each point and then interpolated on the flame surface in a given position, $x_{i_{\mathbb{F}}}$.

The tensor undergoes a rotation relative to a coordinate system, aligns with the normal to the flame surface, and the tangential rate is then calculated by the sum of the eigenvalues of the stretch rate in the plane tangent to that surface. In a similar manner, the curvature of the flame surface is calculated with the tensor of the normal gradient of the flame surface, $\{\nabla\hat{\mathbf{n}}\}$, giving the tensor $\bar{\bar{\boldsymbol{\sigma}}} = \{\sigma_{ij}\} \equiv \partial\sigma_i/\partial x_j$ in each point of coordinate $Z_{i_{\mathbb{F}}}$ of this surface (Cant et al. 1999).

In the same fashion for stretching, the tensor $\{\nabla\hat{\mathbf{n}}\}$ experiments another rotation, aligns with the normal and the two main curvatures of the flame surface, calculating the eigenvalues in the tangential plane, forming therefore an average curvature.

Otherwise, it is fact that a rise of the stretch rate leads to a sudden extinction of the combustion process. Warrants et al. (1999) suggested that, generally, the presence of unburnt hydrocarbons is an indication of possible flame extinction. A new partial mixture may take place between fuel and oxidizer during the interval the flame element remains ‘extinct’. When the flame returns to ‘ignite’, a partially premixed flame may occur, giving an intermittent character to the process (Raj, 2007c).

In pool fires, the flame surface acts as a current surface and provides the necessary shear to induce recirculation movements in the flow, feeding the buildup of vortex structures. There is a rotation in the vector field $\mathbf{u}$ of linear velocity, which magnitude is $[\nabla\wedge\mathbf{u}]$ along the axis of the plume. This curl is quantified by the vorticity vector, $\boldsymbol{v}$, which is twice the angular velocity vector $[2\omega]$ that quantifies the whirls within the column.

Mathematically, $\boldsymbol{v}$ is determined by the double product transform $\left[\bar{\bar{\bar{\boldsymbol{\varepsilon}}}} : \bar{\bar{\boldsymbol{\Omega}}}\right]$, applying the third order tensor of permutation, $\bar{\bar{\bar{\boldsymbol{\varepsilon}}}} \equiv \{\varepsilon_{i,j,k}\}$, on e vorticity antisymmetric vorticity tensor, $\bar{\bar{\boldsymbol{\Omega}}}$, to lower its order, and form the vorticity vector, $\boldsymbol{v}$.

This latest is therefore decomposed as the half of the subtraction between the tensor of the velocity gradient, $\{\nabla\mathbf{u}\}$, and its transpose, $\{\nabla\mathbf{u}\}^{\top}$, to lower the order of the vorticity tensor, $\bar{\bar{\boldsymbol{\Omega}}}$. As a vector, it is a quantity easier to operate and compute. Equation (35) expresses this vector as:

$$\boldsymbol{v} = 2\boldsymbol{\omega} = 2\left[\nabla \wedge \mathbf{u}\right] \equiv \left[\overline{\overline{\overline{\boldsymbol{\varepsilon}}}} : \overline{\overline{\Omega}}\right] \equiv \left[\overline{\overline{\overline{\boldsymbol{\varepsilon}}}} : \{\nabla \mathbf{u}\}\right] \equiv \tfrac{1}{2}\left\{\{\nabla \mathbf{u}\} - \{\nabla \mathbf{u}\}^{\top}\right\}$$

$$\equiv \begin{pmatrix} \hat{\mathbf{e}}_1 & \hat{\mathbf{e}}_2 & \hat{\mathbf{e}}_3 \\ \partial/\partial x_1 & \partial/\partial x_2 & \partial/\partial x_3 \\ u_1 & u_2 & u_3 \end{pmatrix} = \left[\hat{\mathbf{e}}_j \wedge \hat{\mathbf{e}}_k\right]\frac{\partial}{\partial x_j} u_k = \varepsilon_{ijk}\frac{\partial u_k}{\partial x_j}\hat{\mathbf{e}}_i$$

$$= \left(\frac{\partial u_3}{\partial x_2} - \frac{\partial u_2}{\partial x_3}\right)\hat{\mathbf{e}}_1 + \left(\frac{\partial u_1}{\partial x_3} - \frac{\partial u_3}{\partial x_1}\right)\hat{\mathbf{e}}_2 + \left(\frac{\partial u_2}{\partial x_1} - \frac{\partial u_1}{\partial x_2}\right)\hat{\mathbf{e}}_3$$

$$\equiv \omega_{x_1}\hat{\mathbf{e}}_1 + \omega_{x_2}\hat{\mathbf{e}}_2 + \omega_{x_3}\hat{\mathbf{e}}_3 \qquad (35)$$

As $\left[\nabla \wedge \mathbf{u}\right] \neq 0$ in all points of the flow within the fire column, it is possible to apply the operator curl to the Navier-Stokes equation to define the equation of vorticity conservation. Writing it with Gibbs' notation (Möller and Silvestrini, 2004), one gets:

$$\underbrace{\frac{D\boldsymbol{v}}{Dt}}_{\substack{\text{Material Vorticity}\\ \text{time change}}} = \underbrace{\frac{\partial \boldsymbol{v}}{\partial t}}_{\substack{\text{Local Vorticity}\\ \text{Time change}}} + \underbrace{\left[\mathbf{u}\bullet\{\nabla \boldsymbol{v}\}\right]}_{\substack{\text{Convective Vorticity}\\ \text{Change rate}\\ \text{following the movement}}} = \underbrace{\left[\boldsymbol{v}\bullet\{\nabla \mathbf{u}\}\right]}_{\substack{\text{Vortexes}\\ \text{Elongation}}} + \underbrace{\upsilon\bullet\left[\nabla^2 \boldsymbol{v}\right]}_{\substack{\text{Vorticity}\\ \text{Diffusion}}} \qquad (36)$$

On the hand, using notation with indices:

$$\underbrace{\frac{\partial v_i}{\partial t}\hat{\mathbf{e}}_i}_{\substack{\text{Convective aceleration}\\ \text{Local change}\\ \text{rate of vorticity}}} + \underbrace{u_j\frac{\partial v_k}{\partial x_j}\hat{\mathbf{e}}_k}_{\substack{\text{Convective transport rate}\\ \text{of vorticity following}\\ \text{the movement}}} = \underbrace{v_j\frac{\partial u_k}{\partial x_j}\hat{\mathbf{e}}_k}_{\substack{\text{Vorticity change rate}\\ \text{due to elongation of}\\ \text{vortex lines}}} + \underbrace{\upsilon\frac{\partial^2 v_k}{\partial x_i^2}\hat{\mathbf{e}}_k}_{\substack{\text{Vorticity change rate}\\ \text{due to the viscous}\\ \text{diffusion}}} \qquad (37)$$

Equation (37) indicates that the sum of the local acceleration of the vorticity of a material particle of the fuel with the convective transport of the vorticity is conserved by the sum of shearing vortexes (elongation) with the viscous diffusion of the vorticity. They are important because they describe the flame folds and viscous effects within the fire column.

As already observed experimentally, in the combustion zone (zone 1), fuel and air diffuse towards the flame surface and are carried by the flow convection in upward direction. Flame combustion releases heat which, as with combustion products, diffuses from that surface, increasing the temperature and reducing the density of the gaseous zone of the flame. Low density gas is accelerated upward by the unbalance between gravity and surface forces (compression and shear), supplying buoyancy and ascending momentum to the fuel vapors in that region.

At the top of the flame surface, all vapor fuel that left the pool had already been burned leaving behind only excess air and combustion products. The remaining path of these gases in the vertical drafting also evolves as a buoyancy plume (Silva, 2004; Warnatz et al., 1999; Heskestad, 1998; Steward, 1970; Morton et al., 1956).

5.3. The governing equations of mass diffusion conservation of the combustion process

Diffusion is the mass transport process caused by concentration gradients. This process governs non pre-mixed turbulent diffusion flames. Temperature gradients cause mass transport in irreversible processes, as known as thermal diffusion or 'Soret effect'. In the same fashion, concentration gradients may cause energy transport, or 'Dufour effect'. In combustion processes, the last effect (Dufour) usually is considered negligible, although it is present in other chemical reacting flows. The first Fick's law describes mass fluxes. This is described by the first term of the right side of the Eq. (38),

$$\underbrace{\left|\mathbf{J}_i\right|}_{\substack{\text{Mass Diffusion}\\ \text{of chemical spieces}\\ \text{Mass transport}}} = \underbrace{\frac{c^2}{\rho}\mathcal{M}_i\sum_j \mathcal{M}_j\mathfrak{D}_{ij}\frac{\partial x_j}{\partial z}}_{\substack{\text{Mass Diffusion}\\ \text{First Fick`s law}}} - \underbrace{\frac{\mathfrak{D}_i^{T}}{T}\frac{\partial T}{\partial z}}_{\substack{\text{Thermal diffusion}\\ \text{Soret effect}}} \qquad (38)$$

For industrial applications, it is acceptable an to use the following approximation

$$\left|\mathbf{J}_i\right| \approx -\mathfrak{D}_i^{\mathcal{M}} \rho \frac{w_i}{x_i}\frac{\partial x_i}{\partial z} - \underbrace{\frac{\mathfrak{D}_i^{T}}{T}\frac{\partial T}{\partial z}}_{\text{Soret effect}} \tag{39}$$

If the chemical kinetics is rapid enough, the combustion of laminar/non-pre-mixed flames follows specific equations. According to Warrants et al. (1999), similarly to the mass fraction of the chemical species i, w_i, one can define as $\mathcal{Z}_i$ as the mass fraction of the chemical element i in the total mass of the mixture. The following correlation applies (Silva, 2004; Warrants et al., 1999; Williams, 1985):

$$\mathcal{Z}_i = \sum_{j=1}^{Q} \mu_{ij}\, w_j \qquad \text{for} \qquad i = 1, 2, \ldots, \mathcal{E} \tag{40}$$

This mass fraction of an element has a special meaning since it cannot be changed by chemical reactions but it can be modified otherwise by mixing processes[9]. For simple and non-premixed laminar flames, treated as a co-current flow between fuel Moreover, oxidizer, a new scalar variable can be defined, independently of i, called 'mixture fraction', ξ or the 'passive scalar'. This parameter is a function of the element mass fraction $\mathcal{Z}_i$. Indexes 1 and 2 in Eq. (41) denote the two abovementioned streams (fuel and oxidizer), giving the following correlation (Warrants et al, 1999):

$$\xi = \frac{\mathcal{Z}_i - \mathcal{Z}_{i_2}}{\mathcal{Z}_{i_1} - \mathcal{Z}_{i_2}} \tag{41}$$

The advantage of this formulation is that ξ keeps a linear relation with $\mathcal{Z}_i$ and w_j due to Eqs. (40) and (41). This correlation is of great importance to the present model. Warrants et al. (1999) concluded on the other hand that there is a quasi-linear correlation between mass fraction and mixture fraction, so that $w_i \approx w_i(\xi)$ is used to model non-premixed turbulent flames, which is exactly the case for the present modelling. In addition, as $\mathcal{Z}_i$ of a given chemical element cannot be changed by chemical reaction processes (since the mass is conserved), in the same fashion the mixture fraction, ξ cannot be altered, since it is conserved according to Eq. (41). These correlations are fundamental to the simplification of the mass and energy conservation balances to be presented hereinafter.

However, the treatment of source terms in chemical equilibrium, i.e., the chemical reaction rates in the species conservation equations, is a cumbersome task. Thus, one of the options is to use the conservation equations of the chemical elements, since they do not change in chemical reactions. As the elements of a chemical reaction cannot be created or destroyed by this principle, the source terms vanish in the equations of the elements conservation, via their mass fractions as postulated by Williams (1985). So, the mass conservation of the chemical species can be written as (Bird et al. 2002; Warrants et al, 1999), written in Gibbs' notation:

$$\underbrace{\frac{\partial(\rho_i)}{\partial t}}_{\substack{\text{Transient term}\\ \text{Accumulation}\\ \text{of the species i}}} + \underbrace{\left(\nabla \bullet [\rho_i \mathbf{u}]\right)}_{\substack{\text{Convective term}\\ \text{Transport}\\ \text{of the species i}}} - \underbrace{\left(\nabla \bullet \mathbf{j}_i\right)}_{\substack{\text{Diffusive term}\\ \text{Diffusion}\\ \text{of the species i}}} = \underbrace{\mathcal{M}_i \dot{\omega}_i}_{\substack{\text{Source term}\\ \text{Production}\\ \text{of the species i}}} \tag{42}$$

If the molecular mass diffusivities, $\mathfrak{D}_i$, of all chemical elements are approximately the same, μ_{ij} can multiply Eq. (42) by Eq. (40), and adds to itself. If the sum of all source terms of its right side of the in Eq. (42) ($\sum_{j=1}^{Q} \mu_{ij} \mathcal{M}_i \dot{\omega}_i$) is null (no source terms generation), one can have another equivalent equation with no source terms, $\mathcal{M}_i \dot{\omega}_i = 0$, such as

[9] An axiom from Chemistry.

$$\underbrace{\frac{\partial(\rho \mathcal{Z}_i)}{\partial t}}_{\substack{\text{Transient term} \\ \text{Accumulation} \\ \text{of the species} \\ \text{(chemical element) i}}} + \underbrace{\left(\nabla \bullet [\mathbf{u}_i\, \mathcal{Z}_i]\right)}_{\substack{\text{Convective term} \\ \text{Transport} \\ \text{of the species} \\ \text{(chemical element) i}}} - \underbrace{\left(\nabla \bullet \left[\rho \mathfrak{D} [\nabla \mathcal{Z}_i]\right]\right)}_{\substack{\text{Diffusive term} \\ \text{Diffusion} \\ \text{of the species} \\ \text{(chemical element) i}}} \approx 0 \qquad (43)$$

5.4. Non-premixed turbulent flames with chemical equilibrium

The application of Reynolds' (time average) and Favre's (density) filters on Eq. (43) will generate new fluctuations and not explicit terms. Adding more functions of the average dependent variables, will produces a 'not closed' Navier-Stokes equation ('the turbulence closing problem'). To close this equation it is necessary then to model the resulting Reynolds' tensors as a turbulent transport, in the same fashion as if it were laminar. This modelling is possible when one considers the 'gradient transport approximation', based on the 'Boussinesq's approximation' (Silveira Neto, 2002, 1988). This approximation considers that the time average of the Reynold's tensor flux is proportional to the tensor of the Favre's average of the transported quantity (Warrants et al., 1999), i.e., $\overline{\{\rho\, \mathbf{u}''\mathbf{q}_i''\}} \approx -\bar{\rho}\, \mu_T \{\nabla \tilde{\mathbf{q}}_i\}$. With this empirical correlation it is possible simplify the average conservation equations for the passive scalar of the mixture fraction. The flow turbulent viscosity models use models of '0', '1', '2' equations. It includes the turbulent kinetic energy and its dissipation rate $(\kappa - \varepsilon)$ (Sagaut, 2001; Pope, 1991; Warrants et al., 1999; Piomelli, 1999). The passive scalar, ξ, does not depend on the chemical element i, rather it depends linearly on the mass fraction w_j instead, because of Eqs. (40) and (41). As the mixture fraction is a dimensionless and normalized quantity, as long as the mixture proceeds, in every point of the thermal plume flow, ξ can be considered as the mass fraction of the fluid material originated from stream 1 and 1-ξ the mas fraction originated from stream 2 (Warrants et al., 1999). Using Eqs. (41) and (43), it is possible to reach the conservation equation of the passive scalar ξ of the mixture fraction, simplifying the turbulence modelling, so one reaches the Eq. (44),

$$\underbrace{\frac{\partial(\rho \xi)}{\partial t}}_{\substack{\text{Transient term} \\ \text{Change rate of the} \\ \text{passive scalar per} \\ \text{unit of volume}}} + \underbrace{\left(\nabla \bullet [\rho\, \mathbf{u}\, \xi]\right)}_{\substack{\text{Convective term} \\ \text{Transport rate of the} \\ \text{passive scalar per} \\ \text{unit of volume}}} - \underbrace{\left(\nabla \bullet \left[\rho \mathfrak{D} [\nabla \xi]\right]\right)}_{\substack{\text{Diffusive term} \\ \text{Diffusion rate of the} \\ \text{passive scalar per} \\ \text{unit of volume}}} = 0 \qquad (44)$$

Warrants et al. (1999) considers that as the passive scalars has no source or sink term, it stands during the combustion chemical reaction and, with this sense, one can consider it as a 'conserved scalar'. Therefore, it is possible to model diffusion flames with the appropriate boundary conditions with the oxidizer at $\mathcal{Z} \to -\infty$ and the fuel at $\mathcal{Z} \to +\infty$. In this sense, it is possible to state the following premises and simplifying hypothesis (Silva, 2004; Warrants et al, 1999):

1. The combustion takes place with 'fast' chemical equilibrium (kinetics). The chemical species react until the equilibrium takes place as fast as they mix, and the chemical reaction is $\mathrm{C} + \mathrm{n\,O} \to \mathrm{Products}$, describing a global combustion process;
2. Molecular mass diffusivities of all scalars are equal and all species mix equally;
3. Energy diffuses at the same rate for all species, i.e., the Lewis number is approximately 1 (molecular mass diffusion vs. thermal diffusion, $Le = \alpha / \mathfrak{D} = k_{mix} / \rho \mathfrak{D} c_p \approx 1$);
4. There is no heat loss within the flame (fire plumes are 'adiabatic'); all scalar variables (temperature, enthalpy, mass fraction and density) are known functions only of the mixture fraction scalar, ξ. Additionally, the known function is the equilibrium composition. As a premise, the turbulent kinetic energy of the flow is supposed to be negligible, at constant pressure;
5. There is no source term, as well as no creation nor process extinction;
6. Mass transport takes place with chemical species diffusion, according to the first Fick's law [Eq. (38)];
7. The combustion occurs with constant transport proprieties.

The hypotheses 2 to 7 above are known as 'Schvab-Zel'dovich's approximation'. This concept considers that there are density variation and volumetric expansion, providing the heat release arising from combustion (Warrants et al., 1999). Thus, one can model enthalpy and temperature fields via passive scalar conservation. In other words, using the mixture fraction, ξ, according to Eq. (44) (Silva, 2004; Warrants et al., 1999; Fay, 2006), as follows:

$$\xi = \frac{h - h_{\mathrm{ox}}}{h_{\mathrm{v}} - h_{\mathrm{ox}}} \tag{45}$$

The mass fraction of the combustion products, $w_{\mathrm{prod}}(\xi)$, correlates with the temperature T via ξ of Eq. (45), using equation (46)

$$w_{\mathrm{i}} \approx w_{\mathrm{i}}(\xi) \equiv w_{\mathrm{prod}}(\xi) = \frac{T - T_{\mathrm{a}}}{T_{\mathrm{ad}} - T_{\mathrm{a}}} \tag{46}$$

As simplifying hypothesis, Eq. (45) represents the gas flow as 'convective dominant'. To this account, the fluxes of species mass diffusion, enthalpy of viscous shear stresses and compressive normal pressures within the flame are negligible (Fay, 2006). Otherwise, it shows that $w_{\mathrm{prod}}(\xi)$ is correlated and computed to T via ξ. Hence, one can reduce the modeling problem of non-premixed turbulent flames to the tracking of ξ, for homogeneous chemical species and their respective enthalpies. Thus, ξ is the only variable necessary for the description of the reaction process in the absence of source term. Moreover, this greatly simplifies the process of pool fire modeling.

5.5. The governing equations of energy conservation in the flame combustion process

The energy conservation equation written with Gibb's notation governs this process is (Esteves, 2010; Sparrow and Cess, 1978):

$$\underbrace{\rho c_{\mathrm{P}}(DT/Dt)}_{\substack{\text{Overall change}\\ \text{of Internal energy}}} = \underbrace{-(\nabla \bullet \mathbf{q}_{\mathrm{C}}) - (\nabla \bullet \mathbf{q}_{\mathrm{R}})}_{\substack{\text{Heat flux exchanged on the border}\\ \text{by molecular Conduction and Radiation}}} \underbrace{-(\beta^{*}/\mathcal{K})(\nabla \bullet \mathbf{u})}_{\substack{\text{Compression Work}\\ \text{done on the fluid}}} \underbrace{+\Phi}_{\substack{\text{Mechanical}\\ \text{Viscous Dissipation}\\ \text{of the fluid}}} \underbrace{+\rho \dot{Q}'''}_{\substack{\text{Source term}\\ \text{of heat Generarion}}} \tag{47}$$

with $\beta^{*} = \frac{1}{v}(\partial v/\partial T)_{P}$ and $\mathcal{K} = \frac{1}{v}(\partial v/\partial P)_{T}$.

Disregarding the compression work done on the fluid and the viscous dissipation, and developing the material derivative of the temperature, one can have (Esteves, 2010),

$$\rho c_{\mathrm{P}}\left(\partial T/\partial t + (\mathbf{u} \bullet [\nabla T])\right) = -(\nabla \bullet \mathbf{q}_{\mathrm{C}}) - (\nabla \bullet \mathbf{q}_{\mathrm{R}}) + \dot{Q}''' \tag{48}$$

Additionally, if the variations of the temperature with time are also negligible, one can find

$$\underbrace{+\dot{Q}'''}_{\substack{\text{Heat Generation rate}\\ \text{by Combustion of the fire plume}\\ \text{per unit of volume}}} = \underbrace{+(\nabla \bullet \mathbf{q}_{\mathrm{C}})}_{\substack{\text{Heat generation rate}\\ \text{by Conduction}\\ \text{per unit of volume}}} \underbrace{+\rho c_{\mathrm{P}}(\mathbf{u} \bullet [\nabla T])}_{\substack{\text{Heat generation rate}\\ \text{by Convection}\\ \text{per unit of volume}}} \underbrace{+(\nabla \bullet \mathbf{q}_{\mathrm{R}})}_{\substack{\text{Heat generation rate}\\ \text{by Radiation}\\ \text{per unit of volume}}} \tag{49}$$

As discussed previously, Fig. 7 represents the plume's control volume and Eq. (49) models the overall heat transfer from the fire to the surroundings. Hottel (1954) models this process with Eq. (50), so one can have

$$\underbrace{+\dot{Q}/(\pi D^{2}/4)}_{\substack{\text{Thermal flux}\\ \text{Total received by the}\\ \text{liquid pool emitted}\\ \text{by the fire column}}} = \underbrace{+(4k/D)(T_{\mathbb{F}} - T_{\mathrm{a}})}_{\substack{\text{Thermal flux}\\ \text{Conduction through}\\ \text{the edge}\\ \text{of the fire column}}} \underbrace{+h_{\mathrm{CV}}(T_{\mathbb{F}} - T_{\mathrm{a}})}_{\substack{\text{Thermal flux}\\ \text{Convection among the}\\ \text{products of the fire column}\\ \text{and the surroundings}}} \underbrace{+\sigma \mathcal{F}(T_{\mathbb{F}}^{4} - T_{\mathrm{a}}^{4})(1 - e^{-\mathscr{L}_{\lambda} D})}_{\substack{\text{Thermal flux}\\ \text{Radiation between the}\\ \text{fire column and the surroundings}}} \tag{50}$$

5.6. Vaporization velocity and the combustion Froude number

The burning rate $\dot{m}_{\mathrm{v}}''$ expresses the pool vaporization. It receives heat transfer contributions from seawater to LGN and radiation of pool fire within the plume. Local atmospheric conditions near to the freezing temperatures of water may occur due to fast depressurizations. Therefore, it is plausible to have formation of ice and/or hydrate when the water temperature is near 273 K (and even at warmer temperatures). In this model, we assume that the hydrates stability will decrease significantly with warmer water and surrounding agitation, such as, from the spill itself and/or ocean conditions. We also assume that the heat flux from the flame melts the ice/hydrate layer or prevent its formation even in near water-freezing temperatures. Thus, one can consider that

$$\dot{m}''_{\mathrm{v}} = \dot{m}''_{\mathrm{b}} + \dot{m}''_{\mathrm{r}} \tag{51}$$

where the vaporization of the cryogenic in the pool is related to $\langle \dot{y} \rangle$ and ρ_{l}, as cited by ABS (2004) as

$$\dot{m}''_{\mathrm{v}} = \langle \dot{y} \rangle \rho_{\mathrm{l}} \tag{52}$$

Esteves and Parise (2013a,b) discuss thoroughly these parameters and this work uses experimental values $\dot{m}''_{\mathrm{v}}$ and $\langle \dot{y} \rangle$ from the open literature[10]. Equation (52) converts one into the other, assuming the cryogenic liquid density as $\rho_{\mathrm{l}} = 422.5$ kg/m³. The normal boiling temperature of LNG is T_{b} = 111.7 K at atmospheric pressure and sea level of P_{a} =102.3 kPa. The latent heat of vaporization at these conditions is $\Delta H_{\mathbb{V}_{\mathrm{L}}}$ = 509.3 kJ/kg (FERC, 2004; ABS, 2004). The dry bulb temperature of the ambient air and water are, respectively, $T_{\mathrm{a}} = 293$ K, and $T_{\mathrm{w}} = 293$ K. Esteves and Parise (2013a,b) implement the TMS (2006) and Raj's (2007b) equations in the model, and this work follows this procedure, referring to the thermal plume of Fig. 7.

The effects of the wind follow the equation

$$U^*_{10} = \frac{U_{\mathrm{wind},10}}{\left[\left(\dot{m}''_{\mathrm{v}} / \rho_{\mathrm{a}}\right) g D_{\mathrm{p\,ci}}\right]^{1/3}} \tag{53}$$

The combustion Froude number is calculated as

$$Fr_{\mathbb{C}} = \frac{\dot{m}''_{\mathrm{v}}}{\rho_{\mathrm{a}} \sqrt{g D_{\mathrm{p_{ci}}}}} \tag{54}$$

5.7. Geometry and height of the 'visible' plume

Based on field experiments of Thomas (1965, 1963), tests performed in China Lake, Cal. (Raj, 2005), and in the Montoir, France, LNG terminal (Raj, 2007a; TMS, 2006; Malvos and Raj,(2006) Raj (2007a) proposed the following equations for the mean height (length) of the 'visible' solid fire column, being Eq. (55) for vertical and Eq. (56) for tilted plumes.

$$\frac{L_{\mathbb{V}}}{D^{\mathrm{eq}}_{\mathrm{p_{ci}}}} = 55\, Fr_{\mathbb{C}}^{\;2/3} \qquad \text{for} \qquad U^*_{10} \le 1 \tag{55}$$

$$\frac{L_{\mathbb{V}}}{D^{\mathrm{eq}}_{\mathrm{p_{ci}}}} = 55 \left(\frac{\dot{m}''_{\mathrm{v}}}{\rho_{\mathrm{a}} \sqrt{g D^{\mathrm{eq}}_{\mathrm{p_{ci}}}}} \right)^{2/3} \left\{ \frac{U_{\mathrm{wind},10}}{\left[\left(\dot{m}''_{\mathrm{v}} / \rho_{\mathrm{a}}\right) g D^{\mathrm{eq}}_{\mathrm{p_{ci}}}\right]^{1/3}} \right\}^{-0,21} \qquad \text{for} \qquad U^*_{10} > 1 \tag{56}$$

Based on the Albuquerque tests, SNL (2011) proposes an equivalent equation to model the geometry of pool fires. Fundamentally, Sandia uses the same parameters as the Raj (2007a) correlation uses for solid flames[11],

[10] 0.00021 (Quest, 2003, 2001), 0.0003 (SNL, 2008a,b; 2004), 0.000324 (TMS, 2006; Raj, 2007a,b,c), 0.000473 (Johnson and Cornwell, 2007; ABS, 2004), 0.000667 (FERC, 2004; ABS, 2004), 0.0008 (SNL, 2008a,b, 2004), 0.000852 (FERC, 2004; ABS, 2004) and 0.0011 (Luketa-Hanlin, 2006).

[11] $\Delta H_{\mathbb{C}_{\mathrm{L}}}$ is computed separately in Eq. (69), producing the same physical effect.

$$\frac{H}{D} = 4.196\left[\frac{\dot{m}''_{\mathrm{v}}\,\Delta H_{\mathbb{C}_{\mathrm{L}}}}{\rho_{\mathrm{a}} T_{\mathrm{a}} c_{\mathrm{P_a}} \sqrt{g}\left(D_{\mathrm{p\,ci}}\right)^{5/2}}\right]^{0.539} - 0.930 \tag{57}$$

SNL (2011) reports uncertainties of 8% (2 standard deviations) on the flow measurements and 10% on the flame height data. The tests were performed at different locations, elevations (sea level at Montoir with an ambient pressure 17% lower than that of Albuquerque, N. Mex.) and weather conditions. Albuquerque tests were performed in water reaching a pool fire of 56 m (from a spilled pool of 83 m), the larger diameter to date, whereas Montoir was on land, with diameter of 35 m.

Despite of these differences, this work follows the Raj's proposition. With our model, it is possible to correlate other equations and results from the works available in literature. Thus, whenever possible along this work, we incorporate the important results from the Albuquerque tests.

We anticipate here at this stage that Figure 18 ahead focuses on this aspect, showing that the fire column geometries described by the Equations (55) and (57) provide equivalent results, giving the uncertainties of this process.

5.8. Extended diameter and drag ratio caused by the fire column drag

Another phenomenon considered in this work was the drag caused by the wind, i.e. the extended diameter of the solid flame. This effect modifies the shape of the diameter of the pool fire from circular to elliptical. The drag of the flame is important, since as it deforms the fire base and changes the view factor of the flame relative to the receiver object (target).

The higher the configuration factor, the greater will the thermal radiation transport be, in the open field that surrounds the thermal plume. Usually this effect is reported as 'drag ratio', otherwise, the ratio between extended diameters of the thermal plume to the diameter thereof in the 'calm' wind condition. The drag is therefore strongly dependent on wind speed. Its effects were studied in the 'Montoir' test, and it is modeled considering the Froude number calculated with the local wind, $U_{\mathrm{wind,10}}$, at the height of 10 m above the ground where the pool fire takes place, according to TNO (2005). The drag is modeled in Woodward and Pitblado (2010).

$$Fr_{\mathbb{C},10} = \left(U_{\mathrm{wind,10}}\right)^2 \big/ g\,D_{\mathrm{p\,ci}} \tag{58}$$

$$Drag = D_{\mathrm{ext}} = D_{\mathrm{p_{ci}}}\,1.5\left(Fr_{\mathbb{C},10}\right)^{0.069} \tag{59a}$$

To calculate the flame drag, ABS (2004) uses the NFPA (1995) equation (22)[12] (*) of Section 3, Chapter 11:

$$Flame\ drag = D_{\mathrm{ext}} = D_{\mathrm{p_{ci}}}\,1.25\left(\frac{U^2_{\mathrm{wind}}}{g\,D_{\mathrm{p_{ci}}}}\right)^{0.069}\left(\frac{\rho_{\mathrm{v}}}{\rho_{\mathrm{a}}}\right)^{0.48} \tag{59b}$$

$$Drag\ ratio = D_{\mathrm{ext}} \big/ D_{\mathrm{p_{ci}}} \tag{60}$$

Woodward and Pitblado (2010) p. 253, discuss the best equation to model an extended pool diameter. On the other hand, this study compares the Moorhouse (1982a,b) and Lautkaski (1992) correlations adopting eight values of burning rate ($\dot{m}''_{\mathrm{v}}$), and with these values, tests circular pools of 35 m diameters.

The present work calculates Froude's number with those vaporization mass flow rates, considering the LNG vapor with density of 1.751 kg/m³ and air with density of 1.178 kg/m³. From these tests, the following conclusions are withdrawn:

- The equation of Mudan (1984) has the 'density' term reversed; that is, the right is the fuel vapor density should appear in the numerator and the air density in the denominator instead. This work uses the correction;
- To include a correction, multiplying the term of the Froude number by 1.2 and reverting the densities ratios as proposed by Moorhouse (1982a,b), Moorhouse and Pritchard (1982) and Lautkaski (1992). Woodward and Pitblado (2010) treat it in the same fashion in Eqs. 9:31 and 9:32 (*), p. 253;
- Calculating drag ratios with Moorhouse (1982a,b) and Lautkaski (1992) models and Froude numbers between 0.004139 and 0.02168 present deviation of +3.33%. The same result one obtains with Woodward and Pibladio (2010) model and Froude numbers between 0.03 and 0.01
- Esteves (2010) finds drag ratios of 1.05 (as of Table 5.3) using the equations from (58) to (60) and burning rates of 0.334 kg/m².s (vaporization velocities of 0.0008 m/s). This work finds 1.09, corresponding to a deviation 4.2%, which is acceptable in terms of uncertainties.

[12] From now on, the numbers and/or letters adjoining to the references cited in the present work, refer to those written and cited by the original authors. They are designated with (*).

Therefore, this work concludes to adopt the Lautkaski's (1992) correlation, according to Eqs. (59a) and (59b) compiled from Eq. 9:31 (*) of Woodward and Pitblado (2010).

5.9. Flame inclination (*tilt*)

The flame will not remain vertical with significant wind action. This effect will pose an inclination angle, relevant to evaluate the emitted radiation field. The flame inclination (tilt) usually can be determined with the equation of Welker and Sliepcevich (1966), as presented by TNO (2005), as well as by Woodward and Pitblado (2010),

$$Tilt\,angle = \frac{\tan\phi}{\cos\phi} = 3.3Fr_{\mathbb{C},10}{}^{0.8}Re_{10}^{0.07}\left(\rho_{\mathrm{v}}/\rho_{\mathrm{a}}\right)^{-0.6} = 3.3\left(\frac{U_{\mathrm{wind},10}^{2}}{gD_{\mathrm{p_{ci}}}}\right)^{0.8}\left(\frac{D_{\mathrm{p\,ci}}U_{\mathrm{wind},10}\,\rho_{\mathrm{a}}}{\mu_{\mathrm{a}}}\right)^{0.07}\left(\rho_{\mathrm{v}}/\rho_{\mathrm{a}}\right)^{-0.6} \quad (61)$$

Following Woodward and Pitblado (2010), it is necessary to calculate of the Reynolds number with wind speed 10 m above the base, so

$$Re_{10} = \frac{D_{\mathrm{p\,ci}}U_{\mathrm{wind,10}}}{\upsilon_{\mathrm{a}}} \quad (62)$$

in addition, according to TNO (2005) one can calculate the flame tilt in radians as

$$Tilt\ angle\left[\mathrm{rad}\right] = \arcsin\left\{\frac{\left[4\left(\tan\phi/\cos\phi\right)+1\right]^{0,5}-1}{2\left(\tan\phi/\cos\phi\right)}\right\} \quad (63)$$

On the other hand, the American Gas Association (AGA) (1974, 1973) proposed another correlation to determine the flame tilt as recommended by Beyler/NFPA (2002), as follows:

$$\cos\phi = \begin{cases} 1 & \text{for } U_{1.6}^{*} < 1 \\ 1/\sqrt{U^{*}} & \text{for } U_{1.6}^{*} \geq 1 \end{cases} \quad (64)$$

The Welker and Sliepcevich (1966) equation proved to be the most appropriate for the calculation of the flame tilt. It provides the slightest inclination after comparison with six other equations of the current literature.

We considered that the smaller the slope, the larger the geometrical configuration factor will be, and the receiving object will "see" a larger portion of the flame. Ultimately, when the flame does not tilt by the wind action ($\phi \to 0$), targets receive the higher radiation emitted by the fire column, thereby increasing the safety zone around the terminal. Under this account and from the safety point of view, this correlation showed to be the best option, reason why this work adopted it in detriment of the AGA's correlation. We compared it with other six equations of the open literature.

To confirm it we performed a parametric analysis. We simulated the tilts with seven vaporization velocities[13] and wind velocities of 2, 4 and 6 m/s consistently with the Pasquill's B, C and D categories for atmospheric stability. Initially, the test used a wind velocity of 10 m/s, however the flame extinguished, as expected, because the atmospheric stability reached with velocities up around 4 m/s. This wind velocity did not support the combustion process with Froude numbers close to zero. This value does not allow any burn rate in the region of "visible" combustion, due to the entry of more air than necessary into the lateral side of the fire plume, with adequate velocity to sustain the combustion.

On the other hand, simulations with the TNO equations provided high values of tilt, and for this reason, have not been used either. Simulations used in this comparison considered pools with diameters of 10, 20, 35 100 and 300 m, and the values found for the diameter of 35 m were consistent with those found by Raj (2007a,b) in the China Lake, Cal., tests.

6. Modelling the thermal radiation fields

6.1. (Time average) Surface Emissive Power (*SEP*) of the fire column

The Equations (55), (56) or (57) demonstrates that gravitational forces (buoyancy) counterbalance the wind effects (inertia). Low Froude numbers govern the geometry of turbulent diffusion fire columns, giving them a low buoyancy profile. Therefore, the higher the wind effect, the lower the plume length and burning velocity, for the same plume diameter. In addition, for the same

[13] of 0.0021, 0.0003, 0.000324, 0.000473, 0.000667, 0.0008 and 0.0011 m/s.

reason, the lower the wind effects, the higher the plume length. Bottom 'clean burning zone' length, $L_{\mathbb{C}}$, and ratio $\psi = L_{\mathbb{C}}/L_{\mathbb{V}}$ were correlated experimentally with data acquired from the tests with land pool fires with 35 m diameter at Montoir Terminal (Malvos and Raj, 2006).

The results show that the $L_{\mathbb{C}}$ length near fire column base was small (about 10 m, or 15 %) when compared to the overall 66 m length of the fire column. TMS (2006) and Raj (2007a,b) developed then Eqs. (65) and (66) defining the fire plume parameters as $L_{\mathbb{C}}$, $L_{\mathbb{V}}$, $L_{\mathbb{I}}$, $\psi = L_{\mathbb{C}}/L_{\mathbb{V}}$ and $Fr_{\mathbb{C}}$.

$$\psi = \frac{L_{\mathbb{C}}}{L_{\mathbb{V}}} = \left(1 - \frac{L_{\mathbb{I}}}{L_{\mathbb{V}}}\right) = 0.70 + \log_{10}\left[\left(Fr_{\mathbb{C}}\right)^{1/4}\right] \tag{65}$$

$$L_{\mathbb{I}} = (1-\psi) L_{\mathbb{V}} \tag{66}$$

The effective surface emissive power in the smoke is produced in the inner parts of the thermal plume due to the incomplete combustion of fuel by the reduced oxygen concentration in the fire core. Thus, only a fraction of the radiation is transmitted to the nominal flame surface. This attenuation, E_{s}, on the emitted effective radiation, is due to τ_{s} that reduces E_0 where the 'clean' combustion takes place, giving

$$E_{\mathrm{s}} = E_0\, \tau_{\mathrm{s}} \tag{67}$$

The smoke transmissivity depends on parameters of particulate material (soot) partially glowing within the plume during the fire. , as well as of optical properties of the luminous energy emitted by the fire plume, such as $A_{\mathscr{L}}$, C_{S} and L_{beam}. As $A_{\mathscr{L}}$ and L_{beam} which in general depend on λ, TMS (2006) and Raj (2007a,b,c) proposed the following equation, to correlate the total hemispheric transmissivity independently of λ

$$\tau_{\mathrm{s}} = e^{-\left(A_{\mathscr{L}}\, C_{\mathrm{S}}\, L_{\mathrm{beam}}\right)} \tag{68}$$

Experimentally, (Raj, 2007a,b) demonstrated that C_{s} is related to ρ_{a}, Y, $\Re$, η, $\Delta H_{\mathbb{C}_{\mathrm{L}}}$ and $c_{P_{\mathrm{a}}}$. It is given by the correlation proposed by Raj (2007a,b,c) and TMS (2006), as follows

$$C_{\mathrm{s}} = \rho_{\mathrm{a}}\, Y \frac{1}{1 + \left(\Re/\eta\right) + \left[\Delta H_{\mathbb{C}_{\mathrm{L}}} / \left(c_{P_{\mathrm{a}}} T_{\mathrm{a}}\right)\right]} \tag{69}$$

Based on the results of the China Lake and Montoir field tests, Raj (2007a,b,c) recommended that the length of the optical beams of cylindrical fires, L_{beam}, is 63 % of $D_{\mathrm{p_{ci}}}^{\mathrm{eq}}$. One can write the Eq. (70) as follows

$$L_{\mathrm{beam}} = 0.63 D_{\mathrm{p_{ci}}}^{\mathrm{eq}} \tag{70}$$

According to experiments carried out by Notariani et al. (1993) with oil fires, with pool diameters varying between 1 and 17 m, an empirical correlation between Y and $D_{\mathrm{p_{ci}}}$ for LNG fires it was proposed such as

$$Y = 9.412 + 2.758\, \log_{10}\left(D_{\mathrm{p_{ci}}}\right) \tag{71}$$

This equation, as presented by Raj (2007a,b), Y was expressed in %, while the right side expresses the decimal logarithm of the pool diameter. Raj (2007a,b) expressed it as a mass fraction in percentage basis. As this is a correlation obtained experimentally, where 9.412 and 2.758 coefficients are valid only if $D_{\mathrm{p_{ci}}}$ is measured in meters, Y. It was used by Raj (2007a,b) as an expression as a percentage.

Even though Notariani et al (1993) used oil fires, TMS (2006) considered that, until its publication, the knowledge this correlation aggregates seems to be an adequate proxy, providing the results of the Montoir terminal with LNG pools with diameters of 35 m. The results of this correlation fitted the model proposed for pool fires, in which the radiation emitted by the fire column varied along its axis length. TMS (2006) and Raj (2007a,b) developed a model postulating that there is a probability, $0 \leq p(\xi) \leq 1$, of the fire column surface irradiates in the intermittent zone just above the 'clean' combustion zone (consequently $L_{\mathbb{I}} > L_{\mathbb{C}}$). This probability can be interpreted as the fraction of the time that the outer layers of the cylindrical fire 'show the inner core' of the plume irradiating energy (light) thus at the maximum *SEP*. The remainder of the time the emission is from remaining smoke layers of the thermal plume. Such a probability was proposed to be modeled by a polynomial function whose order would be a function given by the power $\mathfrak{n}$. It was calibrated ('best fit') to the experiments with the 35 m diameter of Montoir terminal LNG fire tests. The value of ξ is obtained by the equations proposed by TMS (2006) and Raj (2007a,b), so

$$p(\xi)=1 \qquad \text{for} \quad 0 \leq \xi \leq \psi \tag{72}$$

$$p(\xi)=\left(\frac{1-\xi}{1-\psi}\right)^{\mathfrak{n}} \qquad \text{for} \quad \psi \leq \xi \leq 1 \tag{73}$$

Thus, one has

$$\xi = \frac{Z}{L_{\mathbb{V}}} = \frac{\text{Length along the axis of the fire column}}{\text{Length of the 'visible' fire column}} \geq \psi \tag{74}$$

Examining the Equations (65) and (74), which are, respectively, $\psi = L_{\mathbb{C}}/L_{\mathbb{V}}$ and $\xi = Z/L_{\mathbb{V}}$, and dividing one by the other, we reach $\xi/\psi = Z/L_{\mathbb{C}}$. Analyzing the Equations (51), (56) and (65), one concludes that the governing parameters of the thermal column geometry are the vaporization mass flow rate, $\dot{m}''_{\mathrm{V}}$, and the combustion Froude number, $Fr_{\mathbb{C}}$

TMS (2006) and Raj (2007a,b) modelled the flame surface emissive power as a time averaged quantity, $\bar{E}$. On this account, only a fraction of the emissive power at the base of the fire column, E_0, would irradiate to the surroundings expressed as follows:

$$\frac{\bar{E}}{E_0} = \psi + \left[\frac{1+\mathfrak{n}\ e^{-\left(A_{\mathscr{L}}\, C_{\mathrm{s}}\, L_{\mathrm{beam}}\right)}}{1+\mathfrak{n}}\right](1-\psi) \tag{75}$$

The best adjustment of the data acquired with the LNG fires tests of 35 m diameter made in the Gaz de France's Montoir terminal, was obtained when $\mathfrak{n}=3$ (TMS, 2006; Raj, 2007a,b). The parameter $\bar{E}$ depends on the diameter of the fire column, D, and the spectral optical thickness, κ_{λ}, according to the experimental results acquired with China Lake tests (Raj, 2007a,b; TMS, 2006). This optical thickness represents the reduction that the fire plume experiments in its maximum capacity to irradiate luminous energy during the fuel burning. It considers the combustion inefficiencies and the presence of particulate material in soot (combustion products). Based on optical properties, the time average of the total hemispheric emissivity is calculated as

$$\bar{\varepsilon} = 1-e^{-\left(D_{\mathrm{pci}}/\kappa_{\lambda}\right)} \tag{76}$$

TMS (2006) determined the maximum emissive power at the base of the fire, $E^{\max}$, as being 325 kW/m², equivalent of a blackbody, based on the data acquired from site experiments in China Lake and Montoir terminal. This value is supposed to be equivalent to a blackbody with temperature irradiating with 1,547 K. Thus, emissive power at the firebase can be determined, providing the concept that the spectral optical thickness is the inverse of the extinction coefficient, $\kappa_{\lambda} = 1/\mathscr{L}_{\lambda}$ (Siegel and Howell, 2001).

$$E_0 = E^{\max}\left[1-e^{-\left(D_{\mathrm{pci}}/\kappa_{\lambda}\right)}\right] = E^{\max}\left[1-e^{-\left(D_{\mathrm{pci}}\,\mathscr{L}_{\lambda}\right)}\right] \tag{77}$$

LNG pool fires are 'optically thick', due to the presence of soot particles in turbulent diffusion fire plumes of flow buoyancy (Fay, 2006; TMS, 2006; Raj, 2007a,b). Based on this, rather, the plume irradiates as a black body in the region of higher thermal emission. In other words, at the bottom of the plume near the burning substrate, is the region of the fire emitting the greatest thermal radiation.

6.2. Fields of the emitted thermal radiation

The modeling is based on the previous work developed by Esteves and Parise (2013a,b), where the action of wind was not considered. The pool fire generates a time average surface emissive power resulting in a thermal radiation field that propagates in the surrounding atmosphere and strikes the surroundings resources. The model evolved considering not only the presence of the wind (drag) but the fire column inclination (tilt) as well.

The atmosphere attenuates effects of thermal radiation fields emitted by pool fires with a given wavelength**.** This attenuation is a function of: (i) air transmissivity, (ii) path length between emitter and targets, (iii) the geometric configuration (view) factor and (iv) the relative position between both. The equations developed are general for vertical or inclined cylindrical flame, considering the target on the ground or above, which may also be vertical, horizontal or inclined.

To assess the radiation that strikes on the surroundings, it is necessary to know some parameters to determine its vulnerabilities at a given distance from the edge of pool fire. It provides subsides for the decision-making about where to locate a cryogenic terminal. The model calculates in a 'direct format' the variables of interest for an object located at a pre-determined distance from the pool fire. Therefore, it is possible to assess the thermal dose striking on neighboring targets/assets, well as their vulnerabilities, in percentage of the resource affected and the as well as the potential harm in terms of lethality, first and second degree burns.

In the same fashion, it is possible to calculate parameters with 'reverse format'. For example, if one knows beforehand the allowable flux for a given resource and that the Authorities define, and then it is possible to calculate the percentage and the type of vulnerability of the impact. Thus, the corresponding radius centered in the pool fire or its edge can be determined. If the thermal flux surpasses the Authorities' requirement, it is necessary to perform an iterative calculation using longer distances until both values match.

The open literature defines levels for the vulnerabilities (1, 5, 50, 90 and 99%) for lethality, first, second degree burns. With the aid probit tables, it is possible to assess different percentages, discussed ahead.

6.3. Thermal flux

Mathematically, the rigorous model is established, for example, by Raj e Atallah (1974), calculating the thermal flux that comes out from a solid pool fire plume. The combustion is supposed to be of turbulent diffusion, which radiation takes place in open field with no obstacles. So one has

$$\dot{q}'' = \int_{V_F} \int_{\lambda=0}^{+\infty} \frac{c_1 \kappa_\lambda \left[\exp\left(-\int_0^r \kappa_\lambda \, d\kappa_\lambda \right) \right] \lambda^{-5} \cos\phi \, dV_F \, d\lambda}{\left[\exp\left(c_2 / \lambda T \right) - 1 \right] \left(\pi r^2 \right)} \tag{78}$$

The integration covers the total energy spectrum and fire column volume. It is necessary to have the complete distribution of flame temperature fields as well the time average fluctuations of the flames elements, wavelengths and time distributions of the attenuation coefficients. In the same fashion, it is equally required to describe the concentrations of all chemical species which absorb and emit energy [CO_2, H_2O (v) and soot]. A simplification was introduced by Raj (2007c) using the concept of spectral emissive power $\bar{E}_{\lambda_i}(\lambda)$, such as

$$\dot{q}'' = \sum_{i=1}^{N} \mathcal{F}_{dA_i \to A_j}^{\text{view}} \int_{A_i} \int_{\lambda=0}^{+\infty} \left[\bar{E}_{\lambda_i}(\lambda) \cdot \tau_\lambda(\lambda) \, d\lambda \, dA_i \right] \tag{79}$$

The model considers that $\mathcal{F}_{dA_i \to A_j}^{\text{view}}$ varies in the interval $0 \le \mathcal{F}_{dA_i \to A_j}^{\text{view}} \le 1$. It is the contribution of the view factor of the i^{th} area element located at the external flame's surface that is 'seen' by the receptor target/asset j outside the flame. The view factors are calculated in accordance with the methods published in the open literature [Siegel and Howell (2001); Sparrow and Cess (1978); Hottel and Sarofim (1967); Hottel (1954)].

6.4. Geometric configuration (view) factor

For two finite areas, A_i and A_j, the calculation of the reciprocal factor is computed as presented in Fig. (10) and Eq. (80).

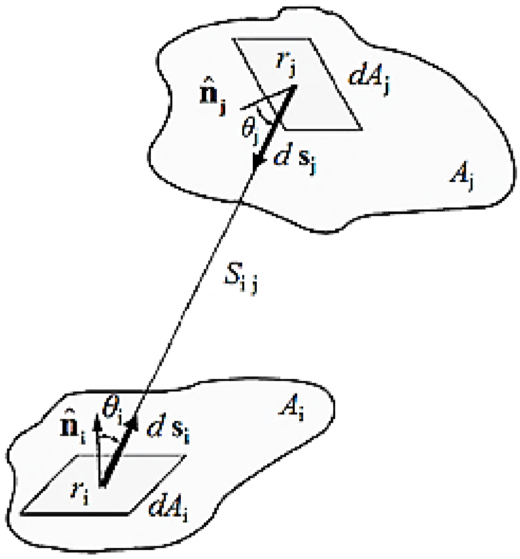

Fig. 10 – Evaluation of the view factor between two surfaces. Adapted from: Bejan and Krauss (2003)

$$A_i \mathcal{F}^{\text{view}}_{A_i \to A_j} = A_j \mathcal{F}^{\text{view}}_{A_j \to A_i} = \int_{A_i} \mathcal{F}^{\text{view}}_{dA_i \to A_j} dA_i = \frac{1}{2\pi} \oint_{\Gamma_j} \left[\int_{A_i} \frac{(y_j - y_i)n_i - (z_j - z_i)m_i}{S^2} dA_i \right] dx_j + \frac{1}{2\pi} \oint_{\Gamma_j} \left[\int_{A_i} \frac{(z_j - z_i)l_i - (x_j - x_i)n_i}{S^2} dA_i \right] dy_j + \frac{1}{2\pi} \oint_{\Gamma_j} \left[\int_{A_i} \frac{(x_j - x_i)l_i - (y_j - y_i)m_i}{S^2} dA_i \right] dz_j \quad (80)$$

The view factor considers two smooth, continuous and finite surfaces, A_i and A_j. They are enclosed by two differentiable, continuous and closed contour lines of the finite surfaces, A_i and A_j, C_i and C_j, distant S_{ij} from each other. The vector elements $d\,\mathbf{s}_i$ and $d\,\mathbf{s}_j$ represent the contour lines of the finite surfaces to lower the integral order, in accordance with Fig. 10. The equation (81) simplifies the calculus. [Siegel and Howell (2001), Sparrow and Cess (1978), Hottel and Sarofim (1967), Hottel (1954)]

$$\mathcal{F}^{\text{view}}_{A_i \to A_j} = \frac{1}{A_j} \int_{A_i} \int_{A_j} \frac{\cos\theta_i \cos\theta_j}{\pi S_{ij}^2} dA_i dA_j \quad (81)$$

Using the Green's and Stokes' theorems (Kaplan, 2002; Kreizig, 1999), to low the order of the area quadruple integral of Eq. (81) converting it in a double line integral, such as Eq. (82).

$$A_i \mathcal{F}^{\text{view}}_{i \to j} = \frac{1}{2\pi} \oint_{C_i} \oint_{C_j} \ln S_{ij}\, d\,\mathbf{s}_j d\,\mathbf{s}_i \quad (82)$$

The finite surface area A_i delimits a smooth, continuous and closed contour curve C. It is defined by the functions $P(x,y,z)$, $Q(x,y,z)$ and $R(x,y,z)$, being differentiable twice at an arbitrary point (x,y,z) of its domain. At a given point of C the unit dyadic vector $\hat{\mathbf{n}} = l\,\hat{\mathbf{e}}_1 + m\,\hat{\mathbf{e}}_2 + n\,\hat{\mathbf{e}}_3$ is normal to the surface A_i and makes with the axes (x,y,z), respectively, the angles of the director cosines $l = \cos\alpha$, $m = \cos\beta$ and $n = \cos\gamma$ (Siegel e Howell, 2001; Sparrow e Cess, 1978, Kaplan, 2002). Analytically, we can write the Eq. (84).

$$\oint_{C}\left(Pdx+Qdy+Rdz\right)=\int_{A}\left[\left(\frac{\partial R}{\partial y}-\frac{\partial Q}{\partial z}\right)\cos\alpha+\left(\frac{\partial P}{\partial z}-\frac{\partial R}{\partial x}\right)\cos\beta+\left(\frac{\partial R}{\partial x}-\frac{\partial Q}{\partial y}\right)\cos\gamma\right]dA \quad (83)$$

The quadruple integral area of Eq. (81) can have its order lowered to a line double integral, in accordance with Eq. (84). Analytical integration around two curves C_i and C_j, the components of areas A_i and A_j the distance S calculate the view factor $\mathcal{F}^{\text{view}}_{A_i\to A_j}$ .as follows.

$$\mathcal{F}^{\text{view}}_{A_i\to A_j}=\frac{1}{2\pi A_i}\left(\oint_{C_i}\oint_{Cj}\ln S\,dx_i dx_j+\ln S\,dy_i dy_j+\ln S\,dz_i dz_j\right) \quad (84)$$

6.5. Coupling the models of SEP, view factor and local atmosphere transmissivity

6.5.1. SEP and view factor - Literature overview and discussions

The evaluation of the thermal radiation incident on an object outside the fire column involves three steps.

- Determine the geometric characteristics of the pool fire, i.e., combustion mass flow rate and physical dimensions ($L_{\text{ive}}/D_{\text{eci}}$).
- Calculate the average surface emissive power of the pool fire. The intensity of the emitted radiation depends on several factors: type and the fuel composition, size of fire and flame temperature;
- Determine the thermal radiation flux incident on a given location outside the plume. It depends on the fire column geometry, the radiant characteristics and the relative orientation of flame to the receiver. For large distances of hundreds of meters, the absorption of radiation by the atmosphere becomes important. It depends on the optical path length between flame and target, the flame temperature and local humidity in the atmosphere.

For this task, this work compared some consecrated models available in the open literature.

Beyer/NFPA (2002) use four methods of SFPE (1999) to calculate the thermal radiation emitted by a pool fire. Two of them are considered as simplified (screening) developed by (I) Shokri and Beyler (1989) and (ii) the classical models for point source flame. However, Shokri and Beyler (1989) and Mudan and Croce (1988) developed more refined models. For the present modelling, we are considering only detailed models in detriment of screening methods.

We considered as key factors the equations conciseness, low computational efforts/costs, plausibility of results, and follow the NFPA/SFPE calculation march. To make up our choice we focused our choice on the methodology in two consecrated models, that is, Shokri and Beyler (1989) and Mudan and Croce (1988).

The method of Shokri and Beyler (1989) simplifies the pool area calculus. It considers the Heskestad (1998, 1983) correlation $H=0.235\dot{Q}^{2/5}-1.02D$ used in point source models. In this equation, $\dot{Q}$ is the total rate of radiation emitted by the flame appearing as an independent variable. This is a simplification, since it does not consider the Froude number and the mechanisms of toroidal vortices formed in the region above the "clean" combustion zone of the plume. These (important) mechanisms are responsible for the natural draft of combustion products on the top of the fire column. It takes place by virtue of the turbulent diffusion generated by transportation of the combustion toroidal vortices formed. This mechanism generates the buoyancy in the lower part of the flame just above the 'rich combustion core'. This buoyancy governs the number of combustion Froude (balance between inertia and buoyance forces).

The correlation used to calculate the effective flame emissive power, $E=58(10^{-0.00283D})$, considers its decay as the pool diameter increases due to the smoke generation, but it proved not to fit well to LNG fires. When compared to the Mudan's correlation, $E=E^{\max}e^{-\mathrm{sD}}+E_{smk}[1-e^{-\mathrm{sD}}]$, it presented the worst spreading in predictions. Besides, it does not consider the flame emitting thermal radiation as a black body, as well as the flame's extinction and the smoke emissive power.

The Shokri and Beyler (1989) model considers 100% for the air transmissivity. For real situations, the surrounding atmosphere provokes an exponential decay on the transport process of thermal radiation to the environment. We will discuss this matter in Equation Eq. (85).

On the other hand, it has only four points to validate LNG fires up to 25 m in diameter, presenting thus considerable data scattering when for fire 'non-LNG' fires are compared. Finally yet importantly, it presented scaled up safety factors starting with 2, which casts some uncertainty on the quantitative determination. Therefore, due to simplification of the method as presented, it is plausible to infer that the results obtained with the Shokri and Beyler (1989) method could over predict the results, particularly for fires with diameters above 35 m, as used in the LNG Montoir's terminal and 56 m in Albuquerque, N. Mex. field tests.

On the other hand, the methods of Mudan (1984) and Mudan & Croce (1988) consider the transmissivity different from 100%. They use the Thomas (1963) first equation for vertical fire columns with dimensionless coefficient of 42 rather than 55 of the second equation (Thomas, 1965). For inclined flames, Mudan (1984) uses Thomas (1965) second correlation, used also for vertical flames, with the wind velocity term being equal to 1, given by Eq. (55). That is, the same adopted by the Raj (2007a,b) model as well as in the latest models for solid flames.

Mudan adopted the AGA (1974, 1973) correlation instead, given by Eq. (64) to calculate the flame tilt. Regarding the turbulent diffusion flame, Mudan used the Froude number to model the combustion toroidal vortexes, which is the most appropriate. The emissive power is equivalent to that of a blackbody in the base plume, which is the most adequate for large diameter pool fires, according to the field tests of Gaz de France's terminal and SNL (2011) tests in Albuquerque, New Mexico. Therefore, we will use the strategy and calculation march based on the model presented in Fig. 11.

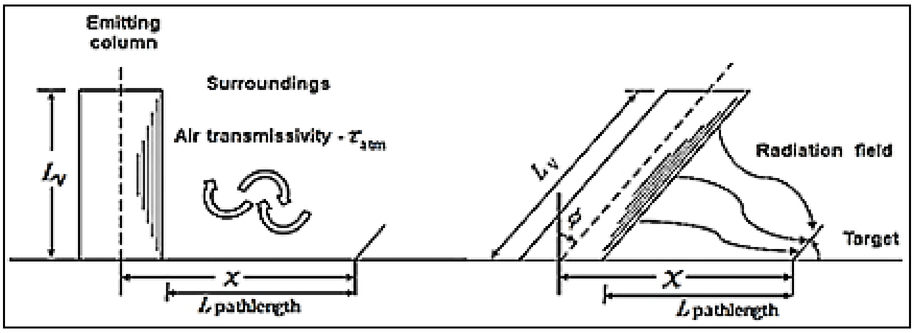

Fig. 11 – The fire column with the surrounding atmosphere and the receiving target. Adapted from Beyler/NFPA (2002)

Based on Eqs. (75) and (81), and according to Mudan (1984) and Beyler/NFPA (2002), Equation 21 (*), page 3-279, this work can calculate the thermal radiation incident on a target outside the flame using the governing equation:

$$\dot{q}'' = \langle E_{\text{eff}} \rangle \, \mathcal{F}_{1\to2}^{\text{view}} \, \tau_{\text{atm}} \tag{85}$$

The time average and effective emissive power, $\langle E_{\text{eff}} \rangle$, is equivalent to $\bar{E}$, as indicated by Eq. (75) based on Raj (2007a,b). According to that model, $\bar{E}$, takes into account experiments with pool fires of LNG and LPG on land, and LNG on water. They follow the Thomas (1965) equation, where the geometry of the flame follows the Eqs. (55) and (56), as per Esteves (2010) and Esteves and Parise (2013a,b). Otherwise, Mudan uses the equation $E = E^{\max} e^{-\text{sD}} + E_{\text{smk}} \left[1 - e^{-\text{sD}}\right]$ to model the phenomenon in an equivalent manner, but this work did not test it.

Mudan (1987, 1984) used two groups of equations to compute the configuration factor, one for vertical and other for tilted pool fires. If the fire is vertical: (I) the target is located on the ground or immediately above the top of the flame; in this case, a single cylinder represents the flame;

(ii) the target is located between the bottom of the pool fire (on the ground) and the top of the fire column; in this case, the flame is split into two cylinders, one below and the other above the target.

Mudan (1987) uses the Sparrow (1963) approach with line integrals to define a closed system of equations to calculate view factors for tilted pool fires. Beyler/NFPA (2002) and Mudan (1984) use the AGA correlation expressed by the Eq. (64) to calculate the flame tilt. It presents acceptable scattering in the results in the correlation of U^* with $\cos\phi$, being appropriate to calculate view factors. For an inclined fire column, one can calculate the vertical and horizontal components of the configuration factor in accordance with to the Eqs. (86-93) [Beyler/NFPA (2002)] as follows:

$$\pi \mathcal{F}_{\text{vert}}^{\text{view}} = \frac{a\cos\phi}{b - a\sin\phi} \cdot \frac{a^2 + (b+1)^2 - 2b(1 + a\sin\phi)}{\sqrt{AB}} \cdot \arctan\left[\sqrt{\frac{A}{B}} \cdot \left(\frac{b-1}{b+1}\right)^{1/2}\right] + \frac{\cos\phi}{\sqrt{C}} \cdot \left\{\arctan\left[\frac{ab + (b^2-1)\sin\phi}{\sqrt{b^2-1} \cdot \sqrt{C}}\right] + \arctan\left[\frac{(b^2-1)\sin\phi}{\sqrt{b^2-1} \cdot \sqrt{C}}\right]\right\} - \frac{a\cos\phi}{(b - a\sin\phi)} \cdot \arctan\left(\sqrt{\frac{b-1}{b+1}}\right) \tag{86}$$

$$\pi \mathcal{F}_{\text{horz}}^{\text{view}} = \arctan\sqrt{\frac{b+1}{b-1}} - \frac{a^2+(b+1)^2-2(b+1+ab\sin\phi)}{\sqrt{AB}} \cdot \arctan\left[\sqrt{\frac{A}{B}} \cdot \left(\frac{b-1}{b+1}\right)^{1/2}\right] + \frac{\sin\phi}{\sqrt{C}}\left\{\arctan\left[\frac{ab-(b^2-1)\sin\phi}{\sqrt{b^2-1}\cdot\sqrt{C}}\right] + \arctan\left[\frac{(b^2-1)^{1/2}\sin\phi}{\sqrt{C}}\right]\right\} \tag{87}$$

$$H = L_{\mathbb{V}} \tag{88}$$

$$a = 2L_{\mathbb{V}} / D_{\mathrm{p\,ci}}^{\mathrm{eq}} \tag{89}$$

$$b = 2\mathcal{X} / D_{\mathrm{p\,ci}}^{\mathrm{eq}} \tag{90}$$

$$A = a^2 + (b+1)^2 - 2a(b+1)\sin\phi \tag{91}$$

$$B = a^2 + (b-1)^2 - 2a(b-1)\sin\phi \tag{92}$$

$$C = 1 + (b^2-1)\cos^2\phi \tag{93}$$

The vector sum of the horizontal with vertical components of the view factor gives the total view factor

$$\mathcal{F}_{1\to2,\max}^{\text{view}} = \sqrt{\left(\mathcal{F}_{1\to2,\text{ horz}}^{\text{view}}\right)^2 + \left(\mathcal{F}_{1\to2,\text{ vert}}^{\text{view}}\right)^2} \tag{94}$$

Zero tilts reduce the Eqs. (86) and (87) to the equations 23a and 23b (*), respectively, as the way they were recommended by Beyler/NFPA (2002) on pages 3-280/281 and 3-281.

We searched on consecrated textbooks, open literature and catalogs[14], trying to find computational tools to model view factors for realistic shapes as those found in the engineering work. In other words, targets with geometries similar to cylindrical columns with finite heights, parallelograms, cubes, spheres, prisms. The results were scarce and limited to few cases of not tilted parallel cylinders with equal diameters and cylinders with infinite heights and same diameters. This geometric configurations obviously did not match the present model, reason why they could not been considered. This might be the reason why most references consider the target receiving radiation, such as flat plates being located at the ground level or higher.

6.5.2. Local atmosphere transmissivity - Literature overview and discussions

When a fire column emits thermal radiation to the local environment, there are some effects. There are interactions with humidity and transmissivity of the air, resulting, consequently, in attenuation of its intensity due to absorption and molecular diffusion. The main constituents of the air responsible for this attenuation are H_2O (v) and CO_2.

This report revise, investigates and tests a comprehensive set of correlations[15]. The main premise is that the fires emit radiation as black bodies with the absorvities computed in the bands of H_2O (v) and CO_2 (v), although other equations include the effect of scattering of the radiation in the atmosphere.

Hottel and Sarofim (1967) developed sets of these curves and published it in abacuses. Based on it, Beyer/NFPA (2002) developed graphs with curves of atmospheric emissivity but they seem to be limited as a computational tool. An additional work of get data in digital spreadsheets would be necessary. Those authors introduced the parameter $P_{\mathrm{H_2O(v)}}^{\mathrm{sat}}(T_{\mathrm{a}})$ with maximum value of 6.10 at the saturated condition of the water vapor, which limits its use. TNO (1992) used $1{,}000 \le P_{\mathrm{H_2O\,(v)}}^{\mathrm{sat}}(T_{\mathrm{a}})\cdot \mathcal{L} \le 1{,}000{,}000$ Pa.m.

SNL (2011) discusses the effects of the atmosphere on the transmissivity. For the same path length, the lower relative humidity, the higher the transmissivity will be; and the higher the path length, lower thermal radiation flux will strike on the surrounding targets and the safer the terminal location will be.

We did a comparison between Wayne (1991) and SNL (2011) data. The results indicate that both relative humidity and atmospheric temperatures are not applicable in the range between 256 K and 373 K. Therefore, it is necessary to use an additional and intermediate step to calculate the saturated water vapor pressure using Antoine's equation with other subsequent coefficients.

[14] Martinez (2014), Howell and Mengüç (2011), Bopche and Sridharan (2009), Kern (1999), Juul (1982), Wiebelt and Ruo (1963).
[15] SNL (2011), MKOPSC (2008), Raj (2007a,b), TMS (2006), Mannan/Lees (2005), TNO (2005), ABS (2004), Beyler/NFPA (2002), AIChE (2000), Mudan (1984), Hottel and Sarofim (1967), Hottel (1954).

It redounds in an implicit process of $H_2O(v)$ and $CO_2(v)$ contents as functions of the path lengths and temperatures. This interactive process requires convergence of results to solve implicit values, reason why we did use this method in the present work.

TMS (2006), based on Raj (1977a,b), correlated the transmissivity as a direct function of path length. They sustained that the partial pressure of the water and the transmissivity decreases with the increase of several other parameters[16]. As positive factor of this correlation is that TMS (2006) considers the d path lengths varying in a wide interval of 1 and 10,000 m, counted from the outside surface of the fire plume, propagating in the atmospheric air. This fits with the majority of open fires in the industry that occurs in that range.

Based on literature, one can develop a comparison of those models, compiling graphs and equations from references. The key points are: (i) SNL (2011), (ii) TMS (2006) Fig. 3-4, p. 99, with relative humidity of 20, 50, 60, 80 (extrapolated) and 100% with path lengths of 1; 10; 100; 1,000; 10,000 m; (iii) TNO (2005), equation 6.29 (*), p. 6:50; (iv) AIChE (2000), equations 2.2.42 and 2.2.43 **(*)** p. 209 and (v) Wayne (1991). The results shown in Fig. 12 and the curve of 80% was used to prepare the Fig. 13

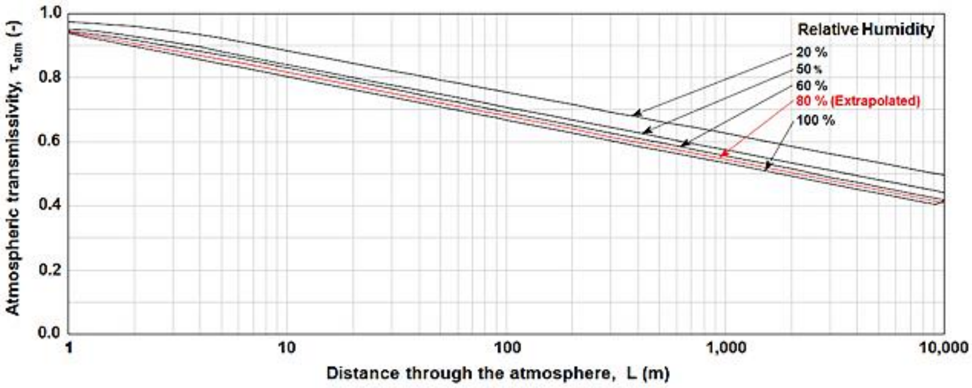

Fig. 12 – Average transmissivity – 80%. Adapted from TMS (2006).

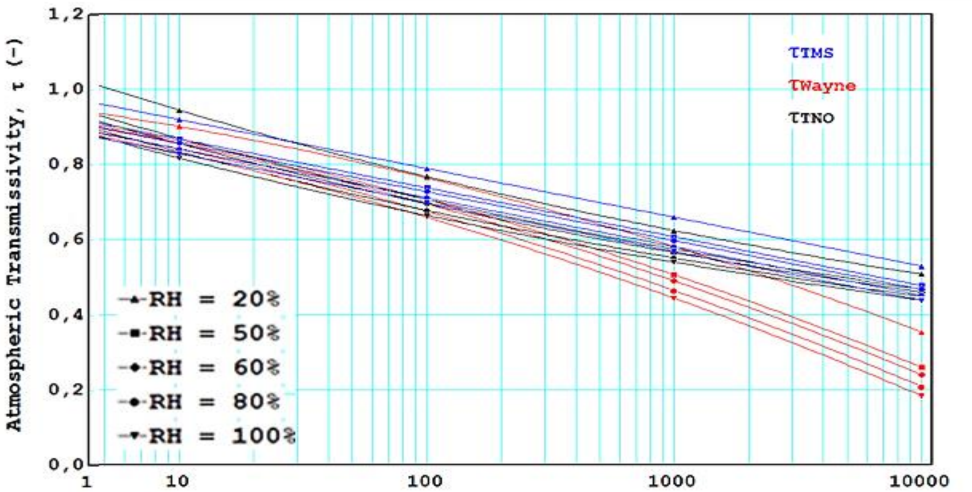

Fig. 13 – Atmospheric transmissivity comparison

From these comparisons, we withdraw the following key points:

- The TNO and TMS curves presents transmissivity values of the same order of magnitude throughout the whole atmospheric path length;
- As expected, the 20% RH curve shows the highest transmissivity for the three references, since lower water vapor content in the atmosphere provokes less scattering of energy;
- Upon reaching the path length of 10,000 m (strong effects of the surrounding atmosphere), the Wayne curves between RHs of 50 and 100% converged to transmissivities between 0.18 and 0.36, respectively; while the TMS curves fell to a range of 0.4-0.5. The decrease of Wayne curves is steeper than the TNO and the quasi-linear TMS, because it is plausible to expect that at a path length of 10,000 m, there is more absorption and scattering of thermal radiation;
- Lower heat flux values imply smaller exclusion zones and greater response times, facilitating the evacuation in emergency situations;

[16] One can mention as examples: relative humidity, atmospheric temperature, water content between 240 and 373 K, and relative humidity. For the later value, the partial pressure of water vapor was found to be exactly equal to 1 atm (101,325 N/m² or 101.325 kPa), according to Mannan/Less (2005).

- On the other side of the interval, with path lengths close to the edge of the fire column (1 m or closer, i. e., where the atmosphere effects is practicably null), TMS transmissivities is in the range of 0.97 (100 %) and 0.99 (20 %). Wayne and TNO also presented similar values;
- The TMS curves appears above Wayne's model curves, since TMS equations considers the absorvity caused by water vapor only, while Wayne's model includes both $H_2O(v)$ and $CO_2(v)$, i.e., TMS considers less scattering of thermal radiation.

Similar comparisons one can also test to obtain the best compromise with plausibility of results considering path length, partial water vapor pressure in the atmosphere and transmissivity, using the AIChE (2000) correlations. When one considers thermal fluxes of 5 kW/m², some results presented high variances from each other, i.e., long path lengths scattered substantially the results. Using their correlations, one has:

$$P_{\mathrm{H_2O(v)}}^{\mathrm{sat}}\left(T_{\mathrm{a}}\right)=1013.25\cdot\frac{RH}{100}\cdot e^{\left(14.4114-5328/T_{\mathrm{a}}\right)} \tag{95}$$

$$\tau_{\mathrm{atm}}=2.02\left(\frac{RH}{100}\cdot P_{\mathrm{H_2O(v)}}^{\mathrm{sat}}\left(T_{\mathrm{a}}\right)\cdot \mathcal{L}\right)^{-0.09} \tag{96}$$

6.5.3. Modeling of the radiation fields

To determine the thermal flux of a fire plume it is necessary to apply the march of Eqs. (85), (75) and (94).

$$\dot{q}''=\left\langle E_{\mathrm{eff}}\right\rangle \mathcal{F}_{1\to 2}^{\mathrm{view}}\ \tau_{\mathrm{atm}} \tag{85}$$

Step 1: Calculate the time average surface emissive power of the visible fire plume along its length (height), using the Eq. (75)

$$\frac{\bar{E}=SEP\equiv\bar{E}\equiv\left\langle E_{\mathrm{eff}}\right\rangle}{E_0}=\psi+\left[\frac{1+\mathfrak{n}\ e^{-\left(A_{\mathscr{L}}\,C_{\mathrm{s}}\,L_{\mathrm{beam}}\right)}}{1+\mathfrak{n}}\right]\left(1-\psi\right) \tag{75}$$

Step 2: Determine $\mathcal{F}_{1\to 2,\max}^{\mathrm{view}}$, according to Eq. (94)

$$\mathcal{F}_{1\to 2,\max}^{\mathrm{view}}=\sqrt{\left(\mathcal{F}_{1\to 2,\ \mathrm{horz}}^{\mathrm{view}}\right)^2+\left(\mathcal{F}_{1\to 2,\ \mathrm{vert}}^{\mathrm{view}}\right)^2} \tag{94}$$

Step 3: Calculate τ_{a} using the Eq. (96)

$$\tau_{\mathrm{atm}}=2.02\left(\frac{RH}{100}\cdot P_{\mathrm{H_2O(v)}}^{\mathrm{sat}}\left(T_{\mathrm{a}}\right)\cdot \mathcal{L}\right)^{-0.09} \tag{96}$$

7. Effects of thermal radiation on individuals and material resources

7.1. Fundaments and discussions about the stochastic 'probit' functions

The accidents (spill, fire, etc.) are random events, and they use probability distribution functions to describe their occurrences. The effects are deterministic events; in turn, they use deterministic physical models to quantify their impacts. The spills, fires, explosions, etc., generate effects on the surrounding resources, provoking impacts due to mas, heat and momentum transfers. Often, they take place simultaneously, and with some extension, one prevailing over others. These resources respond to such transfers with physical effects, such as poisonings, burns, lung ruptures, etc.

The prediction of the effects on individuals considers a predetermined pattern, e.g., occurrence of death, due to the exposition to a given toxic concentration. Discrete functions usually do not determine the consequences, such as constant peak loads generating discrete effects. Instead, the predictions uses distribution probability functions, given the random nature of the events. We anticipate here the use of the Equations (101) to (104) for this purpose.

A method to assess the consequences of a given release is the dose-response model. It uses 'probit' (probability unit) functions to linearize the response. For single exposures, this method is a stochastic transform that converts the curve of the dose-response into a straight line. This generic method evaluates consequences and couples probit functions with dose loads to linearize the response (Finney, 1971). It attends by the name of ‘Probit analyses’, published between 1940 and 1950 (ioMosaic, 2007; AIChE, 2000; Finney, 1971).

TNO (1992) and Einsenberg et al. (1975) developed a model to calculate the thermal effects. They correlated damage load (dose, or a function of energy released by a fire and the duration of exposure), response (mass per unit time), and the percentage of individuals affected with a specific extent (‘response’).

Given the wide variability of responses from individual to individual, the best model is the normal distribution. In addition, the logarithm function is the best curve to describe the average behavior of the individuals affected by the dose (ABS, 2004; AIChE, 2000; TNO, 1992). It has a mean response and a standard deviation. As a result, there is variability of responses from individual to individual. Thus, in a given sample, a broad spectrum of responses may occur for a given constant exposure.

For convenience, it is useful and usual to plot in a graph a curve of the logarithm of the dose versus the cumulative average response for each dose. "Dose" is the amount of thermal radiation incident on the surface area of the skin per unit of time, for example. ‘Response’ is number (probit) associated to only one percentage defined by a stochastic transform. This format provides a straight line in the middle of the dose range. The logarithm follows this pattern for many organisms, but there are individuals who can tolerate higher levels of causal variable while others that are sensitive to it.

The area under the curve represents the percentage of individuals affected in the interval by a given response. A response with one standard deviation means that 68% of individuals are affected, and with two standard deviations means that 95.5% are affected. In the infinite, the curve will tend to three standard deviations, having the area under the curve equal to 1 (100%).

It is possible to determine the correlation between the doses using ‘probit functions’. For exposures to radiation fields in open areas, the dose-response curve $\left[\mathcal{D}\text{ - }R(\%)\right]$ and the probit variable correlates to each other through the probabilities. They use a transform of a stochastic distribution as defined by the Eq. (97) (ABS, 2004; TNO, 1992). This equation reflects a generalized correlation, time dependent, for a variable that may have a stochastic consequence. A normal Gaussian distribution can define them.

$$\text{Response } = R(\%) = \frac{1}{\sqrt{2\pi}}\int_{-\infty}^{Pr-5} \exp\left(-\frac{u^2}{2}\right)du = \frac{1}{2}+\frac{1}{2}\operatorname{erf}\left(\frac{Pr-5}{\sqrt{2}}\right) \tag{97}$$

Since Eisenberg et al. (1975), the scientific community has been using this method to evaluate toxic effects. They use a statistical correlation between the damage load and the percentage of people affected to a certain extension. The probit variable is normally distributed, and it has an average value of 5 and a standard deviation 1. Another alternative format of Eq. (97) is the Eq. (98), considering the error function, erf, (ABS, 2004). The calculation of the mortality response (percent fatality) follows this equation:

$$R(\%)=50\left[1+\frac{Pr-5}{|Pr-5|}\operatorname{erf}\left(\frac{|Pr-5|}{\sqrt{2}}\right)\right] \tag{98}$$

Figure 14 presents the correlation between $ln\mathcal{D}$ and the response $R(\%)$. The response percentage (%) is read on the ‘S-curve’ and the probit numbers on the straight line. Table 3 is the equivalent to the ‘S-curve’ and straight line.

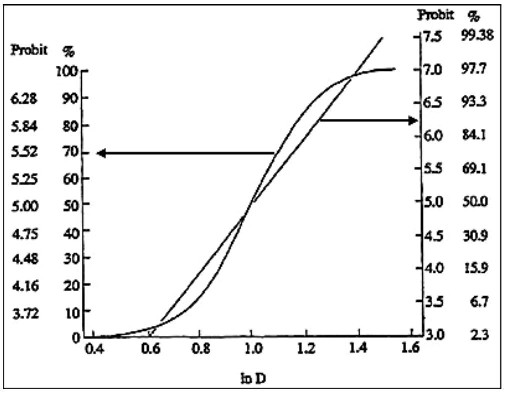

Fig. 14 – Effect of the probit transform.
Adapted from TNO (1992)

%	0	1	2	3	4	5	6	7	8	9
0	-	2.67	2.95	3.12	3.25	3.36	3.45	3.52	3.59	3.66
10	3.72	3.77	3.82	3.87	3.92	3.96	4.01	4.05	4.08	4.12
20	4.16	4.19	4.23	4.26	4.29	4.33	4.36	4.39	4.42	4.45
30	4.48	4.50	4.53	4.56	4.59	4.61	4.64	4.67	4.69	4.72
40	4.75	4.77	4.80	4.82	4.85	4.87	4.90	4.92	4.95	4.97
50	5.00	5.03	5.05	5.08	5.10	5.13	5.15	5.18	5.20	5.23
60	5.25	5.28	5.31	5.33	5.36	5.39	5.41	5.44	5.47	5.50
70	5.52	5.55	5.58	5.61	5.64	5.67	5.71	5.74	5.77	5.81
80	5.84	5.88	5.92	5.95	5.99	6.04	6.08	6.13	6.18	6.23
90	6.28	6.34	6.41	6.48	6.55	6.64	6.75	6.88	7.05	7.33
-	0.0	0.1	0.2	0.3	0.4	0.5	0.6	0.7	0.8	0.9
99	7.33	7.37	7.41	7.46	7.51	7.58	7.65	7.75	7.88	8.09

Table 3 – Relationship between percentages and probits
Adapted from TNO (1992)

On the first column on the left side of the Table 3, the percentage varies from 0 to 90, and on the first line, it varies from 0 to 9, covering therefore the interval from 0 to 99%, with limit probit numbers of, respectively, 0 and 7.33.

After 99%, it is possible to reach 99.9% using probit numbers from the second to the last line, in the interval 0.0 to 0.9. Therefore, for 99.0% (99 + 0.0) the probit number is 7.33 (same as above); for 99.2% (99 + 0.2) the probit is 7.41, and for 99.9% (99 + 0.9) the maximum probit is 8.09. Below 1%, the probit numbers are not applied. A singularity occurs, when the logarithm of the dose reaches 1, resulting in a probability of 50 % with a probit 5. For practical interpolation purposes, one can use the Table 3 to convert percent responses into probits, or vice versa, with reasonable approximation. It is an 'alternative 'solution' for the analytic solution of the Eqs. (97) and (98).

The stochastic transforms of Eqs. (97) and (98) are linearized into the canonic Eqs. (99) and (100), respectively, for exposures to toxic concentration $\mathcal{C}$ and thermal radiation flux $\dot{q}''$ during an interval of exposure time of t_{exp} as follows. The probit functions Pr for fatality responses for both of them are, respectively:

$$Pr = \kappa_1 + \kappa_2 \ln \mathcal{D} = \kappa_1 + \kappa_2 \ln \underbrace{\left[\int_0^{t_{\text{exp}}} \mathcal{C}^{\mathcal{N}} dt \right]}_{\substack{\text{Reynolds time average} \\ \text{of the received dose} \\ = \mathcal{D}_t}} \tag{99}$$

$$Pr = \kappa_1 + \kappa_2 \ln \mathcal{D} = \kappa_1 + \kappa_2 \ln \underbrace{\left[t_{\text{exp}} \cdot \left(\dot{q}'' \right)^{4/3} \right]}_{\substack{\text{Total average dose of radiation} \\ = \mathcal{D}_t}} \tag{100}$$

where κ_1 and κ_2 are the probit parameters established from experimental measurements and/or evaluated from scientific literature.

7.2. Stochastic probit equations

Until now the models presented, correlate the effects of radiant energy striking on vulnerable resources of the surroundings. The subsequent step is to determine its extent on these resources. This section provides a summary of data and methods to estimate the effects on individuals and structures resulting from exposure to thermal radiation. Damage to the environment can be more complex to assess since it may involve impacts on flora and fauna, soil contamination among others. This kind of modeling is not within the scope of this work.

Injuries depend on the heat flux and exposure time. To define the maximum acceptable heat flux and exposure time, one should consider at least three parameters: intensity of thermal radiation fluxes, review data from accidents and catastrophic fires (e.g., Mexico City 1984); results of experiments with guinea pigs in laboratory and burning profiles observed in animals victimized by forest fires. These data allowed the tab of radiation levels and exposure times for various effects. Thus, it was possible to establish the modeling of the 'probability units' (probit) to estimate the likelihood of several effects typically based on the response to the determined thermal loading doses.

The product of the power of incident thermal flux times the effective time to find safe shelter (with around 1 kW/m²), otherwise, models doses, which is determined empirically (ABS, 2004; Mannan/Lees, 2005; TNO, 1992). We reproduce here the Equations from (101) to (104) found in the open literature to model probit functions. They calculate the damage caused by thermal radiation (IoMosaic, 2007; Mannan/Lees, 2005; ABS, 2004; TNO, 1992). Notice that they were modified considering the effective exposure time, t_{eff} , in replacement of the exposure time, t_{exp} , as discussed ahead in 7.3 (Exposure duration, reaction and other related times).

According to TNO (1992), we present the equations for first, second degree burns, and lethality with no protection and with protection. The last probit function accounts for clothing protective influence on fatality for humans. It assumes that 20 % of the body area remains unprotected for an average population. As a result, the fatality for protected bodies is about 14 % of the fatality for unprotected bodies. The modelling of the effective exposure time, t_{eff} , uses, for instance the two equations (7) (*) of ioMosaic (2007), as follows:

- First degree burns

$$Pr_{\text{FDB}} = -39.83 + 3.0186 \ln \underbrace{\left[t_{\text{eff}} \cdot \left(\dot{q}'' \right)^{4/3} \right]}_{\substack{\text{Thermal load or Dose} \\ = \mathcal{D}_t}} \tag{101}$$

- Second degree burns

$$Pr_{\mathrm{SDB}} = -43.14 + 3.0186 \ln \underbrace{\left[t_{\mathrm{eff}} \cdot \left(\dot{q}'' \right)^{4/3} \right]}_{\substack{\text{Thermal load or Dose} \\ = \mathcal{D}_{\mathrm{t}}}} \tag{102}$$

- Lethality with no protection

$$Pr_{\mathrm{LTH}}^{\mathrm{NoPrt}} = -36.38 + 2.56 \ln \underbrace{\left[t_{\mathrm{eff}} \cdot \left(\dot{q}'' \right)^{4/3} \right]}_{\substack{\text{Thermal load or Dose} \\ = \mathcal{D}_{\mathrm{t}}}} \tag{103}$$

- Lethality with protection

$$Pr_{\mathrm{LTH}}^{\mathrm{WPrt}} = -37.23 + 2.56 \ln \underbrace{\left[t_{\mathrm{eff}} \cdot \left(\dot{q}'' \right)^{4/3} \right]}_{\substack{\text{Thermal load or Dose} \\ = \mathcal{D}_{\mathrm{t}}}} \tag{104}$$

To illustrate the application of the probit functions, we reproduce on Fig. 15 the curves of thermal radiation fluxes as a function of the exposure time to produce 1% injuries or fatalities. Observe the quasi superimposition of the curves for second degree burn and fatality without clothing, for this percentage.

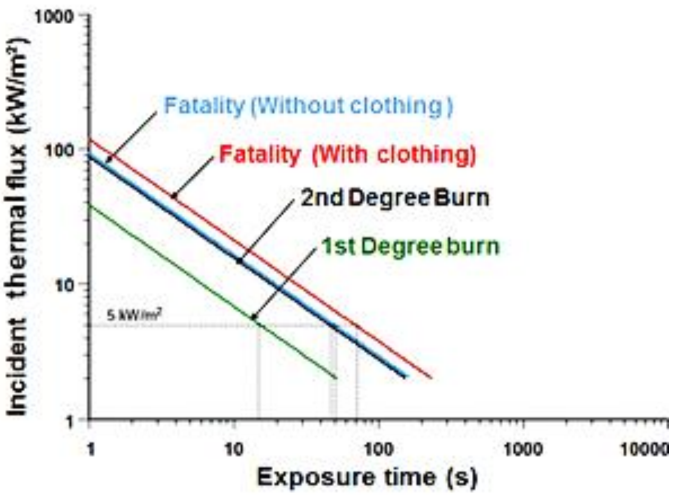

Fig. 15 – Effect of the probit transform. Adapted from ioMosaic (2007)

7.3. Exposure duration, reaction and other related times

Fireballs, BLEVEs, for example, take place in a very short interval, meaning that there is neither enough time to escape nor to look for sheltering. Rausch et al. (1977) recommend 30 seconds for the exposure duration to so-called urban areas. For other remaining areas, the exposure duration is strongly dependent on prevailing circumstances.

This option, however, the users have the option to model. With illustrative examples of that reference, it was shown how strongly the damage extent is strongly dependent on the exposure duration time. In other words, the extent of the damage, i.e., dead or wounded individuals, is fully dependent on this duration, the magnifying effect of which scales up by a factor of 40-50 times.

Heat radiation causes injuries to the people exposed, and the type of injury is determined by the exposure duration. Moreover, the injury extension is strongly dependent of this time, which depends on many incidental circumstances, and one of them is the reaction time, i.e., the time lapse to search for shelter. Thus, it is difficult to define beforehand specific rules/scenarios for these durations, given the randomness of the events. These also depend on escape routes and shelters available, on the composition (elders, children, handicapped, etc.) of the exposed people. Usually, the open literature considers three environmental characteristics are considered: (i) urban areas (buildings), (ii) build-up areas (centers of villages), (iii) open areas (agricultural flat land).

Hymes (1983) analyzing the accident of Los Alfaques (Spain) deduced that an individual would require 5 seconds to react, and subsequently run a distance of 30 m to get away from the fire with an escape speed of 6 m/s. He considered that these figures could be a good evaluation. TNO (1992) also cites that in a LNG Integral study, and in a few other risk analyses, exposure duration of 60 seconds, irrespective of specific circumstances. However, a 30 seconds figure could indicate, as estimation in other studies. According to that methodology, fatal injuries due to heat radiation are still possible to occur to distances larger than 1,000 m.

In the case of Mexico City accident (with LPG), Pietersen (1985) concluded that due to the high building density and the protective possibilities backed up by the distances, fatal injuries due to radiation were still possible for "major damages" outside a radius of 300 m. The exposure duration was significantly lower than 60 seconds were. Thus, providing the available literature, TNO sustains that this duration time focuses "exclusively on engineering judgment".

In risk assessment evaluations, due to the scarcity of available data, it is usual to assume a pessimistic approach. In other words for the exposure duration, the value selected could be longer than the one which can reasonably be expected. In this fashion, values of 30-60 seconds could represent an overestimation figure. However, the calculation of the overall exposure time, one may consider escape possibilities. It is reasonable, in principle, also to consider the radiation decreasing with time.

TNO (1992) simplifies this procedure assuming a pessimistic approach stating that, "the exposure duration will be taken equal to the time required to react (5 seconds) plus the time required to reach a distance at which the radiation intensity is not higher than 1 kW/m²[17])"

Hymens (1983) proposed to use a speed scape of 6 m/s. However, this value seems to be high, if one uses it as an average figure, since TNO (1992) proposes otherwise to use 4 m/s.

TNO suggests that in the case when the exposed group has an average composition (elders, children, handicapped,…), it is possible to consider a different reaction time and a different escape speed, for both positive (following the crowd flux during the escape) and negative (against the flux). However, unless concrete data are available, this one can consider this information merely as approximation.

ioMosaic (2007) citing Cassidy and Pantony (1988) and TNO (1992), presented probit equations (101) to (104) for first/second degree burns and lethality levels, within the infrared spectrum. A part of the total spectrum is indicated in Table 4, recommending, however that this table should not be extrapolated to 1 kW/m².

Table 4 – Relationship between percentages and probits

Thermal load (kW/m²)	**Time for reaction (t_{rct}) (sec)**
22	0.2
18	1.5
11	3.5
8	5.5
5	9.0
2.5	25.0

The influence of escaping from a given location impacted by a thermal flux to a place where the radiations is safer (approx. 1 kW/m²) can also be used for an estimation of injuries and fatalities (Opshoor et al., 1992). In the present model, as conceived by TNO, the concepts of 'effective exposure duration', t_{eff} , and the 'effective exposure duration during the escape', $t_{\mathrm{eff,esc}}$ are developed. One can express the dose of thermal radiation, $\mathcal{D}_{\mathrm{t}}$, according to Eqs. (99) and (100):

$$\mathcal{D}_{\mathrm{t}} = \dot{q}'' \cdot t_{\mathrm{eff}} \tag{105}$$

TNO (1992) recommended considering a tentative exposure time of $t_{\mathrm{exp}} = 20\,\mathrm{s}$. However, this time may vary, depending on the fire location and the population affected by the radiation. To overcome this difficulty, Melhem et al. (2006) suggested substituting the exposure time of Eq. (99) by another parameter, the effective exposure duration, t_{eff} . This could be more realistic to use in probit equations (101)-(104). The influence of the time to leave the fire location to seek for shelter, when the radiation is supposed to be safe (1 kW/m²) can estimate injuries and fatalities from the incident radiation (ioMosaic, 2007; Opschoor et al., 1992).

In accordance with ioMosaic (2007), a realistic value for an individual to react could be assumed as $t_{\mathrm{rct}} = 5\,\mathrm{s}$, so the parameters $\mathcal{L}_1$, u_{esc} and $t_{\mathcal{L}_1}$ can be defined. One can calculate $\mathcal{L}_1$ using numerical iterations, since for a given flux both τ_{atm} and $\mathcal{F}^{\mathrm{view}}_{1\to 2,\mathrm{max}}$ depend on $\mathcal{L}_1$. The present modelling implements this iterative process with successive interpolations, such as of the Newton-Raphson. Therefore, one can write the Eqs. from (101) to (104) considering now the effective exposure time, t_{eff} . The calculation of this time uses the equation (7) (*) of ioMosaic (2007), introducing the reaction time $t_{\mathrm{rct}} = 5\,\mathrm{s}$, $\mathcal{L}_1$ as the distance to 1 kW/m², u_{esc} as the run velocity, and $t_{\mathcal{L}_1}$ as the time to reach 1 kW/m², giving therefore

[17] TNO (1992) cited by ioMosaic (2007), considers: "1 kW/m² as the maximum heat flux the skin can absorb during a long time without feeling pain." This is approximately eequivalent to the solar flux received without protection.

$$t_{\mathrm{eff}} = t_{\mathrm{rct}} + 0.6\frac{\mathcal{L}_1}{u_{\mathrm{esc}}}\left[1-\left(1+\frac{u_{\mathrm{esc}}}{\mathcal{L}_1}t_{\mathcal{L}_1}\right)\right]^{-(5/3)} \tag{106}$$

Similar equation is based otherwise on Eq. (5.2), compiled here as it is from TNO (1992), such that

$$t_{\mathrm{eff}} \cong t_{\mathrm{rct}} + \underbrace{\frac{3}{5}\frac{\mathcal{X}_0}{u_{\mathrm{esc}}}\left\{1-\left[1+\frac{u_{\mathrm{esc}}}{\mathcal{X}_0}\cdot\frac{\mathcal{L}_1-\mathcal{X}_0}{u_{\mathrm{esc}}}\right]^{-(5/3)}\right\}}_{t_{\mathrm{eff,esc}}} = t_{\mathrm{rct}} + t_{\mathrm{eff,esc}} \tag{107}$$

This model allows calculating the influence of the fire extension on the exposure duration. However, for the case of short duration fires, the escape route to be covered becomes shorter, decreasing the radiation dose. Therefore, the possibility of sheltering is not considered, since this effect can be incorporated into the calculation by the selection of a maximum values for t_{eff}, which is dependent on the environment area considered. In some cases, the fire can have a limited duration. This, in turn, also affects the radiation dose received. This effect can be taken into consideration when calculating t_{eff}, by substituting the value of $t_{\mathrm{exp}} = t_{\mathrm{rct}} + t_{\mathrm{esc}}$ in Eq. (98) by the real fire duration, i.e., t_{V} (vaporization time of the pool), providing the latter is shorter than the escape time, t_{esc}.

According to TNO (1992) Annex B Page 54 and presented in Fig 11, an individual located at $\mathcal{L}$ (or $\mathcal{L}_{\mathrm{pathlength}}$) from the edge of the pool fire, will have to run with an escape speed of u_{esc} = 4 m/s up to the point where the thermal radiation predicted by the computer program gives a distance $\mathcal{L}_1$ where the thermal flux is 1 kW/m². Otherwise, $\mathcal{L}_1$ counts from the center of the pool fire, where the thermal flux is equivalent to the solar radiation. The escape distance to be covered is $\mathcal{L}_1 - \mathcal{X}_0$, since the TNO (1992) context considers $\mathcal{X}_0$ as the distance where an individual is located (from the center of the pool fire) when he starts to escape from the pool fire. So one can write

$$t_{\mathrm{esc}} = \left(\mathcal{L}_1 - \mathcal{X}_0\right)/u_{\mathrm{esc}} = \left(\mathcal{L}_1 - \mathcal{X}_0\right)/4 \tag{108}$$

Considering that the reaction time is t_{rct} and the time to escape from the fire with a given radiation intensity is t_{exp}, one can determine the total exposure duration t_{exp}, as follows

$$t_{\mathrm{exp}} = t_{\mathrm{rct}} + t_{\mathrm{esc}} \tag{109}$$

Considering that $t_{\mathrm{rct}} = 5\,\mathrm{s}$ as adopted by TNO (1992), the total dose of thermal radiation is

$$\mathcal{D}_{\mathrm{t}} = \underbrace{\left[\dot{q}''\left(t = t_{\mathrm{rct}}\right)\right]^{4/3}}_{\mathcal{D}_{\mathrm{rct}}} + \underbrace{\int_0^{t_{\mathrm{esc}}}\left[\dot{q}''(t)\right]^{4/3}dt}_{\bar{\mathcal{D}}_{\mathrm{esc}}} \tag{110}$$

$$\mathcal{D}_{\mathrm{t}} = \mathcal{D}_{\mathrm{rct}}\left(\text{reaction time}\right) + \bar{\mathcal{D}}_{\mathrm{esc}}\left(\text{escape time}\right) \tag{111}$$

If Eq. (B.5)(*) of TNO (1992) is considered, then

$$\mathcal{D}_t = \left(\dot{q}''\right)^{4/3} \bullet \underbrace{\left[\!\left[t_{rct} + \underbrace{\frac{3}{5}\frac{\mathcal{X}_0}{u_{esc}}\left\{1-\left[1+\frac{u_{esc}}{\mathcal{X}_0}\left(t_{exp}-t_{rct}\right)\right]^{-(5/3)}\right\}}_{t_{eff,esc}} \right]\!\right]}_{t_{eff}} =$$

$$\left(\dot{q}''\right)^{4/3} \bullet \underbrace{\left[\!\left[t_{rct} + \underbrace{\frac{3}{5}\frac{\mathcal{X}_0}{u_{esc}}\left\{1-\left[1+\frac{u_{esc}}{\mathcal{L}_1}\bullet\frac{\mathcal{L}_1-\mathcal{X}_0}{u_{esc}}\right]^{-(5/3)}\right\}}_{t_{eff,esc}} \right]\!\right]}_{t_{eff}} \tag{112}$$

According to Eq. (109), one can have, alternatively, that $t_{esc} = t_{exp} - t_{rct}$ as considered in the same fashion by Eq. (5.2) of TNO (1992), then one has

$$\mathcal{D}_t = \left(\dot{q}''\right)^{4/3} \bullet \underbrace{\left[\!\left[t_{rct} + \underbrace{\frac{3}{5}\frac{\mathcal{X}_0}{u_{esc}}\left\{1-\left[1+\frac{u_{esc}}{\mathcal{X}_0}t_{esc}\right]^{-(5/3)}\right\}}_{t_{eff,esc}} \right]\!\right]}_{t_{eff}} \tag{113}$$

Therefore, one can use either the Eqs. (112) or (113) solve the Eqs. (101)-(104). In the so-called "urban area", consisting of high density of buildings, one can derive a correlation can be derived for the effective exposure duration, t_{eff} . Taking into account the density of neighbor buildings, one can derive a correlation for the effective exposure escape possibilities, considering otherwise that it is necessary to derive a proper value for the radiation field.

8. Evaluation of exclusion and safety zones and selection of thermal radiation levels

This topic discusses the criteria to set the maximum thermal radiation flux that could be acceptable to strike on the resources around LNG terminals. Pursuant to Esteves et al (2016, 2015) and items 7.1, 7.2 and 7.3, here we present the tools to define siting criteria, exclusion and safety zones. They follow the main international codes, standards, and regulations.

However, it should be emphasized that, based on those references and ABS (2004) and FERC (2004), none of the 'siting criteria' and 'exclusion zones' are applicable to LNG offshore terminals. They are applicable to onshore terminals only.

Yet, for onshore terminals, the criteria and exclusion zones do not apply to potential releases from an LNG carrier moored at an unloading terminal dock. For U.S. LNG terminals, there is generally safety zones defined for both LNG unloading docks and for LNG carriers in transit through port areas.

8.1. Applicable definitions

Exclusion zone

The area around an LNG facility in which operators or government Authority has the legal control of all activities. The Authorities use the CFR codes[18] to delimit these zones. These areas encompass:

- Flammable dispersion zone: The area reached by a cloud at 50% v/v or more of the flammable concentration of Methane obtained with a design spill of LNG. However, it cannot extend beyond the LNG facility property line (NFPA 59A, 2006);
- Impoundment area: Physical provisions to minimize the possibility of an accidental discharge of LNG tanks endanger vicinal properties or important process equipment and structures, or even reaching waterways. Generally, impoundment areas are

[18] U.S. 49 CFR Subparts 193.2057 for thermal radiation and U.S. 49 CFR Subparts 193.2059 for flammable vapor hazards.

- as a containment dike or sump. If designed and constructed properly, the outside wall of a double wall storage tank could be considered an impoundment area (NFPA 59A, 2006);
- Thermal radiation zone: The area potentially impacted by a fire involving a design spill quantity into the impoundment or a dike fire to specific exposure level for various occupancy categories around the facility. For example, the level usually adopted at the facility boundaries is 5 kW/m². The various exposure levels are presented in the item 8.2.1 below (NFPA 59A, 2006);

Safety zone

The area (water, shore or water and shore) to which, for safety or environmental purposes, access is limited to authorized persons, vehicles, or vessels only. It may be stationary and characterized by fixed limits. However, some port authorities may describe it otherwise as an exclusion zone around a vessel in motion (USCG 33 CFR 165.20),

Security zone

The area (land, water, or land and water) allocated by the Navy Authorities during specific times. They must: (i) prevent damage or injury to any ship or waterfront facility, (ii) guarantee the safeguard of ports, harbors, territories, or waters of the U.S.A., (iii) assure the strict observance of the rights and obligations defined on the U.S.A. Codes, such as the USCG 33 CFR 165.30.

8.2. Criteria and exclusion zones specifications

The following standards are applicable:

- European Normalization, EN 1473 - Installation and Equipment for Liquefied Natural Gas - Design of Onshore Installations;
- NFPA 59A-2006 - Standard for the Production, Storage, and Handling of Liquefied Natural Gas;
- U.S. DOT Regulation 49 CFR Part 193 - Liquefied Natural Gas Facilities: Federal Safety Standards;
- Canadian Standard CSAZ276-01 - Liquefied Natural Gas (LNG) — Production, Storage, and Handling.
- Nova Scotia Department of Energy, Code of Practice for Liquefied Natural Gas Facilities.

8.2.1. Selection of the thermal radiation levels

8.2.1.1. Human exposure

Thermal radiation levels should be set for the population exposed to potential events of fire in a terminal. For example, allowable levels of thermal radiation should be defined differently for (i) process plant operators who make use of appropriate clothing, (ii) areas where there is usually no human presence, but to which there may be access, or (iii) sensitive populations (elderly, disabled, for example).

For the purposes of the analysis of an onshore facility, the Code of Federal Regulation 49 CFR 193 and NFPA 59A-2006 specify a level of interest of 5 kW/m². Table 5 presents the expected effects based on industry information. The level of 5 kW/m² is applicable to short-term events such as, for example, fireballs. It is also applicable in the early stages of longer duration events such as pool fires, taking into account that the population potentially exposed has the opportunity and ability to seek quickly protection.

Table 5 – Effects of thermal radiation on humans for a level of 5 kW/m²
Source: Adapted from Esteves et al. (2015) (Table 1), ABS (2004) (Table 2.6), FERC (2004) and FEMA (1990)

Effect/Injury	Exposure time (s) / Data source	
Severe pain	13	Table 2.2 ABS (2004); FEMA (1990)
1st degree burn	20	Table 2.4 (ABS, 2004); Prugh (1994) (5 kW/m² for 20 s, corresponding to a thermal radiation load of 100 s.kJ/m²)
2nd degree burn	30	Table 2.4 ABS (2004); Prugh (1994) (5 kW/m² for 30 s, corresponding to a thermal radiation dose of 150 s.kJ/m²)
	40	Table 2.2 (ABS, 2004); FEMA (1990)
3rd degree burn (1% fatality)	50	Table 2.4 (ABS, 2004); Prugh (1994) (5 kW/m² for 50 s, corresponding to a thermal radiation dose of 250 s.kJ/m²)
72% probability for 1st degree burns	40	Eqs. (101) to (104) above; TNO (1992)

8.2.1.2. Effects of thermal radiation on structures

Similar to the effects of thermal radiation on human beings, its effects on structures also depend on incident heat flux and the exposure time. With structures, effects also depend strongly on the materials used in the construction, for example, steel, concrete, wood. Table 6 shows design and assessment guideline values for the effects of thermal radiation on structures. For large incidents involving LNG spills on water, selection of levels of concern is a complicated issue for the fact that fires can be of short-duration, about 5 minutes for a pool fire involving a fast leak of inventory from a simple membrane cargo tank from a carrier. However, we point out that the mentioned values are merely guidance on damage to structures and they consider long-duration exposures of 30 minutes or even more. Table 6 summarizes the most widely used.

Table 6 – Design and assessment guidance s for the effects of thermal radiation on structures
Source: Adapted from Esteves et al. (2015), ioMosaic (2007), ABS (2004), AIChE (2000) and World Bank (1988)

Thermal radiation intensity limit (kW/m^2)	Limit description/Observed effect
Design Guidance from AIChE (2000)	
37.5	Sufficient to cause damage to process equipment
25.0	The minimum energy required to ignite wood at indefinitely long exposure (nonpiloted)
12.5	The minimum energy required for piloted ignition of wood, and melting of plastic tubing. This value is typically used as a fatality number
9.5	Sufficient to cause pain in 8 seconds and 2nd degree burns in 20 seconds
4.0	Sufficient to cause pain to personnel if unable to reach cover within 20 seconds. However, blistering of skin (second degree burns) is likely; 0% lethality
1.6	Will cause no discomfort for long exposure
Design and assessment guidance from British Standard 5908 (BS 5908:1990)	
37.5	Intensity for damages on process equipment
25	Intensity at which nonpiloted ignition of wood occurs
12.5	Intensity at which piloted ignition of wood occurs
Design and assessment guidance from Mecklemburgh (1985)	
14	Intensity that normal buildings should be designed to withstand
10-12	Intensity at which vegetation ignites
Assessment guidance from DiNenno-NFPA (1982)	
30	Spontaneous ignition of wood
15	Piloted ignition of wood
20	Ignition of No. 2 Fuel Oil in 40 seconds
10	Ignition of No. 2 Fuel Oil in 120 seconds
18-20	Cable insulation degrades
12	Plastic melts
37.5	Equipment damage
9	Equipment damage – conservative value used in flare system design
Design Guidance from Kletz (2005, 1980)	
38	Intensity on storage tanks
12.5	Intensity on wood or plastics
5	Intensity on people performing emergency operations

The data presented above show variations in intensity levels and associated effects. However, the data are relatively consistent and, additionally, for long-duration exposure, some reasonable choices for levels of concern and associated types of damage could be used as follows:

- 38 kW/m^2 - Damage to process equipment and storage tanks;
- 25 kW/m^2 - Ignition of wood without direct flame exposure;
- 12 kW/m^2 - Piloted ignition of wood, melting of plastic material, ignition of vegetation.

These levels refer to general guidelines for fire of any duration; nevertheless, it is necessary care since they will tend to be very conservative for fires of short-duration. For instance, steel structures exposed to a much higher intensities for short-durations without causing any type of damage due to temperatures rising. Thus, as a general recommendation, heat balances calculations are required to assess the intensities and durations that a specific structure can withstand. In order to minimize the need for heat balance calculations, the interest levels above mentioned applies, but a detailed analysis may be required on case-by-case situations, when structures have the potential for exposure to fires of shorter duration.

8.2.2. European LNG standard

The European standard EN 1473 (1997) requires risk analysis to identify potential accidents that can occur, including scenarios of large LNG spills that may result in pool fires. It also specifies limits that must be met for such fires. Tables 7 and 8 reproduce the recommended maximum incident radiation of flux values for radiation emitted from a pool fire (in cases where such levels has not defined yet by existing local authorities' regulations) for areas inside and outside the facility, respectively. The standard also provides guidelines on how to calculate these levels of radiation.

Table 7 – Allowable thermal radiation flux inside the facility boundaries
Source: Adapted from Esteves et al. (2015), ABS (2004) and World Bank (1988). Based on Table 1 of EN 1473 (1997)

Type of location inside facility boundary	Maximum level of thermal radiation (kW/m^2)
Concrete outer surface of adjacent storage tanks: Unprotected (See Notes 1 and 3) or behind thermal protection (See Note 2)	32
Metal outer surface of adjacent storage tanks: Unprotected (See Note 3) or behind thermal protection	15
The outer surfaces adjacent pressure storage vessels and process facilities	15
Control room, maintenance workshops, laboratories, where houses, etc.	8
Administrative buildings	5

Note (1): for pre-stressed concrete tanks, an approved type of analysis may determine maximum radiation fluxes.
Note (2): Such facilities can be protected by means of water sprays, fireproofing, radiation screens, or similar systems.
Note (3): Protection must be provided by spacing alone.

Table 8 – Allowable thermal radiation flux outside the facility boundaries
Source: Adapted from Esteves et al. (2015), ABS (2004) and World Bank (1988). Based on Table 2 of EN 1473 (1997). Excludes solar radiation

Type of location outside the facility boundary	Maximum level of thermal radiation (kW/m^2)
Remote area (See Note 1)	13
Urban area	5
Critical area (Se Note 2)	1.5

Note (1): Area only infrequently occupied by small numbers of persons (for example, moorland, farmland and desert)
Note (2): This is either (i) an unshielded area of critical importance where people without protective clothing can be required at all times, including during emergencies or (2) a place difficult or dangerous to evacuate at short notice (for example, sports stadium, playground, outdoor theater).

8.3. Siting criteria and exclusion zones as per U.S.A. standards and regulations

According to Esteves et al. (2015), the USA Federal Regulation Codes for industrial safety require LNG terminals surrounded by "exclusion zones". These zones are necessary to protect neighboring communities in the event of a pool fire or a flammable vapor cloud (according to U.S. 49 CFR 192.2057 and 192.2059 subparts) resulting from an LNG spill from an onshore equipment. For FERC site approval, the owner of the facility or a government agency must to exercise "legal control" of activities within those zones. FERC does not require, however, exclusion zones should established for spills from a carrier ship LNG moored at the facility dock or in transit to reach the dock.

The USA, Canada and Nova Scotia adopt some standards and requirements. Notwithstanding, they will not be discussed in detail as part of this scope. The following are some highlights from those:

- NFPA 59A-2006 Siting Requirements: This Standard does not use the term “exclusion zone”. However, it provides criteria for siting a facility based on both thermal radiation hazards and flammable vapor dispersion hazards, specifying the concepts of “Design spill”, “Thermal radiation siting limits”, and “Flammable vapor siting limits”;
- US DOT 49 CFR 193 Exclusion Zone Requirements: This Regulation requires “exclusion zones” based on NFPA 59A requirements. It considers some minor changes, fundamentally related to specific approved analysis assumption and methodologies. The size of the exclusion zone must be calculated in accordance with 49 CFR Subparts 193.2057 when applied to thermal radiation and 193.2059 when concerning to flammable vapor hazards;
- U.S. Coast Guard Safety and Security Zones: The USCG 33 CFR 165.30,29 typically established “safety” and “security” zones for marine LNG facilities and operations as discussed above in the item 8.1 (Applicable definitions) above:

8.4. Canadian Standard Z276-01

The Canadian standard CSA Z276-01 defines the sitting criteria in a similar way as the NFPA 59A 206 does. It uses the same definitions for design and impounding areas, as well as the thermal radiation flux criteria for specific locations. Despite of having similar criteria of analysis, it does not state specific siting criteria when compared to the equivalent U.S. Codes. Regarding methods of analysis, it is more flexible than the equivalent U.S. requirements.

8.5. Nova Scotia Department of Energy LNG Code of Practice

The Code of Practice for Liquefied Natural Gas Facilities (2005) of the Nova Scotia Department of Energy, is more complex and have more restrictions than the Canadian Standard CSA Z276-01 has. For instance, it includes siting requirements from the API and AIChE/CCPS, in addition to what is detailed and implemented in the Canadian Standard Z276-01 requirements. Depending on the project location and type of project, both of them are equally used.

9. Pool spreading and combustion - Results and discussions

9.1. Development of the modelling for pools pill/spreading, pool fire, thermal radiation fields, vulnerability areas as a tool to aid the definition of exclusion zones around LNG facilities

The model calculates 'directly' the variables of interest at a given distance (path length), that is, the heat flux incident on a target, as well as its vulnerabilities in terms of first, second and third degree burns (lethality) for human exposures. One must compare these values of Tables 5 or 6 with reference tools, in order to check if the values calculated are acceptable by the references requirements. Similarly, Then also use Tables 6, 7 and 8 as guidance for the effects of thermal radiation on structures. Once these guidance values matches, subsequent calculations can provide the other distances that fulfill or are lower than the maximum allowed levels for the incident thermal radiation.

In the present work, we also investigated the possible calculation of the variables of interest in a 'reverse' format. Once setting the maximum percentage of vulnerability, for instance, using those from the Authorities, the model can recalculate the respective thermal load (dose). In this case, it implies considering both thermal flux and effective time to escape for shelters. In other words, the probit numbers and their associated percentage of damage caused on the surrounding resources. Again, one should compare these new figures with Tables 5 to 8, giving thus new subsides for safety management countermeasures.

In this process, we managed two variables: (i) the thermal flux emitted by the fire column, $\dot{q}''$ incident at a given distance and (ii) the effective time exposure, t_{eff} . One can reduce the first, for example, based on the most credible scenario, increasing the distance (exclusion zone) by moving the vulnerable resource far away, from the probable location of the fire column (for example, the moor where the carrier is anchored). To reduce the second, one can provide more (or faster to reach) adequate shelters near (or in) the terminal location.

However, this inverse process is not a problem without solution. To speed up of this inverse process, other approaches, adequate calculation march/methodologies, mathematical and computational tools and formulations are possibilities to treat the problem properly. As a preliminary screening method, 'trial-and-error' solutions leveraged by interactive algorithms can achieve the solution introducing tentative path lengths in the transmissivity equations. When the thermal flux striking on the surroundings resources matches the values of incident fluxes prescribed on the industrial standards, this distance is a potential solution, to be a guidance value for terminals siting. However, at the present stage of this research, we have not implemented this approach yet in this report.

9.2. Input data

9.2.1. Pool spreading and vaporization

$CVC =$ 125,000 m³ (Fay, 2003); NT $=$ 5 (Fay, 2003); DR $=$ 11.85 m; h_{o} $=$ 13 m (SNL, 2008); $\mathfrak{B}$ $=$ 2.31 (Fay, 2003); ρ_{w} $=$ 1,025 kg/m³ (ABS, 2004); ρ_{l} $=$ 422.5 kg/m³ (ABS, 2004; Esteves, 2010); ρ_{v} $=$ 1.751 kg/m³ (ABS, 2004, page C-3); ρ_{a} @ 300 K (kg/m³) $=$ 1.178 kg/m³; $\langle \dot{y} \rangle$ $=$ 7E(-4) m/s (FERC, 2004); A_{h} $=$ 0.78 m² $(D_{\mathrm{h}} = 1\mathrm{m})$; A_{h} $=$ 19.6 m² $(D_{\mathrm{h}} = 5\ \mathrm{m})$ (FERC, 2004).

9.2.2. Pool combustion and Transmissivity of the local atmosphere

T_{a} $=$ 300 K (ABS, 2004); P_{a} $=$ 101.325 kPa (ABS, 2004); $c_{\mathrm{P_a}}$ $=$ 1.00 kJ/kg.K, RH $=$ 70% (FERC, 2004; ABS, 2004) (https://www.ohio.edu/mechanical/thermo/property_tables/air/air_Cp_Cv.html (Access 5Jun2016); $E^{\max}$ $=$ 325 kW/m² (Raj, 2007a,b); $\bar{E} =$ 265 kW/m² (FERC, ABS, 2004); $A_{\mathscr{L}}$ $=$ 130 m²/kg (TMS, 2006); L_{beam} $=$ 13.8 m Raj (2007a,b); $\mathfrak{R}$ $=$ 17.1674 for CH_4 (Esteves, 2010, Table 6.1); η $=$ 0.1454 (Esteves, 2010, page 218); $\Delta H_{\mathbb{C}_{\mathrm{L}}}$ $=$ 50,020 kJ/kg (Raj, 2007a,b; Esteves, 2010,Table 6.1); $\mathfrak{n}$ $=$ 3 (Raj, 2007a,b); $U_{\mathrm{wind,10}}$ $=$ 8.941m/s – (ABS, 2004, Page 34).

9.3. Results, comparisons with literature and discussions

9.3.1. Geometry of the semicircular pool spreading

The Figure 16 presents the simulations results about the semicircular pools around the tear of a stricken carrier's hull. It compares the maximum pool areas spilled onto the sea and the respective vaporization time. The carriers have capacities of 125,000 m³ (Fay, 2003) and 265,000 m³ (SNL, 2008, 2004). The pools vaporizing velocities are 0.00021 m/s and 0.0011 m/s.

The A_{m} vs. A_{h} curves present two singularities with prominent (enlarged sizes) points in the figure: (I) light gray color for the 'critical' value of the parameter Υ , where the flow transit from the regime 'gravity-inertia' to 'gravity-viscous'. From this point forward, the concavity of the A_{m} curve inverts upside down. Going one-step further, the area continues to increase until it reaches the (ii) dark grey point, where the pool reaches its ‘maximum’ value. Following, the pool continues to spread, but ‘shrinking’ asymptotically with smaller values, until it reaches the higher limit of A_h = 100 m² of the tear value.

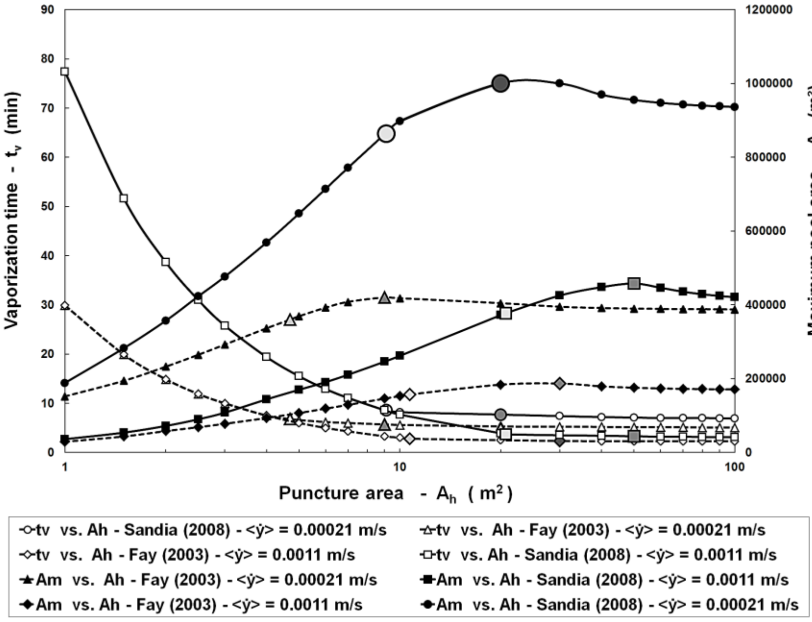

Fig. 16 – Maximum pool areas and vaporization times vs. puncture areas. Source: Esteves and Parise (2013a,b)

Depending on the local atmospheric conditions, the volume of the carrier tanks, extension of the tear perpetrated on the carrier hull, and the magnitude of the vaporization velocity, this matter may represent a potential challenge for the Authorities involved with the licensing and siting LNG terminals. When dealing with carriers of huge capacities, these distances are equivalent to the length of a carrier from bow to stern.

The t_v curves present only one concavity in the upside direction as the puncture area rises up to 100 m², due to the vaporization time decreasing constantly with the increase of the tear area.

The Figure 16 compares some results of our investigation. We considered the vaporizing velocities of 0.00021 m/s for the LNG disgorged onto the sea, spilled from a carrier cargo tank. We found that carriers with 265,000 m³ of capacity (Sandia geometry), form maximum pools of 1,000,525 m² on the sea with radius of 564 m. If the capacity of the carrier is 125,000 m³ (Fay Geometry) and the pool vaporizes with the same velocity, than the maximum pool formed will have 420,243 m² with radius of 366 m.

On the other hand, if the vaporization velocity rises to 0.0011 m/s the Sandia geometry provides maximum pools with 457,942 m² with the radius of 382 m, and the Fay geometry gives maximum pools of 186,942 m² with radius of 245 m.

When one compares flows through tears in the ship's hulls, smaller tears ("slow" discharge of LNG onto the sea) are less dependent on the size of the carriers’ geometries, but rather on the vaporization rate. That is, the pool formations are governed by the flow (fluid mechanics governs the phenomenon) in detriment of the vaporization (mass transfer).

On the other hand, with larger tears (100 m²), at the slower vaporization velocity (0.00021 m/s), semicircular pools reach 387,945 m² and 936,433 m², respectively, for the Fay and SNL geometries. If one considers the fastest speed (0.0011 m/s), Fay geometry provides pools with 170,797 m², and SNL geometry renders pools with 420,749 m², disgorging the fluid onto the sea, as if the tear were an "open" channel. In other words, vaporization (thermodynamics prevails the phenomenon) governs the pools formation in detriment of the spreading.

When one compares the vaporization time of both geometries with maximum speed and tears of 100 m², all vaporization times converge to a maximum of 5 min, while with tears of 1 m², these times reach 30 min with Fay geometry and 77 min with SNL geometry. Time of about 2-fold geometry to another, is compatible with twice the volume spilled onto the sea when one compares both geometries. It follows that the mathematical model used here, plausibly describes the physical phenomenon.

9.3.2. Fire column geometry varying with circular pool diameter

The dimensionless ratio $L_V/D_{p_{ci}}$ defines the geometry of the thermal plume. The Figure 17 shows predictions obtained for the geometry behavior of a vertical thermal plume without tilt, flame drag and extended diameter, caused by wind action. Untilted flames tend to provide taller flame lengths, consequently, longer downwind hazard distances and more conservative hazard predictions. If the wind action is considered, one can expect that lower L_v/D_{pci} ratios may occur.

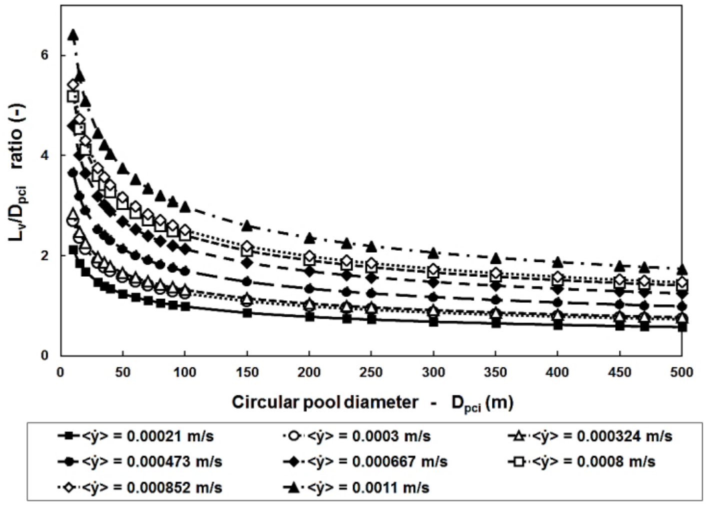

Fig. 17 – Thermal plume geometry vs. circular pool diameter. Source: Esteves e Parise (2013a,b)

Several correlations of fires varying with the diameter are depicted in Fig. 18 (Esteves and Parise, 2013; SNL, 2011).

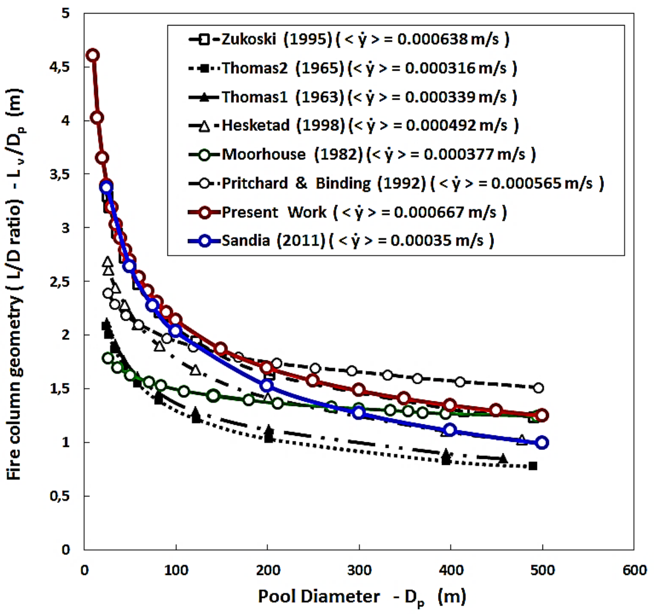

Fig. 18 – Comparison of some geometry correlations. Source: Esteves e Parise (2013a,b)

We converted the semicircular pools into circular using the Eq. (33), covering the range of 10 to 500 m, consistent with the sizes of the vessels currently in use in the ocean transportation of LNG. We assume that constant temperature and concentration of gases characterizes the flame regardless of the size of the column, and the concentration of soot inside it (SNL, 2008).

We suppose that the variation of radiative properties and the rate of the turbulent mixture are constant, due to the pool combustion mechanisms or those induced by the intake of atmospheric air in its side. We use average coefficients to describe local behaviors, because of the complexity problem that takes place on a microscopic scale. However, we describe it using global experimental correlations, instead of exact equations (SNL, 2008).

We predicted all curves using, where applicable, the Eqs. (55) and (57), following the same geometry pattern of Figs. 7 and 17. The geometry ratio behavior observed for the eight vaporization velocities follow the same pattern.

The vaporization velocities vary in a narrower interval, $0.000316 \le \langle \dot{y} \rangle \le 0.000667$ m/s, in order to compare the results of the present work with those indicated in the figure. Some conclusions are noteworthy: (i) the highest ratio occur with fire columns of smaller diameters, showing that the combustion Froude number [inertia forces (upwards) vs. gravitational forces (downwards)] indicates that the inertia outweighs gravity due to less formation of toroid vortices of combustion products.

These whirls/vortexes make the draft of combustion products off the flame core difficult. This means: (i) higher flames are lighter, with more efficient combustion, less smoke and faster draft; (ii) as the diameter increases, the Froude number decreases, the fire column gets ‘thicker' due to the smoke content, tending to lower the height of the fire column. At 500 m diameter, the plume height is almost equal to the diameter (L_v/D_{pci} approximates to 1); (iii) approximately at 10 m diameter, the plumes have

L_V/D_{pci} ratio ranging from 2 to 6, where the vaporization velocity governs this 'jump', while with a diameter of 500 m, this 'heel' varies between 1 and 2; (iv) with a velocity approximately 5 times higher, the plume will be about 6-fold higher, which is plausible, given that the balance is governed by Froude number. It shows the same exponential decay as the pool diameter increases.

As an expected trend, the higher the burning velocity, the higher the geometric L_V/D_{pci} ratio, explained by the rise of the combustion Froude number (faster burning with smaller diameters), even with an exponential power of 2/3 (= 0.6667 of Raj's model) or 0.539 (SNL's model) (see item 9.3.3 ahead).

SNL predictions modelled by Eq. (57) and the predictions of this work, given by Eq. (55), followed the same pattern. For small diameters (25 m) the Lv/Dpci ratio, both were almost equal: SNL with 3.37 and this work with 3.39.

As the diameters increased, the difference between values became bigger (as expected) due to mainly the velocities difference [this work with 0.00067 m/s and SNL (2001) with 0.00035 m/s].

For 200 m, SNL found 1.52, and this work 1.69; for 500 m, SNL modelled 0.99, and this work 1.25 (but with 0.000667 m/s), compared to 1.51 of Pritchard & Binding with 0.000565 m/s.

We assumed the Moorhouse and SNL correlations to match the diameters span from 200 to 400 m; at 300 m, Moorhouse set 1.31 and SNL, 1.27. Before this turning point, SNL gives higher ratios; after that, the situation inverts, reaching a ratio of Moorhouse (1.25)/SNL (0.99) of approximately 1.25. We included the Thomas' correlations to illustrate the context of the Thomas' experiments and researches since 1963-1965.

9.3.3. Fire column geometry varying with Froude combustion number

This behavior presented in Fig. 19, is a variation of Fig. 17, where D_{pci} was replaced by Fr_{C}. For pools burned with turbulent combustion of non-premixed flames, where gravity plays a fundamental role $(Fr_{\mathbb{C}} \ll 1)$ and the mixture of air is a function of gravitational forces, the plume geometry ratio is very sensitive to Froude number (Raj, 2007a,b).

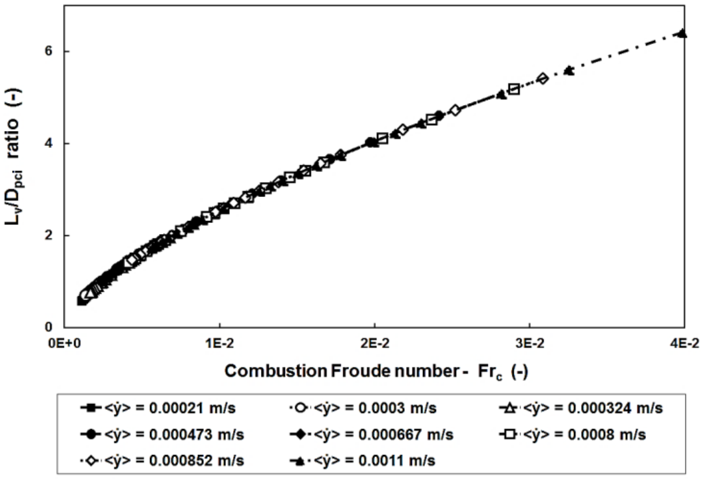

Fig. 19. Fire column geometry vs. Combustion Froude number

The exponential behavior given by the 2/3 power follows the same pattern for the eight vaporization velocities and is consistent with Eqs. (51) and (52). The highest geometry ratio of 6.4171 occurs with the lowest diameter of 10 m and highest velocity of 0.0011 m/s (and greater $\dot{m}''_V$), i.e., burning the pool very rapidly. The lowest ratio of 0.5775 occurs with the largest diameter of 500 m and at the lowest speed of 0.00021 m/s, i.e. burning the pool slowly. Different velocities imply in different intervals, depending on the vaporization velocity adopted in each prediction. Nevertheless, despite of the differences, all the curves present the same profile by virtue of Eq. (55) or (57), reason for the curves superposition. Diameters varying between 500 m and 10 m, give intervals of $0.00107 \le Fr_{\mathbb{C}} \le 0.033985$ and this corresponds to $0.057752 \le L_{\mathbb{V}}/D_{p_{ci}} \le 6.41707$.

Turbulent diffusion flames of non-premixed combustion with $(Fr_{\mathbb{C}} \ll 1)$, is such that as the diameter increases, it causes difficulties for the lateral air entry into the flame core, and this affects the burning efficiency. It occurs because of the presence of more smoke, which is governed by the gravitational forces, lowering the Froude number and decreasing the inertia with less efficient combustion.

Consequently, $L_{\mathbb{V}}/D_{p_{ci}}$ depends much on $Fr_{\mathbb{C}}$ and this trend makes the plume produce more and more smoke reducing the surface emissive power of the fire column. Larger diameters produce more smoke, forming less dangerous thermal plumes. Thus, instead of flame to be light in most of its extension, converting into light the chemical energy content of the fuel, on the contrary, it opens 'intermittent windows of light', due to the presence of smoke.

9.3.4. Fire column geometry varying with combustion parameters

A sensitivity analysis was carried out to compare predictions, is presented in Tables 9 and 10, using models from literature and from the present work. The main parameters considered were $D_{\mathrm{p_{ci}}}$, $\langle D_{\mathrm{p_{ci}}} \rangle$, t_{v} and $\langle t_{\mathrm{v}} \rangle$ obtained from other reviews (SNL 2008, 2004; Otterman, 1975; Johnson & Cornwell, 2007; FERC, 2004; ABS, 2004; Qiao et al., 2006; Hissong, 2007).

An average value of each parameter from the reference works was determined and compared with the correspondent values found using the present model. Results obtained for $D_{\mathrm{p_{ci}}}$ with Fay's (2003) model differ, to a certain extent, from other results presented in Tables 9 and 10.

Such differences could be partly explained by the distinct flow models that have been adopted elsewhere (Esteves and Parise, 2013a,b; Fay, 2003; Quest (2001, 2003), SNL, 2004; Otterman, 1975; FERC, 2004; ABS, 2004; Qiao et al., 2006; Schneider, 1978; TNO/Van den Bosch, 2005; SNL, 2008). The results considered the same approach of Figs. (16) and (17). Nevertheless, Fay's (2003) model proved to be robust, providing consistent results for the range of today's most common membrane LNG carriers.

This model takes into account all relevant phenomena, including cryogenic spill and pool spreading, as well as vaporization of the maximum area onto the sea.

Results indicate that the model is accurate enough to fit industry needs, although a close agreement between works is still a distant objective. Due to the limitations and scarcity of field tests data, a number of issues on mechanisms that are controversial still remain (Lehr, 20007).

Table 11 compares predicted values of $L_{\mathrm{v}}/D_{\mathrm{pci}}$ from the present work and other models (Thomas, 1965; Pritchard, Binding, 1992; Moorhouse, Pritchard, 1982; Zukoski, 1995; Steward, 1970; Heskestad, 1998), to experimental results from China Lake (tests # 1 and 4), Maplin Sands and Montoir (test # 2) compiled from (SNL, 2008; Hissong, 2007). Good predictability is shown with deviations of, +7.1%, +3.6%, +16.3% and -13.6%, respectively, as related by Esteves and Parise (2013a,b).

Capital letters refers to (A) Pritchard and Binding (1992), (B) Moorhouse and Pritchard (1982), (C) Thomas (1965), (D) Zukoski (1995), (E) Steward (1970), and (F) Heskestad (2002,1998,1983), we considered the vaporization velocities $\langle \dot{y} \rangle$ to calculate the $L_{\mathrm{v}}/D_{\mathrm{pci}}$ ratio for each one of the columns, respectively as: (A) 0.000565 m/s; (B) 0.000377 m/s; (C) 0.000316 m/s; (D) 0.000638 m/s; (E) inferred; (F) 0.000492 m/s and (G) (present work) 000667 m/s. We also considered the scattering of the $L_{\mathrm{v}}/D_{\mathrm{pci}}$ presented in the references from (A) to (F), varying in the interval considered of $1.5 \leq L_{\mathrm{v}}/D_{\mathrm{pci}} \leq 4.7$, the results predicted in the present work using the model of TMS (2006) and Raj (2007c), varied in a narrower span, $1.9 \leq L_{\mathrm{v}}/D_{\mathrm{pci}} \leq 3.0$. In other words, the modelling of the present report led to more convergent results.

Table 9

Comparison with other models of literature for near shore operations. D_h = 1 m, one cargo tank breached. Source: Esteves and Parise (2013)

Results found in the literature and simulations made in the of the present work using Fay (2003) model with Eqs. (20) and (21)									
$V_0 = 12{,}500\text{m}^3$ $D_h = 1$ m $A_h \approx 0.8$ m^2									
Description	**Data from Johnson and Cornwell (2007)**	**Data from Hissong (2007)[1]**	**Data from Qiao et al. (2006)**	**This work with input data from Otterman (1975) [2]**	**Data from FERC (2004)**	**Data from ABS (2004)**	**This work Input data from FERC (2004)**	**This work Input data from ABS (2004)**	**Data from SNL (2008, 2004) [3]**
Vaporization velocity, $\langle \dot{y} \rangle$ (m/s)	0.0007	0.0003 [4]	0.0004 [5]	NA	0.0007	0.0007	0.0007 [6]	0,0007 [7]	0.0003
Thermal flux emitted by the pool fire, q'' (kW/m^2)	143	65 [8]	86 [9]	NA	265	265	151 [10]	151 [10]	220
Release mass flow rate from the cargo tank, $\dot{m}_d''$ (kg/s)	2,300 [11]	1,000 [11]	1,700 [12]	app. 2,300	1,700[11]	2,600 [11]	1,700 [11]	2,600 [11]	NA
Total spill duration, t_d (min)	51	1.5 [13]	app. 50 [14]	30	51	33	27	27	NA
Circular pool diameter, D_{Pci} (m)	140	108	180 [15]	124	141 [16]	200	213 [16]	213 [16]	148
Average circular pool diameter, $\langle D_{Pci} \rangle$ (m)	163								
Deviation from average circular pool diameter, (%)	-14	-34	+10	-24	-13	+23	+31	+31	-9
Vaporization time, t_v (min)	51	1.5	NA	NA	51	33	38	38	40
Average vaporization time, $\langle t_v \rangle$ (min)	36								
Deviation from the average vaporization time, (%)	+42	-96	NA	NA	+42	-8	+5	+5	+11

Obs.: [1] $A_h = 0.44$ m^2. Continuous spill of inventory above waterline of (2/3)(40,000 m^3) ≈ 27,000 m^3; [2] Total volume of continuous spill: 10,000 m^3; [3] Accidental event, = 1 m^2 and $C_d = 0.6$; [4] Used by SNL (2004); [5] Recommended by FERC (2004); [6] FERC (2004) input data; [7] ABS (2004) input data; [8] Present work: (0.0003 m/s and 422.5 kg/m^3)(509.3 J/kg); [9] Calculated from (0.0004 m/s)(422.5 kg/m^3)(509.3 J/kg); [10] Calculated from (0.0007 m/s)(422.5 kg/m^3)(509.3 J/kg); [11] Average inferred between initial and final values, based on FERC (2004) and ABS (2004); [12] Computed in Qiao et al. (2006) assuming zero the final value; [13] LNG reaches the top of the hole and the pool fire reaches the maximum diameter of 108 m in approx. 1.5 min; [14] Inferred from Qiao et al. (2006) for D_h =1 m. [15] From Qiao et al. (2006) for D_h =1 m, with circular pool diameter converted according to Eq. (33). [16] Circular pool diameter according to Eq. (33).

Table 10

Comparison with other models of literature for near shore operations. D_h =5 m , one cargo tank breached. Source: Esteves and Parise (2013a,b)

Results found in the literature and simulations made in the of the present work using Fay (2003) model with Eqs. (20) and (21)									
V_0 = 12,500m^3 D_h = 5 m $A_h \approx$ 20 m^2									
Description	**Data from Johnson and Cornwell (2007)**	**Data from Hissong (2007) (1)**	**Data from Qiao et al. (2006)**	**This work with input data from Otterman (1975)**	**Data from FERC (2004)**	**Data from ABS (2004)**	**This work Input data from FERC (2004)**	**This work Input data from ABS (2004)**	**Data from SNL (2008, 2004) (1)**
Vaporization velocity, $\langle \dot{y} \rangle$ (m/s)	NA	NA	0.0004 (2)	0.0004 (2)	0.0007	0.0007	0.0007 (3)	0,0007 (4)	0.0003
Thermal flux emitted by the pool fire, q'' (kW/m^2)	NA	NA	86 (5)	86 (5)	265	265	151 (6)	151 (6)	220
Release mass flow rate from the cargo tank, $\dot{m}_d''$ (kg/s)	NA	NA	NA	NA	43,000 (7)	65,000 (7)	43,000 (7)	65,000 (7)	NA
Total spill duration, t_d (min)	NA	NA	2 (8)	1	2	1.3	1	1	NA
Circular pool diameter, $D_{p_{ci}}$ (m)	NA	NA	495 (9)	589 (10)	438 (10)	260	525	525	512
Average circular pool diameter, $\langle D_{p_{ci}} \rangle$ (m)	472								
Deviation from average circular pool diameter, (%)	NA	NA	+5	+25	-7	-45	+11	+11	+8
Vaporization time, t_v (min)	NA	NA	NA	3.8	4.2	6.9	3	3	3.4
Average vaporization time, $\langle t_v \rangle$ (min)	4.2								
Deviation from the average vaporization time, (%)	NA	NA	NA	-9	0	+64	-28	-28	-19

Obs.: (1) Intentional event, 12 m² with $D_h = 4$ m; $C_d = 0.6$; (2) Recommended by FERC (2004); (3) FERC (2004) input data; (4)ABS (2004) input data; (5)Calculated from (0.0004 m/s)(422.5 kg/m^3) (509.3 J/kg); (6)Calculated from (0.0007 m/s) (422.5 kg/m^3) (509.3 J/kg); (7)Average inferred between initial and final values, based on FERC (2004), ABS (2004); (8)Inferred from Qiao et al. (2006) for $D_h = 5$ m; (9)From Qiao et al. (2006) for $D_h = 5$ m, with circular pool diameter according to Eq. (33); (10) Circular pool diameter according Eq. (33).

Table 11 - Comparison of thermal plume geometry predictions with results of field tests and values cited in the open literature. Compiled and adapted from: Esteves and Parise (2013a,b), Woodward and Pitblado (2010), SNL (2008), MKOCPS (2008), and TMS (2006)
Sources: (A) Pritchard and Binding (1992); (B) (Moorhouse and Pritchard (1982); (C) Thomas (1965); (D) Zukoski (1995); (E) Steward (1970); (F) Heskestad (2002,1998,1993); (G) Present work

Fire geometry acquired with experimental tests		**Prediction of $\left(L_{\mathbb{V}}/D_{p_{ci}}\right)$ (-)**						
Diameter $\left(D_{p_{ci}}\right)$ (m)	**$\left(L_{\mathbb{V}}/D_{p_{ci}}\right)$ (Substrate)**	**(A)**	**(B)**	**(C)**	**(D)**	**(E)**	**(F)**	**(G)**
8.5 (Test #1of '*China Lake*') U_{wind} = 6.2 m/s	2.8 (water)	2.8	2.0	3.0	4.7	4.1	3.6	**3.0**
9.0 (Test #4 of 'China Lake') U_{wind} = 2.2 m/s	2.8 (water)	2.6	1.9	25	3.9	3.7	3.1	**2.9**
20.0 (Test of 'Thornton Center') U_{wind} = 6.2 m/s	2.15 (land)	2.2	1.6	1.6	2.9	3.1	2.4	**2.5**
35.0 (Test #2 of 'Montoir') U_{wind} = 9.0 m/s	2.2 (land)	2.2	1.6	1.5	2.9	3.1	2.4	**1.9**

The coupling of spill and spreading and non-premixed turbulent pool fire models is discussed in sequence. A global study of the problem, encompassing the two models simultaneously, is presented in Table 12. It shows an overall consistency of results, as depicted in each of Fay (2003) geometry and SNL (2008), using tear area values suggested in SNL (2008), SNL (2004) and ABS (2004). For $\langle \dot{y} \rangle$ = 0.000324 m/s, for example, A_h = 0.78 m² does not affect substantially $Fr_{\mathbb{C}}$ for both $CVCs$.

Consequently, the pool fire geometry, $L_{\mathbb{V}}/D_{p_{ci}}$, as well as the values of $L_{\mathbb{C}}$, $L_{\mathbb{V}}$ and $\psi = L_{\mathbb{C}}/L_{\mathbb{V}}$ are almost identical for both. In two $CVCs$, the axial emissive power along the 'visible' thermal plume increases with the vaporization velocity, while $D_{p_{ci}}$ decreases as the plume geometry increases. Alternatively, $L_{\mathbb{V}}/D_{p_{ci}}$ decreases as A_h increases, in both carrier geometries.

If the heat transfer mechanisms, radiation from the fire plume and boiling by Liedenfrost effect (LNG film contact with sea water) are considered, $\langle \dot{y} \rangle$ increases, thus reducing $A_{p_{sc}}^{max}$. This behavior is consistent with trends for $A_{p_{sc}}^{max}$. When comparing the two geometries, it is expected that a nearly 2-fold increase in cargo volume would produce an increase in t_d and t_v. Taken into consideration the variations of $L_{\mathbb{C}}$ and $L_{\mathbb{V}}$, it is observed that $L_{\mathbb{C}}$ contribution governs the plume geometry, since this region concentrates most of the energy radiated by the fire, which produces $\bar{E}$. Therefore, the higher the $L_{\mathbb{C}}$ the higher the values of $L_{\mathbb{V}}$, $L_{\mathbb{V}}/D_{p_{ci}}$, τ_s and $\bar{E}$ will be in both geometries. On the other hand, C_s will rise slightly for an increase in geometry, and will reduce with D_h. Larger cargo geometries augment t_d and t_v substantially, whereas larger A_h reduces drastically both times, although these variables are not significantly sensitive to the rise of $\langle \dot{y} \rangle$, in each geometry. However, if D_h rises, it represents a drastic reduction in t_d and t_v, and, again, they are not sensitive to the increase of $\langle \dot{y} \rangle$.

Notwithstanding the fact that $D_{p_{sc}}$ and $D_{p_{ci}}$ increase with geometry, $L_{\mathbb{V}}/D_{p_{ci}}$ decreases as D_h rises, for each corresponding value of $\langle \dot{y} \rangle$. The same reduction trend is observed for τ_s and $\bar{E}$, as A_h augments.

Table 12 demonstrates that $L_{\mathbb{V}}/D_{p_{ci}}$ is insensitive to the 2-fold scale up of carrier capacity. These results demonstrate the numerical robustness and coherence of results when the spill-combustion model coupling is used.

Table 12 - Results of coupling of pool spill/spreading with pool fire models

Coupling of spill and spreading and turbulent combustion models – Prediction results									
Geometry	Parameter	$D_h = 1$ m - $A_h \approx 0.8$ m^2				$D_h = 5$ m - $A_h \approx 20$ m^2			
		$\langle \dot{y} \rangle$ x 10^{-4} (m/s)							
		2.10	**3.24**	**8.00**	**11.0**	**2.10**	**3.24**	**8.00**	**11.0**
Fay (2003) [1]	t_d (min)	27.1	27.1	27.1	27.1	1.1	1.1	1.1	1.1
	t_v (min)	38.3	38.3	38.3	38.3	5.4	4.4	3.0	2.7
	$A^{max}_{p_{sc}}$ (m^2)	118,560	78,845	31,122	22,634	405,919	334,761	214,460	183,511
	$D_{p_{sc}}$ (m)	549	442	282	240	1017	923	739	684
	$D_{p_{ci}}$ (m)	388	313	199	170	719	653	523	483
	$Fr_{\mathbb{C}}$ (-)	0.001221	0.002098	0.006497	0.009665	0.000897	0.001453	0.004008	0.005734
	$L_{\mathbb{C}}$ (m)	-	9	58	83	-	-	73	119
	$L_{\mathbb{V}}$ (m)	244	282	381	424	368	461	726	851
	$\psi = L_{\mathbb{C}} / L_{\mathbb{V}}$ (-)	-	0.03	0.15	0.20	-	-	0.10	0.14
	$L_{\mathbb{V}} / D_{p_{ci}}$ (-)	0.63	0.90	1.91	2.49	0,51	0.70	1.39	1.76
	C_s (kg/m³ x 10^{-4})	4.26	4.19	4.10	4.0	4.4	4.4	4.3	4.3
	τ_s (-)	1.3E(-6)	2.15E(-5)	1.35E(-3)	3.79E(-3)	≈0	≈0	8.0(E-9)	3.7E(-9)
	$\bar{E}$ (kW/m^2)	74	89	119	130	66	79	106	115
SNL (2008)(Q-max) [2]	t_d (min)	70.1	70.1	70.1	70.1	2.8	2.8	2.8	2.8
	t_v (min)	99.1	99.1	99.1	99.1	7.7	6.6	4.0	4.1
	$A^{max}_{p_{sc}}$ (m^2)	147,056	95,314	38,602	28,074	967,597	785,065	451,263	362,350
	$D_{p_{sc}}$ (m)	612	493	314	267	1,570	1,414	1,072	961
	$D_{p_{ci}}$ (m)	433	348	222	189	1,130	1,014	766	685
	$Fr_{\mathbb{C}}$ (-)	0.001156	0.001990	0.00615	0.009167	0.000716	0.001166	0.003312	0.004815
	$L_{\mathbb{C}}$ (m)	-	7	60	87	-	-	75	130
	$L_{\mathbb{V}}$ (m)	262	303	410	455	497	618	936	1,074
	$\psi = L_{\mathbb{C}} / L_{\mathbb{V}}$ (-)	-	0.024	0.15	0,19	-	-	0.08	0.12
	$L_{\mathbb{V}} / D_{p_{ci}}$ (-)	0.61	0.87	1.85	2.41	0.44	0.61	1.22	1.57
	C_s (kg/m³ x 10^{-4})	4.3	4.2	4.1	4,0	4.6	4.5	4.4	4.4
	τ_s (-)	2.4E(-7)	5.9E(-6)	5.93E(-4)	1.93E(-3)	≈0	≈0	≈0	≈0
	$\bar{E}$ (kW/m^2)	73	87	118	128	60	73	101	111

[1] Carrier #1 geometry: CVC = 125,000 m^3; CTV = CVC/5 =25,000 m^3; Assumed a carrier with NT = 5 membrane cargo tanks with one cargo tank breached; V_o = 12,500 m^3; DR = 11.8 m; h_0 = 13 m. [2] Carrier #2 geometry: CVC = 265,000 m^3 (Q-max); CTV = CVC/5 = 53,000 m^3; Assumed a carrier with NT = 5 membrane cargo tanks with one cargo tank breached; V_o = 41,000 m^3; DR = 12.5 m; h_o = 20 m. When necessary, pool areas and diameters were converted according to Eqs. (32) and (33).

An accident with an LNG carrier redounds in potential hull/cargo tank breaches and the fluid dynamics of a large spill onto the sea water, and the hazards thereof, are phenomena not completely comprehended and interpreted. Some motives contribute: (i) modern carriers are constructed under rigid codes as well as strict safety and environmental regulations, making this industry an example of excellence in accidents occurrence, reducing drastically its history.

So, there is a scarcity of information as well as empirical data about large tears/spills/groundings; (ii) another aspect is that field data acquired from experimental events cover spills volumes poured onto water with about two orders of magnitude less than the spills inventories assumed in recent studies. The result from these evidences is the lack of experimental data, leading to assumptions and simplification of the hypothesis that not always correspond to reality, to determine the actual size of hazards. In this research report, spills were supposed to occur from breaches with two diameters of 1 m and 5 m perpetrated accidently or not against the carrier hulls, with the lower edge coincident with the sea water line. The outflow rate is calculated using the orifice model, considering the flow rate as time dependent and dropping with the decrease of the height of the liquid above the hole. The cross sectional area, A_t, of the cargo tank is assumed to be constant. So one has

$$\dot{m}''_{\mathrm{d}}(t) = C_{\mathrm{d}}\rho_{\mathrm{l}}\pi\left(\frac{D_{\mathrm{h}}}{2}\right)^2 \sqrt{2g\,h(t)} \tag{114}$$

Although the flow rate is a time dependent function, a conservative initial value can be determined when $t = 0$. Therefore, conservatively, its initial value can be calculated, $\dot{m}''_{\mathrm{d}}(t=0) = \dot{m}''_{\mathrm{d,o}}$ when $h(t) = h_{\mathrm{o}}$ and with $C_{\mathrm{d}} = 0.65$ (FERC, 2004)

$$\dot{m}''_{\mathrm{d,o}} = C_{\mathrm{d}}\rho_{\mathrm{l}}\pi\left(\frac{D_{\mathrm{h}}}{2}\right)^2 \sqrt{2g\,h_{\mathrm{o}}} \tag{115}$$

10. Modelling the downwind distances – Background, results, findings and discussions

10.1. Background

We consider the carrier operating in quiescent waters when moored at the terminal, in near-shore operations, and an accident is supposed to breach one cargo tank only. ABS (2004) uses the steady state Bernoulli's equation and an approximation of axisymmetric spread on water, with gravitational and inertial resisting forces, as developed by Webber, and according to TNO (1997, 2005). This approach assumes a self-similar solution of the shallow water and lubrication equations. In this formulation, we included the resistance by turbulent or laminar friction effects, and Webber provides methods to estimate the various values needed, including friction effects, reason why ABS (2004), probably, have chosen this model.

FERC (2004) considered the inclusion of some suggestions in the ABS (2004) report such as: (i) use discharge coefficient of 0.65 to the calculations of outflow from the ship; (ii) approximate the pool shape as a semicircle, rather than a circle; (iii) estimate the friction between the LNG pool and water surface based on shear stress in the vapor film; (iv) use an improved method of handling effect of decreasing spill rate on pool spread; (v) adopt a value of 85 kW/m² for heat flux from the water to the LNG pool; vi) Incorporate two-zone pool fire model. Items i), ii) and (vi) were included in the formulation of the present work.

Neither ABS (2004) nor SNL (2004,2008) mentioned explicitly that the extended diameter was used. On the other hand, ABS presented solid evidence on page C-25, where they considers **explicitly** this diameter, since the tilt and the drag affect the flame length. FERC did not mention which diameter, extended or non-extended they used, which leads to suppose that FERC follows the ABS march. Anyway, this research report considers and models/test **both cases**, and selected the extended diameter hypothesis, to be more realistic.

An equivalent approach we develop in the present work, with Eqs. (1) to (7). As discussed, this work uses Fay/MIT (2003) model to describe the LNG pool spill and spreading onto the sea. On this account, one considers that the pool decelerates with spread and evaporation, which flow motion we assumed as frictionless with an inviscid fluid. During the pool spreading, this flow would transit from 'gravity-inertia' to 'gravity-viscous' regime.

Raj (2007) and Fay (2006) models address the pool combustion and flame geometry, where the column as a solid flame with three regions with the surface emissive power varying with flame length. We modelled the scenarios also with the hypothesis that the spill occurs on the downwind side of a ship (SNL, 2011).

It is important to emphasize that one cannot apply the scenarios to all sites. It is necessary to develop hazard analyses prior to incorporate the appropriate conditions and peculiarities of the surroundings. Thus, all the distances we provide in this report are 'non-site specific' and will change according to the site characteristics. We discuss some of these complexities below.

Experimentally, the open literature cites that higher burn velocities result in smaller pools, as well as its reverse. As a cryogenic, LNG burns faster than the other hydrocarbons with higher molecular mass, by around one order of magnitude (SNL, 2011). The physics of the problem defines that this mass burn rate affects the time average of the flame length L_{V} , so that higher rates increase this length. The TMS/Raj (2006, 2007) combustion model defines this height as intermittent, i.e., the fire column has its height defined in a given fraction of time by the locus of its tip. In the same fashion, wind speed affects burning velocities, so that the trend is the wind that stimulates the velocity increase (SNL, 2011).

View factors are strongly dependent on flame length at distances higher than one pool diameter, and by other turn, these factors determine how much radiant flux will strike the surrounding resources. Hence, increasing the flame length (and view factor) increases the heat flux and downwind distances. On the other hand, an increase in burn velocity will tend to reduce downward distances as a function of the pool diameter reduction, because the pool burns faster. In addition, this mechanism competes with the associated increase in flame length, tending to increase hazard distances.

The competing balances that govern this geometry will depend utterly upon the diameter of the fire. In the same fashion, wind can affect flame geometry, reducing the length by about 10-40%, depending on pool diameter, wind velocity, and other correlations as well (SNL, 2011). The predictions of wind tilt correlation can have wide disparity depending on the pool size and local wind, so their range of validity is applicable to much smaller pool diameters.

Practice demonstrates that it is complex to quantify the exact effects of wind on flame length for pools of very large diameters [100 m, SNL (2004)] considering that "all of the LNG fire studies reviewed assume that a single, coherent [19]pool fire can be maintained for very large pool diameters" (SNL, 2004). Large fires of turbulent diffusion induce strong buoyancy forces, and this effect may compromise the flame tilt, so that it would be significantly less than that predicted by smaller scale test data.

The key aspect is that the wind effect will reduce flame height from that of quiescent conditions. Thus, using flame height data applicable to quiescent conditions for wind environments, it will provide conservative predictions with longer downwind hazard distances.

When a solid cylinder represents fire column, it may over predict view factors, if compared to those from actual flame shapes. Therefore, for the predicted fluxes incident at the various distances, one can expect that it may be higher than average values observed experimentally. By virtue of the correlations among flame height, its geometric L_v/D_{pci} ratio, transmissivities and view factors, small pool diameters will tend to provide shorter downwind hazard distances.

The hazard distances were modeled using thermal radiation flux couplings. We used (i) TMS/Raj's model for surface emissive power varying with the flame height, instead of the fixed value of 265 kW/m² initially used by ABS and FERC; (ii) Beyler/NFPA (2002) model for view factors; and (iii) AIChE and TMS equations to model for the atmospheric vapor pressure, and three combinations of these to calculate air transmissivity. This work adopts the following equations to calculate the atmospheric transmissivity and the view factor between the flame surface and the target:

- Extended diameter
    - Transmissivity: TMS (2006) and AIChE (2002)
    - Saturated vapor pressure of water in the atmosphere: AIChE and TMS
    - View factor: ABS = NFPA

We used the criteria to define the best prediction for downwind hazard distances: (i) to be the closest possible to each one of the ABS or FERC results, and (ii) if the result could not match, then the choice was to consider the furthest (safest) distance from the flame surface. Thus, neither ABS nor FERC presented different predictions, for both tear sizes, 1 m and 5 m.

We considered the most important downwind distance, that which corresponds to the thermal flux of 5 kW/m², since it focus the vulnerable resources surrounding an LNG facility. The literature considers this value as a consecrated cut set used by most of the international regulatory Authorities for the public, residences atnd the likes. ABS presented the safer distance of 860 m and 1,400 m for this radiation level with tears of 1 m and 5 m, respectively. In the present work, we considered two models for atmospheric pressure (AIChE and TMS), three equations for transmissivity modelled with the TMS and AIChE equations combined alternatively, and two models for the view factor considering NFPA and ABS equations.

We tested five combinations of equations to calculate the thermal flux, considering downwind distances counted from the center of the dragged flame column. The best fit for the ABS and FERC results was obtained with the combination of the transmissivity with atmospheric vapor pressure given the AIChE equations and view factor determined by the equations of ABS (or NFPA).

10.2. Prediction of the downwind distances

In 2004, SNL published a wide review about the LNG literature available at that time. In 2008, Sandia updated that report to include raise on the carrier capacities. They jumped from 180,000 m³ to 265,000 m³.

Later on, SNL (2011) developed a series of tests in Albuquerque, N.Mex., to improve the understanding of the physics and hazards of large LNG pool fires, and to acquire learning and updated information about the experiments. They were the largest fire tests performed on water or land to date, using a pool with diameter of 83 m resulting in a pool fire 56 m wide.

The 2004 and 2008 SNL reports consider the parameters obtained in 1979, but with much smaller scale. In addition, in other hand after treatments and refinements, the 2011 tests provided the best experimental data acquired to date. The results of are conservative, once the thermal hazard distances are around 2% and 8% lower than the previous 2004 and 2008 SNL's reports. The downwind distances also varied, depending upon the site considered, prevailing conditions and scenarios. In other words, the results are site-specific.

During those tests, one could observe the potential of hydrates formation, although unstable, in locations with water temperatures nearly above the freezing. Based on those tests, SNL (2011) sustains that ice/hydrates formation is possible to occur. Although, its structural stability may decrease with warmer water and surrounding stir caused by spillage and/or ocean conditions.

Hence, for safety purposes, one can postulate a conservative bias assuming that in marine environment will not form hydrates. Some of the factors are tropical seawaters, presence of waves and currents, agitation, salt content, water temperature around 273 K (even warmer).

Atmospheric pressure plays an important role in thermal radiation attenuation, since the local pressure varies with elevation. The Albuquerque tests occurred in a site with ambient pressure 17 % below that of the sea level, while the Montoir and China Lake experiments occurred at sea level in a LNG terminal. The extension of the atmospheric pressure interference on soot production in turbulent diffusion flames is a field of research.

The flame length depends on the burning velocity, so the higher the velocity the higher this length will be. The flame length is also sensitive to view factors if the distance between the pool center and the target is above about one pool diameter. View factors

[19] The pool fires modelled herewith are supposed to be **'coherent'** with 'column shape' (or *en masse*), inclined or vertical. This work does not consider the hypothesis of fires with 'flamelet elements'.

define the radiation quantity striking surrounding objects. So an increase in flame length and configuration factor implies in increase of the thermal flux on surrounding resources, increasing therefore the downwind hazard lengths. Generally, an increase of the burning velocity tends to shorten downwind distances due to pool diameter reduction but, otherwise, the collateral increase of the flame length provokes an increase of those distances. What effect will govern this competition is a function of the pool diameter.

Local wind velocity tilts and drags the fire column determining its height, but its action may reduce the burning velocity and the correlation between height and pool diameter. Fires of great diameters produce buoyancy momentum induced by whirls and vortex strain/stress inside the plume, reducing its height when compared to quiescent conditions. These two effects combined can decrease/increase downwind hazardous distances, which is a function of the target position from the pool center and how much is the column tilted. Wind also affects burning velocities, so that an increase in wind conditions will dictate an increase in the velocity with which the fuel will burns, or the fire would become extinct.

The transmissivity decreases with the increase of the atmospheric pressure and humidity. Usually, the correlations available consider the fire as a solid column and black/grey body emitting radiation at 1,500 K or above. Humidity and carbon dioxide are the main responsible for this decrease.

At a given temperature and atmospheric pressure and with the same path length, a reduction in relative humidity will raise the transmissivity. In the same token, the higher the temperature the higher the transmissivity and downwind distances will be. This effect becomes even greater above about 1,000 m from the pool fire center. In summary, high transmissivity offers little scattering and resistance to thermal energy across the path length, resulting in longer downwind distances.

Table 13 ahead summarizes the results of all predictions of the downwind distances for four radiation levels. We obtained the results using different models of ABS (2004), FERC (2004) and the present work.

The results of Table 13 demonstrate that this work reproduces, with fair approximation, the results of ABS (2004) and FERC (2004). ABS and FERC used a constant SEP of 265 kW/m² alongside the flame axle, and the same circular pool diameters of ABS (2004), i.e., 148 m (for 1 m breaches) and 260 m (for 5 m breaches). However, this work considers Fay (2003) and Raj/TMS (2007) models, respectively, for pool spill/spreading and turbulent diffusion combustion of the pool. Alternatively, two other predictions were added, with time averaged SEPs of 111 kW/m² (1 m hole) and 106 kW/m² (5 m hole), calculated using Raj/TMS (2007) combustion model, which will be discussed in sequence.

To compile this table, the comparison of the results used three approaches. The first, considered the original SNL (2004) values with a 1.1 m hole on the carrier hull, SEP of 265 kW/m² used for comparison with the correspondent hole (1 m) of ABS, FERC and of this work. When the hole diameter rises to 5 m, the closest SNL (2004) diameter available was 3.9 m (12 m²). If SNL (2004) had used the 5 kW/m² hazard distance could had been even greater than the 1,920 m obtained from using the 3.9 m diameter.

The second SNL approach, updated the original data of the 2004 report including the results of the Albuquerque, NM tests. Here, the closest value available for the 1 m hole diameter was 2.5 m (5 m², the nominal case). The lower / upper bounds rose, respectively, to 436 m / 1,266 m, which is expected, providing the high transmissivity (0.8) and the SEP of 286 kW/m² used, when compared with the previous of 220 kW/m² and 265 Kw/m² of ABS, FERC and of this work. When the hole is 5 m wide, the best SNL fit was 3.9 m (12 m²). One can observe that both upper and lower bounds converge better with 629 m / 1,755 m to the corresponding ABS (600 m / 1,400 m), FERC (620 m/ 1,500 m) and this work (660 m/1,540 m) for a SEP of 265 kW/m².

The third was to include the updated results obtained with the original SNL (2008) report to 2011, for near-shore operations with intentional event. It should be noticed that in 2008, the carriers geometry changed significantly, increasing the spilled volume from 12,500 to 41,000 m³, and the initial height of liquid within the cargo tank from 13 m to 20 m. For a 1 m hole (0.8 m²), the closest SNL value available was the nominal case with 2.5 m (5 m²).

As expected, both upper and lower bounds rose to 463 m and 1,338 m, respectively, compatible with a carrier geometry 3.3 times the original and a hole area 6.3 times bigger. When the 5 m hole is taken into consideration, SNL (2011) provides a maximum diameter of 3.9 m (12 m²). The higher bound rose to 1,849 m and the lower to 668 m. Notice that, in this case, the hole area (12 m²) is 60% lower than the 20 m² (with a 5 m hole) considered by ABS, FERC and this work. If they were even, it is plausible to infer that, in the same token, the downwind distances 668 m and 1,848 m would rise substantially.

Some considerations about the SEPs 111 kW/m² (1 m hole) and 106 kW/m² (5 m hole) are here discussed**. The Raj/TMS (2007) combustion model used in this work, considers the SEP as a time average quantity, varying alongside the flame length**, based on experimental data acquired with the experiments of China Lake (substrate: water) and Thornton Center and Montoir (substrate: land) even that with smaller diameters, as discussed in Table 11 and Fig. 7. Raj/TMS (2007) postulated that in the 'intermittency zone' (zone 2), the SEP varies because of smoke shrouding. It was assumed that the rate of intermittency varies between 0% (or 0) (no smoke obscuration) just at the top of "clean burning zone" to 100% (or 1)(full smoke obscuration) at the top of this zone. This probability, $0 \le p(\xi) \le 1$, can also be interpreted as **the fraction of the time that the outer layers of the cylindrical fire show the "inner core" thus radiating at the maximum SEP**; the rest of the time the emission is from the smoke layers.

ABS and FERC otherwise used a different and equivalent approach, based also on previous tests, but considering the SEP as a constant quantity, alongside the whole fire column axle, independently of the height of this position . This is a conservative non-variable value of 265 kW/m². SNL (2011) in the same token adopts a value even more conservative and a non-variable value of 286 kW/m² measured from the Albuquerque experiments.

It is important to notice that both approaches are valid, giving all the research work put here into perspective. The only purpose of this work is to bring this discussion, offering another alternative to exercise the engineering judgment, providing the results of Montoir, France, and Albuquerque, N.Mex., field experiments. Table 13 summarizes the results.

Table 13 – Thermal radiation distances. Present work vs. FERC (2004), ABS (2004) and SNL (2004,2008,2011)
Complied and adapted from Esteves and Parise (2013a,b), FERC (2004) pages 22-25, ABS (2004) pages 19 and 34, and SNL (2004,2008,2011). NA: Not Available

Parameter analyzed	ABS (2004)	FERC (2004) [1]	SNL			Present work (2017)		ABS (2004)	FERC (2004) [1]	SNL			Present work (2017)	
			(2004) [2][3]	(2011) [2][4]	(2011) [2][5]					(2004) [2][6]	(2011) [2][7]	(2011) [2][8]		
Tear diameter, D_h (m)	1	1	1.1	2.5	2.5	1	1	5	5	3.9	3.9	3.9	5	5
Hole area (1 tank breached), A_h (m²)	0.8	0.8	1	5	5	0.8	0.8	20	20	12	12	12	20	20
Initial LNG height in the cargo tank, h_o (m)	13	13	15	15	20	13	13	13	13	15	15	20	13	13
Initial spill volume, V_o (m³)	12,500	12,500	12,500	12,500	41,000	12,500	12,500	12,500	12,500	12,500	12,500	41,000	12,500	12,500
Local air temperature, T_a (K)	300	300	NA	269	269	311	311	300	300	NA	269	269	311	311
Local relative humidity of the air, RH (%)	70	70	NA	20	20	70	70	70	70	NA	20	20	70	70
Local wind speed, u_{wind} (m/s)	8.9	8.9	≈ 0[9]	≈ 0[9]	≈ 0[9]	8.941	8.941	8.9	8.9	≈ 0[9]	≈ 0[9]	≈ 0[9]	8.941	8.941
Initial spill rate, $\dot{m}''_{d,o}$ (m/s)	5,300	3,400	NA	NA	NA	3,440	3,440	130,000	86,000	NA	NA	NA	86,000	86,000
Spill time, t_d (min)	33	51	NA	NA	NA	27	27	1.3	2	NA	NA	NA	1.1	1.1
Fire burning velocity, $\langle \dot{y} \rangle$ (m/s)	0.00067	0.00066	0.0003	0.00035	0.00035	0.00067	0.00067	0.00067	0.00066	0.0003	0.00035	0.00035	0.00067	0.00067
Fire burning rate, $\dot{m}''_V$ (kg/m².s)	0.282	0.28	0.135[10]	0.147[11]	0.147[11]	0.282	0.282	0.282	0.28	0.135[10]	0.147[11]	0.147[11]	0.282	0.282
Fire duration, t_V (min)	33	51	40	8.1	23	38	38	6.9	4.2	3.4	3.4	10	3	3
Circular pool diameter, $D_{p_{ci}}$ (m)	148[12]	283[12]	148	306	329	148	148	260	877	512	474	509	260	260
Time average SEP, $\overline{E}$ (kW/m²)	265	265	220	286	286	265	111[13]	265	265	220	286	286	265	106[13]
Local air transmissivity, τ (-)	NA	NM	0.8	0.8[14]	0.8[14]	0.54	0.54	NM	NM-	0.8	0.8[14]	0.8[14]	0.51	0.51
Tilt angle at maximum flame radius, ϕ (º)	35	36	≈ 0[9]	≈ 0[9]	≈ 0[9]	36	36	31	27	≈ 0[9]	≈ 0[9]	≈ 0[9]	25	25
Flame drag ratio at maximum length (-)	1.24	1.24	≈ 0[9]	≈ 0[9]	≈ 0[9]	1.24	1.24	1.19	1.15	≈ 0[9]	≈ 0[9]	≈ 0[9]	1.19	1.19
Flame length L_V (m)	280	280	NA	390[15]	390[15]	264	264	430	630	NM	520[15]	490[15]	399	399
Maximum length of the clear flame L_C (m)	NA	180	NA	NA	NA	39	39	NA	270	NA	NA	NA	48	48
Clear fire ratio $\psi = L_C / L_V$ (-)	NM	0.64	NA	NA	NA	0.15	0.15	NA	0.43	NA	NA	NA	0,12	0.12
Fire column geometry, $L_V / D_{p_{ci}}$ (-)	1.89	0.99	NA	1.27	1.27	1.78	1.78	1.65	0.72	NA	1.1	0.97	1.53	1.53
Downwind distance,38 kW/m² (m) [16] [17]	370	280	177	436	463	350	200	600	620	602	629	668	660	380
Downwind distance, 25 kW/m² (m) [16]	450	340	NA	NA	NA	420	270	720	760	NA	NA	NA	800	510
Downwind distance, 12 kW/m² (m) [16]	600	460	NA	NA	NA	570	400	980	1,100	NA	NA	NA	1080	740
Downwind distance, 5 kW/m² (m) [16] [17]	860	650	554	1,266	1,338	800	570	1,400	1,500	1,920	1,755	1,849	1,540	1,060

[1] Discharge coefficient of 0.65. [2] Discharge coefficient of 0.6. [3] Accidental event, as the original 2004 report. [4] Original report of 2004 updated to 2011 with intentional event and nominal case (5 m² hole), incorporating results of the Albuquerque (NM) tests. [5] Report of 2008 for near-shore operations, updated to 2011 with intentional event and nominal case (5 m² hole), incorporating results of the Albuquerque (NM) tests. [6] Intentional event, as the original 2004 report. [7] Intentional event, original report of 2004 updated to 2011, incorporating results of the Albuquerque (NM) tests. [8] Report of 2008 for near-shore operations, updated to 2011 with intentional event and incorporating results of the Albuquerque (NM) tests. [9] No-site specific. Low wind condition was assumed; hence, flame tilt and drag were not considered. [10] Calculated with (0.0003 m/s)(450 kg/m³). [11] Same, with (0.00035 m/s)(420 kg/m³). [12] Extended diameter. [13] Using Raj/TMS (2007) model. [14] Using the Wayne equation. [15] Estimated with the Eq. (1) Page 23 of SNL (2011). [16] From the center of the pool. [17] 37.5 kW/m² causing damage to process equipment after 10 min of exposure; 5 kW/m², level at which second degree burns occur on bare skin after 30 seconds of exposure…

10.3. Results, comparisons with literature and discussions

Thanks to the fluid mechanics (fuel, gases and soot) within a fire column, very low Froude numbers governs turbulent diffusion flames of coherent fires when occurring, with non-premixed combustion. It involves vorticity (whirls/recirculation) and vortex strain/stress. Vorticity induces fire whirls transporting hot combustion products of lower density in an upward convective draft, interacting with external colder atmospheric air. Large pool diameters on the other hand, make difficult the air intake through its lateral surface lowering the combustion efficiency caused by smoke formation. As this process advances in time, there is more smoke formed reducing the surface emissive power, making this a time-averaged quantity. Local atmospheric conditions at high elevations above the sea level, low barometric pressure, temperature and relative humidity, may affect the draft of the combustion products through the upper tip of the fire column, which is a 'time loci' of the flame pulsating tips. On this account, the fire may form less smoke, affecting the flame geometry, L_V/D_{pci} (which depends much on Froude number), with a tendency to form higher and more dangerous thermal plumes;

I. Hence, tall and very light flames will be formed (vivid yellow color) in most of its extension, with strong smoke drafts of high inertia, converting efficiently the chemical energy content of the fuel into light. That seems to be the case of the China Lake (Cal.) and Albuquerque (N.Mex.) tests. An opposite situation is expected with fires at sea level, tending to form fires with reddish-yellow color, with much more smoke, opening bare 'intermittent windows of light', consequently with lower SEPs due to the presence of smoke. That seems to be the case of the Montoir (France) tests;
II. The models used in this report have different approaches in their formulations from those of ABS (2004) and FERC (2004) reports, both for the pool spreading and its combustion. Therefore, one can expect that differences would occur in the predictions results. However, despite the differences, in the overall context, the results keep consistency about the description of the phenomenology itself. When Table 13 ahead is put into perspective, some evidences and results can be withdrawn;
III. This work used the same circular pool diameters of ABS (2004), 148 m (1 m hole) and 260 m (5 m hole), SEP of 265 kW/m² and burning velocity of 0.00067 m/s of ABS and FERC. We considered the local temperature as 311 K, atmospheric pressure at the sea level and high relative humidity (70%), typical for tropical waters. , with transmissivity around 0.6, Evidences confirm that the models used in this work (Fay/MIT for spill/spreading and pool and Raj/TMS's for pool combustion), reproduced fairly the results obtained by those Organizations;
IV. We used the same fire burning velocity and combustion rate of ABS and FERC. However, these values are about the double of the SNL values, reason why this work, ABS and FERC present smaller diameters with both tear diameters ('fast' burn). Under this circumstances, our results are coherent;
V. This work compared our results to the SNL (2011) experimental test data. Despite of the different values of fire burning rates, the circular pool diameters and fire durations times seem to be of the same order of magnitude for both tear diameters. The coherent time scale used by all references supports a plausible mathematical modelling to describe properly the phenomenology of the problem;
VI. Two approaches for the SEP (Beyler/NFPA, Mudan), two for the view factor $\mathcal{F}$ (Beyler/NFPA, Mudan), and three for the air transmissivity τ (TMS, TNO, AIChE) were investigated in this work. The best choice to reproduce the results of ABS (2004) and FERC (2004) focused, respectively, NFPA, NFPA and AIChE. The results found with this work for not dragged and dragged columns reproduced fairly the same results of both ABS and FERC's, although somewhat conservatively with transmissivities of 0.54 and 0.51, provoking shorter distances from the center of the pool fire, as expected with the SEPs of 111 (1 m hole) and 106 kW/m² (5 m hole);
VII. There are some discrepancies between the L_C/L_V ratios of this work when compared to FERC. One can analyses the root cause of this discrepancy based on the experiment of Albuquerque: the locations used to run the tests and, subsequently, the models developed. The Montoir terminal, used by Raj to developed his 3-zones solid flame model of this work, and the desert of Albuquerque, the site where SNL formulated its model. The first test took place at the sea level in a land dike of a terminal, and the second was directly on a water pond in a desert site. This site was on an elevation above the sea level, providing atmospheric pressure about 20% lower than that of sea level. Besides, lower temperature (269 K vs 311 K of this work) and very low relative humidity (20% vs 70% of this work) used by SNL (2011) are also determinant factors. First, a heavy sooty plume of fire was formed, shortening the length of the 'clean' combustion zone to 15 % (with 1 m hole) of the total flame length, whereas the SNL clean combustion length was substantially longer with much less soot as depicted in the photos of its report of 2011. Only FERC reported a L_C/L_V ratio of 0.64 for the 1 m hole, but with no information available for discussion;
VIII. The L_V/D_{pci} ratios for holes of 1 m and 5 m found with work are, respectively, 1.78 and 1.53. ABS found 1.89 and 1.65, FERC found 0.99 and 0.72 and SNL (2011) found 1.27 and 0.97. We explain this difference because each source used a different model from each other to calculate the same dimensionless number; 32.5/13.3
IX. Tilt angles are practically the same of ABS and FERC (36°) for 1 m hole and a small deviation from FERC (25°) for 5 m holes. SNL (2011,2008,2004) did not take into consideration the action of wind due to the non-site specific approach adapted in their reports, therefore no tilt was considered;
   Drag ratios at maximum flame length are practically the same for ABS (1.24; 1.19), FERC (1.24; 1.15) and this work (1.24; 1.19), with both tear diameters (1 m; 5 m). In the same fashion, it happens with tilt angles, although the flame is not susceptible to drag by SNL. It suggests a fair agreement of results;
X. The downwind distances for the thermal radiation levels of fluxes of 38 (37.5 used by SNL), 25, 12 and 5 kW/m², considered two approaches: flame without and with drag. ABS (2004) used flame with drag, in accordance with its calculation memory.

XI. We could not withdraw any information from FERC. We set two main radiation levels are of concern: upper bound with 38 (or 37.5) kW/m², for equipment exposed for more than 10 minutes and the lower bound with 5 kW/m², for second degree burns on bare skin after 30 seconds;

For tears with 1 m nominal diameters and using the same SEP of ABS and FERC (265 kW/m²), this work predicts, respectively, 350 m for 38 kW/m² and 800 m for 5 kW/m², against 370 m for 38 kW/m² and 860 m of ABS for 5 kW/m². FERC found 280 m for 38 kW/m² and 650 m for 5 kW/m², and in the case of SNL (2011)[20] adopting a SEP of 286 kW/m², the results were 463 m for 38 kW/m² and 1,338 for 5 kW/m².

Going further for tears of 5 m, the same profile can be observed. This work predicted 660 m for 38 kW/m² and 1,540 m for 5 kW/m², against 600 m for 38 kW/m² and 1,400 m for 5kW/m² of ABS. In the case of FERC, the values were 620 m for 38 kW/m² and 1,500 m for 38 kW/m², and in the case of SNL (2011)[21] using the same SEP of 286 kW/m², the results were 668 kW/m² for 38 kW/m² and 1,849 m for 5 kW/m².

SNL found 668 m for 38 kW/m² and 1,849 m for 5 kW/m², using a transmissivity of 0.8 combined with a local temperature of 269 K and relative humidity of 20%. On the other hand, this work adopted a transmissivity of 0.54 combined with a local temperature of 311 K and relative humidity of 70%. Considering the differences of premises, models, approaches and experimental data used in both cases, the results found with our work present reasonable plausibility;

XII. Some considerations are given about the SEPs of 111 kW/m² and 106 kW/m², respectively for 1m and 5m hole diameters. To simulate these values, we used a three zones model for pool fires to predict this item according to the Raj/TMS (2007). Addionally, that model takes into consideration soot formation just above the 'clean' combustion zone. As discussed, depending on the atmospheric conditions where the fire takes place, longer or shorter 'clear' flame lengths may occur. The greater the smoke formation within the fire column, the shorter this 'clean' combustion zone will be. Furthermore, the shorter they are the less emissive power the fire will emit outside the plume to propagate in the path length to strike on surroundings resources. This is the key point and the reason why we obtained the fluxes of 111 kW/m² and 106 kW/m² using Raj's model based on the Montoir tests, and SNL used 286 kW/m² based on the test data acquired with Albuquerque experiments. In fact, two approaches can be derived from these two conceptual models proposed [SNL (2011) and Raj/TMS (2007)], depending on the local weather/elevation conditions where the fire may occur. This work raised the question and presented the results that may be considered or not, opening possibilities to decide the most adequate model for the specific situation (and location) in question. The main aspect to be observed is that Table 13 shows solid evidences that if the Raj/TMS (2007) model is used, the downwind hazard distances may be reduced to about half of those predicted by ABS (2004), FERC (2004) and SNL (2011) models. That is, depending on the approaches and premises assumed by each model different results may be obtained;

XIII. To confirm above assertive, we reproduce in the Table 14 a comparison between the hazards distances modelled with different codes (TMS, 2006).

Table 14 – Comparison of downwind distances simulated with different model approaches.
Source: TMS (2006).

Fire diameter $D_{P_{ci}}$ (m)	Downwind distances from the fire center to a vertical target at ground level, X_0 (m)					
	Thermal flux, $\dot{q}''$ (kW/m²)					
	31.5			5		
	NFPA 59A Point source model	LNGFIRE3 ®	TMS (2006)	NFPA 59A Point source model	LNGFIRE3 ®	TMS (2006)
20	63	96	103	24	32	34
30	95	137	148	36	46	51
50	158	213	213	61	75	80
100	316	388	340	121	143	137
200	632	707	570	242	271	242
300	948	1003	785	363	393	340

The evidences postulate that when the overall SEP of the fire column remains with a constant average value irrespectively to the fire diameter. It does not take into consideration that the fire becomes even sootier with the diameter increase. Depending on the site where the fire takes place, if the fire becomes sootier, the SEP over the fire surface decreases with the increase of fire diameter. This is precisely what the SEPs of 111 kW/m² and 106 kW/m² presents. 41.6/11.6

XIV. We calculated these two values for the SEPs (or $\overline{E}$), 111 kW/m² and 106 kW/m². We used the Eq. (75), considering parameters acquired experimentally from the China Lake and Montoir tests (Raj, 2007a,b; TMS, 2006). The SEPs are function of several parameters, such as diameter of the fire column, concentration of soot particles. The optical thickness represents the reduction of a fire column to irradiate with its maximum capacity due to combustion inefficiencies and presence of particulate material in the soot (combustion products). This approach is different from the conservative and fixed values of 265 and 286 kW/m² used by ABS, FERC and SNL, reason why we obtained different results;

[20] Report of 2008 for near-shore operations, updated to 2011 with intentional event and nominal case (5 m² hole), incorporating results of the Albuquerque (NM) tests.

[21] Report of 2008 for near-shore operations, updated to 2011 with intentional event and incorporating results of the Albuquerque (NM) tests

XV. According to Table 13, it is possible to conclude that no matter the model used to calculate the downwind distances, the results will be about of the same order of magnitude. Using the models of ABS (2004), FERC (2004), and SNL (2011) or of the present work (using ABS data), the downwind distances for 38 kW/m² (or 37.5 kW/m²) rely in the interval 250-500 m for the tears of 1 m, and 600-700 m for holes of 5 m. Using the model of Raj/TMS (2007, these distances would be 200m and 400 m, respectively;

XVI. We focus now the thermal flux of 5 kW/m². The global span for the downwind distances found by ABS and FERC with 1 m tears is from 600 m to 1,400 m, whereas for 5 m it is from 1,400 m to 2,000 m. Using the Raj/TMS (2007) model, we found an interval falling from 600 m to 1,100 m, for both thermal fluxes and tear diameters;

XVII. We conclude that it is necessary to exercise the engineering judgment for each specific situation. The results found above intend to be the contribution of the present work. We sustain that:

- Models are only a simulacrum of reality – They represent a coherent set of tools for decision-making; however, they carry intrinsic uncertainties, and must be used consistently with premises and governing assumptions and constraints. In some cases, the industry and scientific community's experience and comprehension on fundamental phenomena are more important than the scientific knowledge used to describe analytically the problem formulated;
- Models are tools to aid decision making – The main point is to use plausible information and judgment regarding a LNG facility siting. Models do not make decisions for players; they must integrate and consider all information on many different aspects of the problem to form a consistent tool basis for decisions involve human beings, environmental and assets;

XVIII. Whatever may be the modelling results found and discussed in Table 13, all the simulated distances predicted with the present work are in accordance with the intervals recommended by SNL (2004). They are powerful tools to manage the eventual hazards and impacts on external public/resources around an LNG terminal. The Sandia's Tables 15 and 16 discussed in the item (11) ahead, present recommendations for the worst case of intentional breach with large releases of LNG. These tears are supposed to cause damage to the ships and large fires with high potential of hazard to public safety. SNL (2004) predicted zones of high potential for approximately 500 m, and above 1,600 m for low potential. The model used in the present work considered ABS (2004) input data, and found similar results for, respectively, 660 m for 38 kW/m² and 1,540 m for 5 kW/m², about the same found by SNL (2004).

11. Some considerations about hazards and impacts on external public/resources

Current modelling of LNG spills and pool fires techniques have limitations. Additionally, site conditions present variations, affecting downwind predictions. Some of the factors are, to name a few, seawater waves and currents, weather conditions, obstacles in the path length of the thermal radiation propagation, land terrains. Therefore, it is helpful to provide beforehand some guidance on the wide general range for potential spills hazards, rather than suggest specific and maximum hazard guidelines.

SNL (2004) summarized results of a sensitive analysis, based on potential breaches perpetrated against LNG carriers. They considered credible accidental and intentional threats that fits and applies to the present work.

They were not for specific sites but, in lieu, they provide general approaches for hazards and potential risks. From these evaluations, SNL (2004) postulated that the thermal hazards would occur fundamentally within a range of 1,600 m centered on the tear, perpetrated on the LNG carrier moored at the terminal.

Under these circumstances, the highest risks would occur in the near field of about 250 m - 500 m around the spill point. Despite of thermal risks could exist beyond 1,600 m chances are that they are generally lower in most cases.

That general hazard assessment identified zones to be used as safety guidance, in such way that:

- The pool sizes for the credible spills estimated could range from generally 150 m in diameter for a small, accidental spill, to several hundred meters for a large one. Therefore, high thermal hazards from a fire are expected to occur within a radius of 250 m – 500 m from spill, depending on its size. Major injuries and significant structural damage are expected in this zone. The extent of the hazards will depend on the spill size, sea waves and currents even in quiescent waters, surrounding constraints, winds and the likes. Public, major commercial/industrial assets or other critical infrastructure elements (chemical plants, refineries, bridges, highways, tunnels), or national icons located within portions of this zone could be seriously damaged;
- However, hazards and thermal impacts may be attenuated to lower levels, increasing distances between the origin of the spill followed by fire. Indeed, some potential for injuries and assets damage can still occur in parts of such a zone, but this will vary based on spill size, distance from the spill/fire, and site-specific conditions. If the spill/fire is small, the hazards transition to lower levels quickly;
- Beyond approximately 750 m for small accidental spills/fires and 1,600 m for large spills, the impacts on public safety should generally be low for most potential spills. Hazards will vary, but chances are that minor injuries and minor assets damage are most likely at these distances. Increased injuries and property/asset damage would be possible if vapor dispersion occurred and a vapor cloud was not ignited until after reaching this distance. However, if a flammable cloud drifts away within its flammability level encounters an open ignition source, chances are that a flash fire may occur in unconfined venues, or else build up to an explosion/detonation, depending on the venue porosity.

Table 15 consolidates ahead the hazard levels for several types of accidental and intentional spills/fires. It considers the size and quantity of breaches. On the other hand, it does not consider parameters such as spill/burning rates, discharge coefficients, flame *SEP*s, transmissivities, and site-specific environmental conditions (wind speed, direction, sea waves/currents). Therefore, the indicated distances to each of the different hazard zones are provided for guidance only, and will vary depending on conditions and site-specific locations. The upper part of the table presents the estimated sizes of zones considering potential accidents for the public, where spills are generally much smaller. The lower part presents in the same fashion the estimated hazard zones for some examples of intentional LNG spills, usually larger.

Table 15 also presents hazards zones/downwind distances based on thermal hazards from pool fires, since them random events may start with ignition sources, generating immediate fires likely to occur. Other events may also be present with potential to generate vapor clouds with no ignition, dispersing up to 2,000 m– 2,500 m. As well, vapor clouds dispersion is highly sensitive to surrounding atmospheric conditions and to the specificity of the site.

Damaged infrastructures, presence of neighbor refineries or power plants may pose collateral threats or latent indirect effects on the facility. However, it is not usual to consider directly these last aspects. However, these issues are site-specific and should be included as part of the overall risk management process.

Table 15 - Guidance for impacts on public safety from LNG breaches and spills. Source: SNL (2004)

Event	Potential ship damage and spill	Potential hazard	Potential hazard on public safety [1]		
			High	**Medium**	**Low**
Collisions: Low speed	Minor ship damage, no spill	Minor ship damage	None	None	None
Collisions: High speed	Cargo tank breach and small-medium spill	Damage to ship and small fire	**≈ 250 m**	**≈ 250 m ≈ 750 m**	**> 750 m**
Grounding: < 3 m high object	Minor ship damage, no breach	Minor ship damage	None	None	None
Intentional breach	Intentional breach and medium to large spill	Damage to ship and large fire	**≈ 500 m**	**≈ 500 m – 1600 m**	**> 1600 m**
	Intentional breach large release of LNG	• Damage to ship and large fire • Vapor cloud dispersion with late ignition	**≈ 500 m** **≈ 500 m**	**≈ 500 m – 1,600 m** **> 1,600 m**	**> 1,600 m** **> 2,000 m**

[1] Distance to origin, varies according to site. Low – minor injuries and minor property damage; Medium – potential for injuries and property damage; High – major injuries and significant damage to property

12. General guidance on risk management for LNG operations over water

SNL (2004) proposed that the most significant impact on public and assets might occur in a range of about 500 m of a spill, with very much lower impacts beyond 1,600 m from a huge spill. Otherwise, in an unintentional collision or deliberate attack from another vessel, it is plausible to consider that 2-3 cargo tanks would be stricken. However, these conditions would not scale up the abovementioned hazard ranges but, rather, it is expected that it would increase the fire duration. Based on that approach, Table 16 compiles and summarizes SNL's recommendations and suggests some summarized guidelines on risk management for such a spills. It should be noticed that parts of texts quoted between parenthesis **( )** refer to accidental spills and between brackets **[ ]**, refer to intentional spills. Texts not quoted are considered valid to both of them.

Table 16 – Summary of suggested guidance on risk management. Source: Adapted from SNL (2011)

Topics on risk management for LNG operations on water	
Focal points →	∗ Cooperation with stakeholders, public officials ∗ Performance-based and site-specific approaches ∗ Threat assessments ∗ Safety/security operations ∗ Available resources ∗ Identify hazards/risks ∗Public safety/ property protection ∗ Risk prevention/mitigation strategies
Guidance	Assist risk management professionals, port security officials for accidental & intentional spills in: • Effective security and protection operations (interdictions, detection, risk management procedures, emergency response measures, etc. • Risk management stratifies based on site-specific conditions • High impact on public/assets with interactions with terrain/structures
(Accidental) and [intentional] spills	
Zone 1	Shipments/deliveries in narrow harbors/channels, pass under major bridges or over tunnels, or within approximately **(250 m** to people, military facilities, population, commercial centers, or national icons**)** and **[500 m** of military facilities, population, commercial centers, national icons**]**. Within this zone, the consequences of an **(**accidental**)** **[**large**]** LNG spill could be significant and have severe negative impacts. Thermal radiation poses a severe public safety and assets hazard, and damage or disrupt critical infrastructure present in this area. Risk management for LNG operations should consider the occurrence of vapor dispersion and fire hazards.

Zone 2	Shipments/deliveries in broader channels/outer harbors or within approximately **(250 m-750 m)** and **[500 m-1,600 m]** of population and commercial centers. Within this zone, the consequences of population or commercial centers. Within this zone, the consequences of an **(**accidental**)** **[**even a large**]** LNG spill are reduced and **(**risk reduction and mitigation approaches/strategies can be less extensive**)**, and **[**thermal radiation transitions to less severe hazard levels to public safety and properties**]**. In this zone risk management strategies for LNG operations should focus on approaches considering vapor dispersion/fire hazards.
Zone 3	Shipments/deliveries that occur more than approximately **(750 m) [> 1,600 m]** from major infrastructures, population and commercial centers, or in large bays or open waters, with minimum risks/consequences to public/assets of an **(**accidental**)** **[**large**]** spill over water are minimal. Thermal radiation poses minimum risks to public safety/assets. Risks reduction/mitigation strategies can be significantly less extensive. Risk management strategies should be concentrated on incident management/emergency response measures focused on vapor cloud dispersion, ensuring that individuals know how to act/do in the occurrence of an unlikely event of a vapor cloud

12.1. General conclusions of Tables 15 and 16

1. The most significant impacts to public safety and property takes place within approximately **500 m** from the center of the spill, with much lower impacts at distances beyond 1,600 m, even for very large spills;
2. Under certain conditions, it is possible that multiple LNG cargo tanks could be breached as a result of the breaching event itself, as a consequence of LNG-induced cryogenic damage to nearby tanks, or from fire-induced structural damage to the vessel;
3. We analyzed the scenarios of multiple breaches and cascading LNG cargo tank damage, as discussed in Sections 4 and 5. While possible under certain conditions, they are likely to involve no more than two to three cargo tanks at any one time. These conditions will not change substantially the hazard ranges noted in the General conclusion #1 above, but will increase expected fire duration.

13. Illustration of the magnitude of radiation impacts

13.1. Calculation march and process

In the modelling methodology presented in this document, it is assumed that the heat flux transmits in an open field, i.e., without obstacles such as hills, trees, housing, etc. Thus, the numerical results presented here apply to any LNG marine terminal under the same assumptions, since the results are independent of the surroundings of the site. To illustrate the magnitude of the distances evaluated in this report, Figures 21, 22 and 23 ahead depict hypothetical locations for mooring a hypothetical LNG carrier for loading/unloading operations. In these figures, the carrier is considered as the epicenter of a pool fire, indicated by the yellow star in the center of the circles. The concentric circles indicate the thermal influence zones for the predicted radiation levels. Figure 20 presents schematically the calculation march used in this research report.

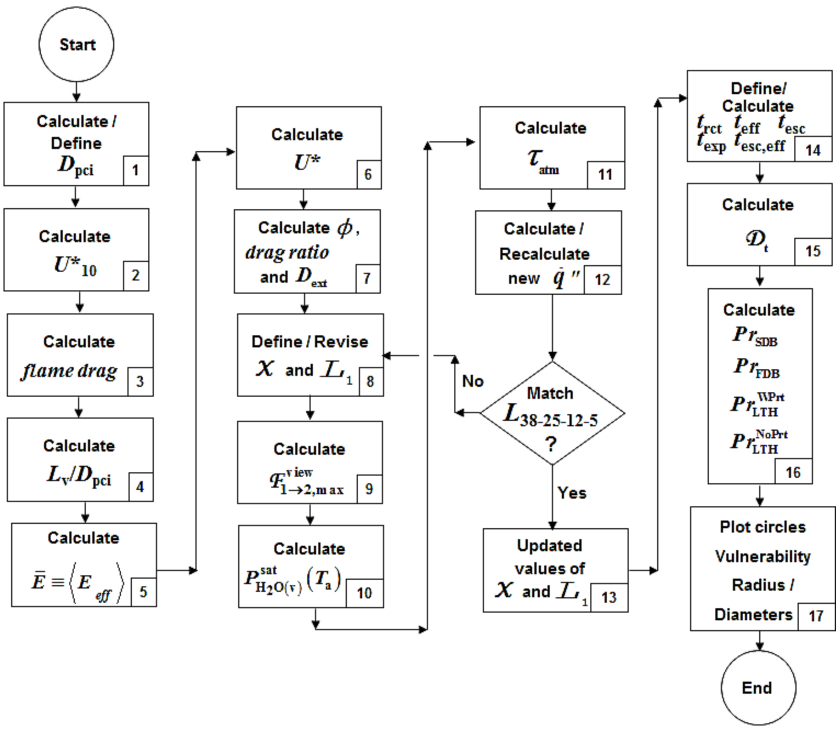

Fig. 20 – Block diagram of each step of the process calculation

Each step indicated in the bottom squares of each block corresponds to the following equations and items of this report, as presented in Table 17.

Table 17 – Summary of the process calculation

Step	Calculation Procedure	Remarks	Report Item	Equations
1	Circular pool diameter	Alternatively, the pool diameter can be defined, assuming a given value. It were considered the ABS values of 148 m and 260 m, respectively for tears of 1 m and 5 m. FERC (2004) values were also simulated in the present work	4.5 and 4.7	(22), (24) and (33)
2	Dimensionless wind velocity at 10 m above the ground	None	5.6	(53)
3	Flame drag	The fire column was supposed to be inclined by the wind action	5.8	(59a)
4	Pool fire geometry – L_V/D_{pci}	None	5.7	(56)
5	Time average surface emissive power of the fire column	None	6.1	(75)
6	Dimensionless wind velocity	Plume at ground level	5.7	(56)
7	Flame tilt, drag ratio and extended diameter (flame drag)	None	5.9; 5.8	(61), (63), (60), (59b), (59a)
8	Distances between the pool fire center and the center of the target, and where the thermal radiation flux received by a resource is equal to 1 kW/m²	Trial and error interactions	6.5	None
9	View factor between the flame column and the target at ground level	Using Green's and Stokes' theorems	6.4; 6.5	(84), (94)
10	Local saturated vapor pressure of the air	AIChE (2000) equation	6.5.2	(95)
11	Local air transmissivity	AIChE (2000) equation	6.5.2	(96)
12	Thermal radiation fluxes	Match the prescribed values of 38, 25, 12 and 5 kW/m²	6.5.3	(85)
13	Update values of the step 11	Until the thermal fluxes match the prescribed values of step 12	6.5.3	(85)
14	Reaction, effective, escape, exposure and effective-escape times	Set 5 seconds for the reaction time and 4 m/s for the escape velocity	7.3	(107), (108), (109), (113)
15	Thermal doses	Sum of reaction dose and time average of escape doses	7.3	(110), (111), (112), (113)
16	Probit values and the correspondent percentages of the resources impacted	First and second degree, lethality with and without protection	7.2	(101), (102), (103), (104)
17	Vulnerability of the resources impacted	Plot on satellite photos or other data base	13	None

13.2 Results and findings plotted on satellite photos

The circles in Figures 21 through 23 indicate the influence zones of the different estimated thermal radiation levels, which radius are plotted on the Google Maps© satellite photos (in both tear diameters of 5 m and 1 m) with the same map scale to keep scale consistency. They were compiled from the data basis property of Google Earth Copyright© 2017 and Google Maps with Map data copyright ©2017 Google Imagery ©2017, from CNES / Astrium, Cnes/Sport Image, DigitalGlobe Terms. Satellite photos presented in Figs. 21, 22 and 23 of this report are used for Scientific Research purposes only, without any commercial objective thereof. Figures 20 and 21 show satellite images captured on April 4, 2017, with scale of 1,000 ft = 300 m (on the map) ≡ 2 cm (on the figures). 24.1/17.9 (too many TM abbreviations)

Each concentric circle of these Figures (21, 22 and 23) applies to each one of predictions of injuries/damages discussed ahead. We considered only the hypothesis of lethality with protection for the realistic/worst case. First and second degrees, as well as lethality burns with protection, may be also expected to occur and one can determine it in the same fashion, but they are not plotted on those figures.

From the three pictures one can conclude that for the tears either of 5 m or 1 m here considered, the inland public, proprieties and assets are far too distant (about 4.2 km in Guanabara and 3.6 km in Paranaguá Bays) from the center of the pool fire. They are 'relatively safe' to outcomes that may occur on the terminals. However, for the operation personnel working within the battery limits of those fictitious facilities, there might be serious concerns about lethality, even with appropriate cloth protection.

The worst case scenario predicted for the larger tear (5 m), with the shortest distance of 660 m away from center of the fire column, led to predict an effective escape time of 97 s (sec) (about 1.5 minute), but receiving a lethal dose of 38 kW/m² with death probability of around 100%. On the other hand, if the personnel can evacuate the site within 164 seconds (about 3.5 minutes), they can have a chance up to 47.5% to be exposed to a level of 5 kW/m² at 1,540 m (about 1.5 km) away from the epicenter. With this worst scenario, the inland public/assets remain 'relatively safe' to the thermal radiation fields. The situation is even more favorable with the tear of 1 m, as illustrated ahead in Fig. 22.

The location of this fictitious terminal is quite peculiar. For the purpose of this work, we chose to locate this facility in the middle of a bay, surrounded by heavy population density, and oil/gas facilities such as refineries, terminals, and sub-sea oil and gas pipelines. The bay supports heavy maritime ship traffic having besides, shipyards, Naval and Marine Corps Military Basis, with constant commercial traffic and military maneuvers. Marine and Coast Guard Authorities develop constant surveillance on this waterway.

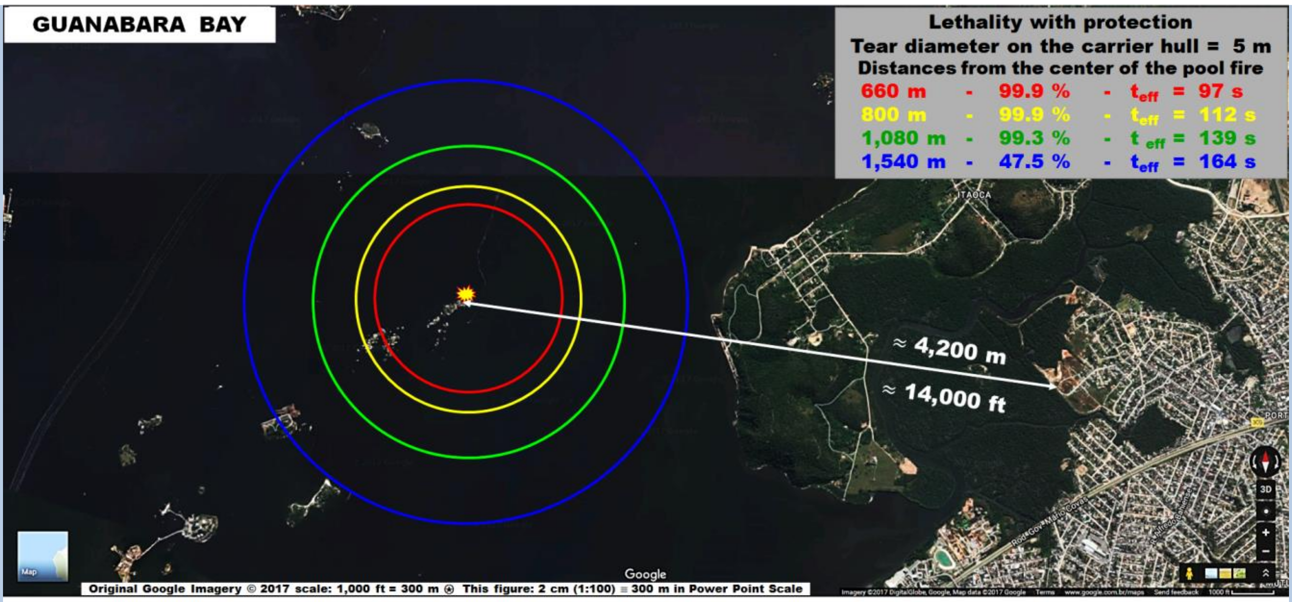

Fig. 21 – An island in the Guanabara Bay with a hypothetical LNG carrier moored in a **hypothetical** loading/offloading location. Tear diameter of 5 m. Available in: https://www.google.com/maps/@-22.76199,-43.10074,10z/data=!3m1!e3-Google Maps. Courtesy of Google Earth Copyright© 2017 and Google Maps. Access: April 14, 2017.

Similar results can be achieved with a tear of 1 m, **as depicted in the Figure 22**. The on land public/assets can be considered as '**not stricken**' by the thermal radiation fields. Similarly, the best situation **between Figures 20 and 21** for the operation personnel is such where the effective escape time is 86 seconds (1.5 minute) with a level of 5 kW/m² at 800 m away from the epicenter.

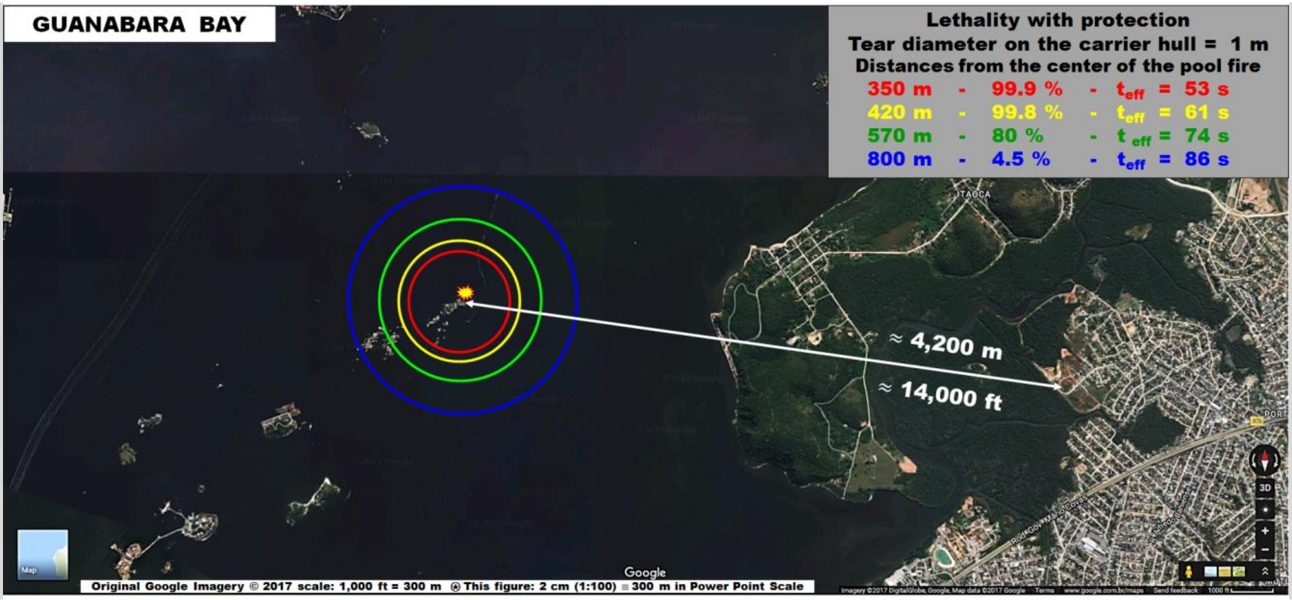

Fig. 22 – **An island in the** Guanabara Bay with a hypothetical LNG carrier moored in a **hypothetical** loading/offloading operation. Tear diameter of 1 m. Available in: https://www.google.com/maps/@-22.76199,-43.10074,10z/data=!3m1!e3-Google Maps. **Courtesy of Google Earth Copyright© 2017 and Google Maps. Access: April 14, 2017.**

Analogously, Figure **23** depicts the site **where** a LNG carrier supposedly could moor for a loading/offloading operation**. As in** Guanabara Bay, this terminal has the influence radius plotted on the Google Maps® satellite photos with the most critical diameter (5 m) with the same map scale to keep scale consistency with what has been compiled from Google Earth®. 36.0/15.5**Figure 23 shows a satellite photo of the Paranagua Bay** captured on **April 19, 2017** from Imagery© Digital Globe. Google, Map data© 2017 Google Terms www.google.com.br/maps, with a scale of **1,000 m = 2.5 cm (on the map)**.

The **port** facilities of **the Paranagua Bay presented in the bottom of this figure, are situated about 25-30 Km west of the Bay entry. An island inside of this water body, distant about 3,600 m west from the port is supposed to accommodate a terminal. A hypothetical scenario of pool fire takes place during the mooring of a LNG carrier when loading/unloading this cryogenic.** Notice that surrounding scenario of this waterway is different from the Guanabara Bay case. **Although this bay may have port facilities with less density of oil/gas facilities and public, the environment seems to be relatively intact in the north direction.**

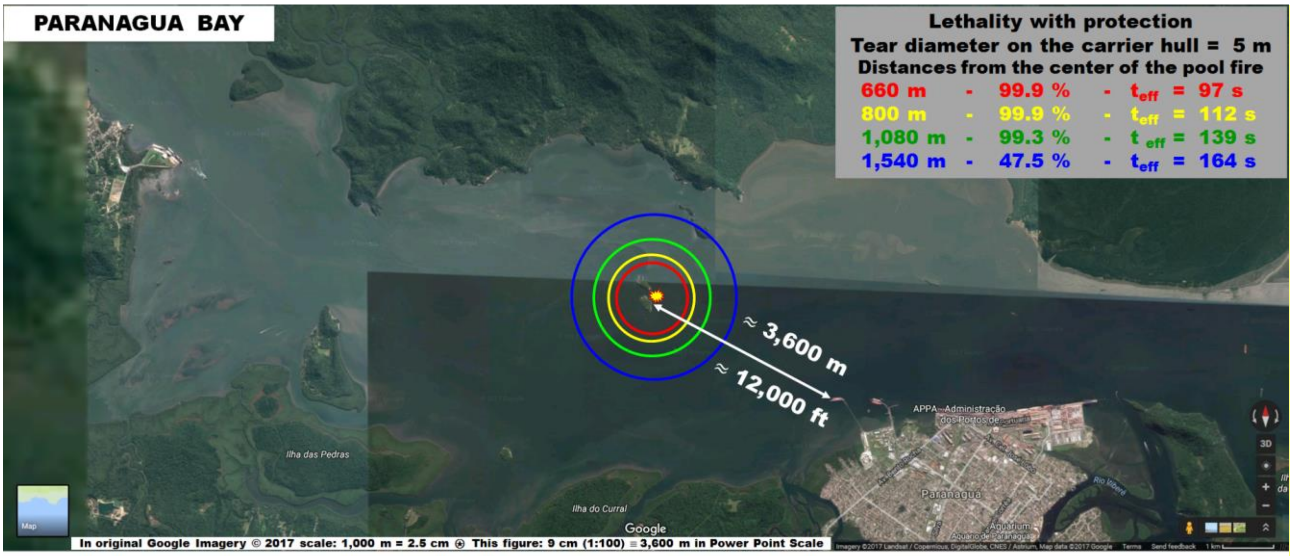

Fig. 23 – **An island in the** Paranagua Bay with a **hypothetical** LNG carrier moored in a loading/offloading operation. Tear diameter of 5 m. Available in: https://www.google.com/maps/@-22.76199,-43.10074,10z/data=!3m1!e3-Google Maps.
Courtesy of Google Earth Copyright© 2017 and Google Maps. Access: April 19, 2017.

As illustrated in Figures 21 through 23, the inland public/assets may be considered as 'not stricken' by the thermal radiation fields. Similarly, the best situation for the operation personnel is such where the effective escape time is 164 seconds (approx. 3 min) with a level of 5 kW/m² at 1,540 m away from the pool fire epicenter, even with a pool fire of 5 m tear.

An important conclusion that can be withdrawn from Figures 21 through 23 is that all of them present similar profiles. With this evidence, one may infer that the probit analysis is independent of environment and scenarios. In other words, it could be considered as 'non-site' specific.

Acknowledgements

PUC-Rio thanks The National Research Council (CNPq) and The Foundation for Research of the State of Rio de Janeiro (FAPERJ) for financial support.

PUC-Rio also acknowledges Dr. Henrique Paula (ABS Group) for his enlightening comments, suggestions and counseling.

PUC-Rio is in debt with Mr. Antonio Cordovil (Chemical Engineering Department of PUC-Rio) for the complete revision of all computer code equations. His effort to reprogram and implement the present modelling, was fundamental to finalize this research report.

The team job thanks Mr. Pedro Araujo (Mechanical Engineering Department of PUC-Rio), for his suggestions and innovative ideas to improve the present work.

Thanks are equally dedicated to Google Earth Pro/Maps Copyright© for the use, as courtesy, in the present scientific research effort of their images and photos.

Disclaimer Notice

List of acronyms

ABS	American Bureau of Shipping
AGA	American Gas Association
AIChE	American Institute of Chemical Engineers
BS	British Standards
CFR	Code of Federal Regulation
EES®	Engineering Equation Solver, developed by the Department of Mechanical Engineering of the University of Wisconsin-Madison, USA
Excel®	Microsoft Advanced Excel Spreadsheet developed by Microsoft for the Windows Platform
FEMA	Federal Emergency Management Agency
FERC	Federal Energy Regulatory Commission
EN	European Normalization
HSE	Health and Safety Executive
IMO	International Maritime Organization
JP	Jet propellant fuel
LPG	Liquefied Petroleum Gas
LNGFIRE®	Thermal radiation model for LNG fires, developed by the Gas Research Institute, 1990
MARAD	United States Maritime Administration
Mathtype 6.9®	Interactive equation editor for Windows, developed by Design Science, Inc. Company Information
MIT	Massachusetts Institute of Technology
MKOPSC	Mary Kay O'Connor Process Safety Center
NFPA	National Fire Protection Association
RPT	Rapid Phase Transition
SEP	Surface Emissive Power
SFPE	Society of Fire Protection Engineering
SIGTTO	Society of International Gas Tanker and Terminal Operators
SNL	Sandia National Laboratories
TMS	Technical & Management Systems
TNO	Technical Netherlands Organization
USDOT	United States Department of Transportation
USCG	United States Coast Guard

WHAZAN	World Bank Hazard Analysis

List of symbols – Romans

A_{h}	Tear area on the carrier hull (m²)
$A_{\mathrm{h_{cr}}}$	Critical tear area on the carrier hull (m²)
A_{i}	Area of ith element of the solid flame surface (m²)
A_{j}	Area of jth element of the solid flame surface (m²)
$A_{\mathscr{L}}$	Soot extinction specific area (m²/kg)
$A_{\mathrm{h\,cr}}$	Critical value of the tear diameter (m²)
$A_{\mathrm{p\,ci}}$	Area of the circular pool formed alongside the carrier hull, centered on the tear center (m²)
$A_{\mathrm{p_{sc}}}$	Area of the semicircular pool formed alongside the carrier hull, centered on the tear center (m²)
$A_{\mathrm{p_{sc}}}^{\mathrm{max}}$	Maximum area of the semicircular pool (m²)
$A_{\mathrm{p_{sc,cr}}}^{\mathrm{max}}$	Critical value of the maximum area of the semicircular pool (m²)
$A_{\mathrm{p_{sc,lb}}}^{\mathrm{max}}$	Lower bound limit of the maximum area of the semicircular pool (m²)
$A_{\mathrm{p_{sc,ub}}}^{max}$	Upper bound limit of the maximum area of the semicircular pool (m²)
A_{t}	Area of the constant cross section of the carrier cargo tank (m²)
a_{i}	Acceleration of the material particle in the direction i (m/s²)
$a^{*,\mathrm{max}}$	Maximum dimensionless area of the semicircular pool (-)
c_{p}	Specific heat capacity at constant pressure (J/kg.K)
$c_{\mathrm{p_a}}$	Specific heat of the air at constant pressure (assuming the same for all gases) (J/kg.K)
C	Continuous curve defined by functions $P(x,y,z)$, $Q(x,y,z)$, $R(x,y,z)$; the chemical element Carbon (-)
C_{d}	Orifice coefficient (-)
C_{i}	Contour curve for a given area i, A_{i} (-)
C_{j}	Contour curve for a given area j, A_{j} (-)
C_{s}	Concentration of soot particles within of a fire column (kg/m³)
CTV	Cargo tank volume (m³)
CVC	Cargo vessel capacity (m³)
c	Molar concentration (mol/m³)
c_1	Constant with value 1.26 E (+8), used in the Eq. (78) (-)
c_2	Constant with value 25,000, when the value of $\dot{q}''$ (Btu/h.ft²), and T (R) (Kern, 1999), used in the Eq. (78) (-)
$\mathcal{C}$	Thermal, overpressure or toxic concentration that must be integrated during all exposure time (kW/m², kPa, kg/m³)
$D = D_{\mathrm{p_{ci}}}^{\mathrm{eq}}$	Average diameter equivalent to the diameter of a circular pool (m)
Da	Damkhöler number (-)
$D_{\mathrm{p\,ci}}$	Diameter of a circular pool (m)
$\langle D_{\mathrm{p\,ci}} \rangle$	Average value of the diameter of the circular pool taken with several values (m)

$D_{\mathrm{p_{ci,ub}}}$	Upper bound value of the diameter of a circular pool (m)
$D_{\mathrm{p_{sc}}}$	Diameter of a semicircular pool (m)
$D_{\mathrm{p_{sc,ub}}}$	Upper bound value of the diameter of a semicircular pool (m)
$D_{\mathrm{p_{sc,cr}}}$	Critical value of the diameter of a semicircular pool (m)
D_{h}	Tear diameter perpetrated on the carrier hull (-)
$D_{\mathrm{h_{cr}}}$	Critical value of the tear diameter perpetrated on the carrier hull (-)
D_{ext}	$= Flame\ Drag$ or extended diameter of the pool fire (m)
$Drag\ ratio =$	Drag ratio, or the ratio between the pool with extended diameter due to the wind action, and the diameter with windless condition, $D_{\mathrm{ext}}/D_{\mathrm{p_{ci}}}$ (-)
D/Dt	Material derivative following the flow movement (-)
DR	Draft; the vvertical distance between the waterline and the bottom of the carrier's hull (keel) (m)
$\mathfrak{D}$	Molecular mass diffusivity of the gas mixture where the flame and the combustion flow takes place (m²/s)
$\mathfrak{D}_{\mathrm{i}}$	Molecular mass diffusivities, of all chemical elements (m²/s)
$\mathfrak{D}_{\mathrm{ij}}$	Coefficients of multi-species diffusion of the mixture; molecular mass diffusivity of the species i in species j in a mixture where the flame and the combustion flow takes place (m²/s)
$\mathfrak{D}_{\mathrm{i}}^{\mathcal{M}}$	Diffusion coefficient for species i into the mixture $\mathcal{M}$ of other species (kg/m².sec)
$\mathfrak{D}_{\mathrm{i}}^{\mathrm{T}}$	Thermal diffusivity of the species i based on the temperature gradient $\partial T/\partial z$ (kg/m.s)
$\mathcal{D}$	Dose of thermal radiation, overpressure or concentration received by a vulnerable resource [s.kW$^{4/3}$, s.kPa$^{4/3}$, s.(kg/m³)$^{4/3}$]
$\mathcal{D}_{\mathrm{t}}$	Dose of the received thermal radiation (s.kW$^{4/3}$)
$\bar{\mathcal{D}}_{\mathrm{esc}}$	Dose received during the escape time (s.kW$^{4/3}$)
$\mathcal{D}_{\mathrm{rct}}$	Dose received during the reaction time (s.kW$^{4/3}$)
dA_{i}	Area element i of the external surface of the fire column (m²)
dA_{j}	Area element j of the external surface of the fire column (m²)
E	Emissive power along the fire plume, equivalent to a blackbody, used by Mudan (1984) and Shokri and Beyler (1989), (kW)
$\mathcal{E}$	Quantity of different chemical elements in the mixture (-)
$\bar{E} \equiv \langle E_{\mathrm{eff}} \rangle$	Average *SEP* (Surface Emissive Power*)* taken along the length (height) of the visible fire plume (kW/m²); time average surface emissive power (kW/m²)
E^{max}	Maximum emissive power taken on the fire base, equivalent to a body with temperature equivalent of a blackbody (kW/m²); Maximum emissive power used by Mudan (1984) (kW)
E_{s}	Effective radiation (attenuation) emitted by the cylindrical external surface of the fire plume, obscured by the smoke (kW/m²)
E_{smk}	Smoke emissive power, used by Mudan (1984) (kW)
E_0	Nominal surface emissive power (*SEP*) of the fire column, close to the fire base (kW/m²)
$\bar{E}_{\lambda_{\mathrm{i}}}(\lambda)$	Time average spectral radiance (or emittance) or Surface Emissive Power (SEP), dependent of the radiation wave, emitted by the i$^{\mathrm{th}}$ area element of the external de area of the fire plume (kW/m².µm)
$\langle E_{\mathrm{eff}} \rangle$	Average emissive power of a solid fire column, determined by the adjustment of several values measured with experiments related in the open literature, for the radiant heat striking over external targets (kW/m²)
$\hat{\mathbf{e}}_{\mathrm{i,j,k}}$	Dyadic unit of the Cartesian basis of a vector in the directions i, j, k (-)

$Fr_{\mathbb{C}}$	Combustion Froude number (-)
$Fr_{\mathbb{C},10}$	Combustion Froude number with wind velocity measured at the height of 10 m above the fire base (-)
$\mathcal{F}$	Generic view factor (-)
$\mathcal{F}_{dA_i \to A_j}^{\text{view}}$	View factor between the element of area dA_i of the external surface of the fire and the area of the object (target), $\mathcal{A}_j$ (-)
$\mathcal{F}_{A_i \to A_j}^{\text{view}}$	View factor between the area A_i of the external surface of the fire and the area of the target, $\mathcal{A}_j$ (-)
$\mathcal{F}_{1\to 2}^{\text{view}}$	View factor between the emitter (1) and the receiver (2) (-)
$\mathcal{F}_{1\to 2,\max}^{\text{view}}$	Maximum view factor, as the resultant of the vector sum of $\mathcal{F}_{1\to 2,\text{horz}}^{\text{view}}$ with $\mathcal{F}_{1\to 2,\text{vert}}^{\text{view}}$.(-)
$\mathcal{F}_{1\to 2,\text{horz}}^{\text{view}}$	Maximum view factor of the horizontal component (-)
$\mathcal{F}_{1\to 2,\text{vert}}^{\text{view}}$	Maximum view factor of the vertical component (-)
$\pi\mathcal{F}_{\text{vert}}^{\text{view}}$	Vertical component of the configuration (view) factor (-)
$\pi\mathcal{F}_{\text{horz}}^{\text{view}}$	Horizontal component of the configuration (view) factor (-)
f_i	Resultant of the body forces acting on the fluid material particle in the pool in the direction i (N)
$g = \lvert\mathbf{g}\rvert$	Module of the vector of gravitational field (m/s²)
$H = L_{\mathbb{V}}$	Height (length) of the visible thermal plume (m)
h	A given height of LNG inside the cargo tank (m). Specific enthalpy (J/kg)
h_0	Initial height of the LNG inside the cargo tank measured above the hole of the tear on the carrier's hull (m)
$h(t)$	Height of the LNG inside the cargo tank, as a function of the time (m)
h_{ox}	Oxidizer specific enthalpy (J/kg)
h_{CV}	Coefficient of convection heat transfer (J/s.m².K)
h_v	Specific enthalpy of the vapor fuel (J/kg)
$\mathbf{j}_i$	Vector of the mass diffusion of the chemical species i per unit of time (kg/m².s)
$\mathbf{J}_i$	Vector field of the mass diffusion flux of the species i in a mixture of $\mathcal{M}$ species (kg/m².s)
k	Thermal conductivity (J/s.m.K; kW/m.K))
$\mathcal{K}$	Isothermal compressibility factor (Pa $^{-1}$)
k_{mix}	Mixture thermal conductivity (J/s.m.K; kW/m.K))
$\mathcal{L}$	Alternatively $\mathcal{L}_{\text{pathlength}}$, distance through the atmosphere, from the outside border surface of the fire plume to the center of the target (Fig. 11) (m)
$\mathcal{L}_1$	Distance from the center of the fire column where the thermal radiation flux received by a resource is equal to 1 kW/m², as defined by TNO (1992)
L_{beam}	Length of the optical beam for cylindrical fires, adopted by Raj (2007a,b) (m)
L_{38}, L_{25}	Downwind distance to 38 kW/m², 25 kW/ m^2
L_{12}, L_5	Downwind distance to 12kW/m², 5 kW/ m^2
$L_{\mathbb{C}}$	Length (height) of the lower part (bottom) of the "clean" combustion zone of the fire plume (m)
Le	Lewis number (-)

$L_{\mathbb{I}}$	Length (height) of the "intermittent" zone of the fire plume (m)
$L_{\mathbb{V}}$	Average length (height) of the "visible" fire plume (m)
$\mathscr{L}_{\lambda}$	Extinction coefficient (inverse of the spectral optical thickness) (m^{-1})
l_i, m_i, n_i	Director cosines of dA_i (-)
l_j, m_j, n_j	Director cosines of dA_j (-)
$\dot{M}$	Mass flow rate (kg/s)
$\mathcal{M}_i$	Molar mass of the chemical species i (kg)
$\mathcal{M}_j$	Molar mass of the chemical species j (kg)
$\dot{m}''_b$	Mass flow rate of the fuel burned in the fire plume per unit of area of the pool ($kg/m^2.s$)
$\dot{m}''_d(t)$	Mass flow rate of the spillage of LNG onto the sea with the cargo tank at full capacity (kg/s)
$\dot{m}''_{d,o}$	Initial mass flow rate of the spillage when the height of LNG inside the cargo tank is $h(t) = h_o$ (m)
$\dot{m}''_r$	Mass flow rate of radiation of the fuel burned in the fire plume per unit of area of the pool ($kg/m^2.s$)
$\dot{m}''_v$	Burning rate of the fuel vaporization of the fuel in the fire plume per unit of area of the pool ($kg/m^2.s$)
N	"N^{th}" element of external surface of the solid flame (-)
NT	Quantity of the carrier cargo tanks (-)
$\mathcal{N}$	Power applied to the concentration $\mathcal{C}$ to define the total dose $\mathcal{D}_t$ received by a given resource (-)
$\hat{\mathbf{n}}$	Dyadic vector, the basis of the tridimensional Cartesian space; Normal vector to the flame surface based on the gradient $\mathscr{r}$ of the progress of the combustion chemical reaction (m)
$\hat{\mathbf{n}}_i$	Normal vector to the surface A_i (m)
$\hat{\mathbf{n}}_j$	Normal vector to the surface A_j (m)
$\{\nabla\hat{\mathbf{n}}\}$	Tensor of the normal gradient of the flame surface (m)
$\mathfrak{n}$	Adjustment power of a polynomial function (-)
O	Chemical element oxygen (-)
P	Pressure (N/m^2)
P_a	Local ambient pressure (kPa)
$P^{sat}_{H_2O(v)}(T_a)$	Saturated water vapor pressure at a given atmospheric temperature (N/m^2)
Pr	Probit random variable (-)
Pr_{FDB}	Probit number for first degree burns (-)
Pr_{SDB}	Probit number for second degree burns (-)
Pr^{WPrt}_{LTH}	Probit number for lethality with protection clothes (-)
Pr^{NoPrt}_{LTH}	Probit number for lethality with no protection clothes (-)
$p(\xi)$	Probability expressed as the fraction of the time that the outer layers of the cylindrical fire show the 'inner core' thus radiating at the maximum surface emissive power (SEP), and the remainder of the time the emission is from the smoke layers (-)
$\dot{Q}'''$	Rate of the energy stored or released per unit of volume ($J/s.m^3$)
$\mathcal{Q}$	Quantity of different chemical species in the mixture (-)
$\dot{Q}$	Radiant energy rate emitted by the thermal plume (kW)

$\mathbf{q}_C$	Vector field of the heat flux transferred by conduction per unit of time (J/m².s)
$\mathbf{q}_R$	Vector field of the heat flux transferred by radiation per unit of time (J/m².s)
$\dot{q}''$	Flux of monochromatic heat per unit of time received at a given distance from the thermal plume (kJ/m².s; kW/m²)
$\overline{\mathbf{q}_i''}$	Reynolds time average of Favre fluctuation of the transported quantity of the species i (mol, kg)
$\{\nabla\tilde{\mathbf{q}}_i\}$	Second order tensor of the gradient transport of the Favre's average of the species i (mol, kg)
R_p	Radius of the semicircular pool (m)
$R(\%)$	Probability or Response, expressed in percentage of the vulnerable resource stricken by the dose emitted (%)
R	Distance (m)
$R_{p\,ci}$	Radius of the circular pool (m)
$R_{p_{sc}}$	Radius of the semicircular pool (m)
Re_{10}	Reynolds number calculated at 10 m above the fire plume base (-)
RH	Relative humidity (%)
$\Re$	Ratio between the mass of the stoichiometric air of mixture to the mass of vapor fuel (methane) $= 17.17$ (-)
$\lvert\mathbf{r}\rvert$	Module vector of the radial particle position particle (m)
r	Radial position of a material particle within the film of a semicircular pool; Radius or position of a volume element in the solid fire column; Distance from the carrier hull to the edge of the semicircular pool (m)
r_i	Space position of the area element dA_i (m)
r_j	Space position of the area element dA_j (m)
r	Progress of the chemical combustion reaction (kg/m)
$[\nabla r]$	Gradient of the progress of the combustion chemical reaction (kg/m)
S	Distance between points of the curves C_i and C_j (m)
SEP	Surface emissive power (kW/m²)
s	Flame extinction coefficient in the Mudan's correlation (m^{-1})
$\mathbf{s}_i$	Vector of a given point of the contour curve C_i (m)
$d\mathbf{s}_i$	Element of the vector $\mathbf{s}_i$ at a given point of the dA_i surface (m)
$\mathbf{s}_j$	Vector of a given point of the contour curve C_j (-)
$d\mathbf{s}_j$	Element of the vector $\mathbf{s}_j$ at a given point of the dA_j surface (m)
S_{ij}	Distance between the centers of the area elements dA_i and dA_j (m)
T	Temperature; temperature of the emitter flame (K)
T_a	Dry bulb temperature of the atmospheric air (K); in accordance to TMS (2006) (Page 40 of 99, Figure 3.4), limited in the interval - 33 °C and 100 °C
T_{ad}	Adiabatic temperature of the flame surface (K)
T_b	Temperature of the normal boiling point (K);
$T_{\mathbb{F}}$	Temperature of the exterior flame surface (K)
T_{ij}	Tensor of the surface tensions acting on the fluid material particle (N/m²)
T_w	Local temperature of the seawater (K)
t	Time (s)
t_{chem}	Chemical reaction time scale of diffusion flames (s)

t_{d}	Discharge time (spillage time of the LNG volume onto the sea; spillage duration) (min; s)
t_{diff}	Diffusion time scale of diffusion flames (min; s)
t_{eff}	Effective exposure duration (time), determined in accordance with methods cited by TNO (1992, *et seq.*) (s)
$t_{\mathrm{eff,esc}}$	Eeffective exposure duration during the escape from a pool fire, determined in accordance with methods cited by TNO (1992, *et seq.*) (s)
t_{esc}	Escape time for an individual to seek for a safe place (shelter) (s)
t_{exp}	Exposure time to thermal radiation (s)
Tilt angle	Flame inclination in relation to the vertical (-)
t_{rct}	Reaction time, by considered as 5 s by ioMosaic (2005) and TNO (1992)
$t_{\mathcal{I}_1}$	Time spent to thermal radiation reach 1 kW/m² (s)
t_{v}	Vaporization time of the pool (fire duration) (min)
$\langle t_{\mathrm{v}} \rangle$	Average vaporization time taken with several values (min)
t_{v}^{*}	Dimensionless time required to vaporize the pool spilled onto the sea (-)
$t_{\mathrm{v_{cr}}}$	Critical value of the vaporization time (s)
$t_{\mathrm{v_{lb}}}$	Lower bound vaporization time (s)
U^{*}	Dimensionless local wind velocity (-)
U_{10}^{*}	Dimensionless local wind velocity, measured at 10 m above the fire base column (-)
U_{wind}	Local wind velocity (m/s)
$U_{\mathrm{wind,10}}$	Local wind velocity measured at 10 m above the fire column base (m/s)
$U_{1,6}^{*}$	Dimensionless local wind velocity, measured at 1.6 m above the fire base column (-)
$\{\nabla \mathbf{u}\}$	Symmetric second order tensor of the velocity field gradient (m/s)
$\{\nabla \mathbf{u}\}^{\top}$	Second order transposed tensor of the velocity field gradient (m/s)
$\mathbf{u}$	Velocity vector field; Vector of the average velocity of the flow mass center (m/s)
$\mathbf{u}_{\mathrm{i}}$	Velocity vector field of the species i diffusion (m/s)
$\overline{\mathbf{u}''}$	Reynolds time average of the Favre fluctuation (by the density) average of the velocity vector field (m/s)
u	Module of the velocity field $\lvert \mathbf{u} \rvert$ (m/s); Independent integration variable (-)
$u_{\mathrm{i,j,k}}$	Velocities field of the fluid material particle in the direction i, j, k (m/s)
u_{esc}	Scape (run) velocity from the fire site (m/s)
$V_{(\mathrm{m})}(t)$	Volume (m³) of a fluid material particle of the fluid at a given time *t* (s)
V_{F}	Total volume of the solid flame (m³)
V_{p}	Volume of the cryogenic liquid in the pool (m³)
V_0	Initial LNG volume in the full cargo tank spilled onto the sea, or within the carrier cargo tank (m³)
v	Specific volume (m³/kg)
$\boldsymbol{v}$	Vorticity vector (1/s)
$v_{\mathrm{i,j,k}}$	Cartesian coordinates of the vorticity vector (1/s)
w_{i}	Mass fraction of the chemical species i $(-)$

w_j	Mass fraction of the chemical species j $(-)$
$w_i(\xi)$	Mass fraction of the chemical species i as a function of the passive scalar $(-)$
$w_{prod}(\xi)$	Mass fraction of the combustion products as a function of the passive scalar $(-)$
X	Distance between the pool fire center and the center of the target (m)
X_0	Distance where an individual is located (from the center of the pool fire) when he starts to escape from the pool fire (m)
x	Generic distance (m)
x, y, z	Cartesian coordinates (m)
$x_{i,j,k}$	Cartesian coordinate in the direction i, j, k (m)
$\mathcal{X}_i$	Mole fraction of the species i (-)
$\mathcal{X}_j$	Mole fraction of the species j (-)
$x_{i_{\mathbb{F}}}$	A given position of the flame surface (m)
$\langle \dot{y} \rangle$	Average vaporization velocity (m/s) of the pool in quiescent waters (m/s)
Y	Soot mass yield per unit mass of fuel burned Smoke (soot) yield (%)
Z	Length alongside the axis of the fire column (m)
$\mathcal{Z}_i$	Element mass fraction of the chemical element i (-)
$z_{i_{\mathbb{F}}}$	Coordinate of a given point of the flame surface (m)

List of symbols – Greeks

α	Thermal diffusivity (m²/s)
α, β, γ	Director cosines (rad)
ß	Dimensionless empirical constant in axisymmetric pool spreading (-)
β^*	Coefficient of thermal expansion (K^{-1})
Υ	Dimensionless flow parameter governing the regime of the LNG pool spillage on the sea of quiescent waters (-)
Υ_{cr}	Critical value of dimensionless flow parameter which governs the flow transit from the gravity-inertia regime to the gravity-viscous regime (-)
Δ	Ratio of the local difference between the density of the sea water and of LNG to the density of the sea water (-)
$\Delta H_{\mathbb{C}_L}$	Lower specific heat of combustion of the liquid fuel (J/kg.K)
$\Delta H_{\mathbb{V}_L}$	Vaporization heat of the liquid fuel (J/kg K)
$\hat{\boldsymbol{\delta}}_{ij}$	Second order tensor of the Kröenecker's delta (-)
$\overline{\delta}$	Time average thickness the pool (m)
$\overline{\overline{\overline{\boldsymbol{\varepsilon}}}}$	Third order tensor of the permutation (-)
$\{\varepsilon_{i,j,k}\}$	Third order tensor of the permutation in Cartesian coordinates (-)
$\overline{\varepsilon}$	Total hemispheric time average emissivity of the fire plume (wavelength independent) (-)
η	Fraction of the air mass which is mixed up to a given length alongside the fire plume axis, Z, and is burned within the fire plume with its stoichiometric mass of fuel, or burning efficiency of the fuel (-)
θ	Conic solid angle between the emitting external surface of the fire plume and the target where the thermal radiation is incident (spherical radian)
θ_i	Conic solid angle between the unit vector $\hat{\mathbf{n}}_i$ normal to the element dA_i and the line that connects dA_i to dA_j (spherical radian)

θ_j	Conic solid angle between the unit vector $\hat{\mathbf{n}}_j$ normal to the element dA_j and the line that connects dA_i to dA_j (spherical radian)
κ_1, κ_2	Constants of 'Probit' Equations, determined empirically based in past accidents of fires, explosions, dispersions, etc. (-)
κ_λ	Spectral optical thickness (physically equivalent to the optical path length) (m)
λ	Global viscosity of a Newtonian fluid (kg/m.s)
λ	Spectral wavelength of the thermal radiation (µm)
μ	Dynamic viscosity of a Newtonian fluid (kg/s.m)
μ_a	Dynamic viscosity of the air (kg/s.m)
μ_{ij}	Mass proportion of chemical element i in the species j
μ_T	Dynamic viscosity of a turbulent flow (kg/m.s)
ξ	Mixture fraction or the 'passive scalar' (-)
ξ	Fraction of the visible flame to the total of the of the thermal plume length (height) (-)
ρ	Density of cryogenic fluid in the pool; Total density of a chemical mixture (kg/m³)
$\bar{\rho}$	Reynolds' time average of the density of the chemical mixture (kg/m³)
ρ_a	Density of the local atmospheric air (kg/m³)
ρ_i	Partial density of the chemical species i (kg/m³)
ρ_l	Density of the LNG (kg/m³)
ρ_v	Density of the GNL vapor (kg/m³)
ρ_W	Density of the local seawater (kg/m³)
$\bar{\bar{\boldsymbol{\sigma}}}$	Second order tensor of the net stretching rate of the flame (m)
σ	Stefan-Boltzmann constant, 5.670367 × 10^{-8} W/(m².K^4)
$\tau_\lambda(\lambda)$	Spectral hemispheric transmissivity dependent of λ of the local atmosphere between the area element dA_i and the area A_{obj} of the receiving object j (-)
τ_{atm}	Spectral hemispheric transmissivity of the local atmosphere (-)
τ_s	Total hemispheric transmissivity of the smoke (soot) (-)
υ	Kinematic viscosity (m²/s)
υ_a	Air kinematic viscosity (m²/s)
Γ_j	Arbitrary contour curve to formulate the line integration for a given area A_j (-)
Φ	Rayleigh function of mechanical viscous dissipation (m²/s³))
ϕ	Flame tilt angle relative to the vertical (rad; degree)
ψ	Ratio between the length of the 'clean' combustion zone to the length of the visible plume taken alongside the axis of the fire plume, $L_{\mathbb{C}} / L_{\mathbb{V}}$ (-)
$\bar{\bar{\Omega}}$	Or Ω_{ij}, vorticity second order antisymmetric tensor (N/m²)
$\boldsymbol{\omega}$	Angular velocity vector (rad/s)
$\dot{\omega}_i$	Molar formation rate of the chemical species i (kg/m³.s)
ω_{x_1,x_2,x_3}	Components of the axles x_1, x_2 and x_3 of the angular velocity (rad/s)

References

ABS Consulting Group, 2004, Consequence assessment methods for incidents involving releases from Liquefied Natural Gas carriers, Report # 80307, May 11 1981; August 15 1981. pp 1527-1532. Access: 9 Jun 2014.

AMERICAN BUREAU OF SHIPPING (ABS), Consequence Assessment Methods for Incidents Involving Releases from Liquefied Natural Gas Carriers. Washington, DC: 2004, May, 56 p. Technical Report to Federal Energy Regulatory Commission-FERC, 131-04 GEMS 1288209.

AMERICAN GAS ASSOCIATION (AGA). LNG Safety Program, Interim Report on Phase II Work. Arlington, VA: 1974,1973, Technical Report IS-3-1.

AMERICAN INSTITUTE OF CHEMICAL ENGINEERS (AIChE), Guidelines for Chemical Process Quantitative Risk Analysis. Center for Chemical Process Safety-CCPS, 2nd ed., 2000, 754 p., New York.

BEJAN, A., KRAUS, A.D., Heat Transfer Handbook. John Wiley & Sons, Inc., 2003, 1399 p., Hoboken, NJ.

BEYLER, C.L., Fire Hazard Calculations for Large, Open Hydrocarbon Fires. In: Handbook of Fire Protection Engineering. National Fire Protection Association-NFPA, Society of Fire Protection Engineering-SFPE, DiNenno, P.J. Editor, 3rd ed., 2002, Quincy, MA.

BIRD, R.B., STEWART, W.E., LIGHTFOOT, E.N. Transport Phenomena. John Wiley & Sons, Inc., 2nd ed., 2002, 895 p., New York.

BLACKWELL, B., SKAAR, H., Golar LNG: Delivering the World's first FSRUs, Golar LNG Ltd, Midwest Power Market Fundamentals, CERA, April, 2009, Hamilton, Bermuda.

BOPCHE, S. B., SRIDHARAN, A., Determination of view factors by contour integral technique, Annals of Nuclear Energy, Vol. 36, 11-12, Dec. 2009, 1681-1688.

BRITISH STANDARDS, BS 5908:1990, Replaced by BS 5908-1:2012, Fire and explosion precautions at premises handling flammable gases, liquids and dusts. Code of practice for precautions against fire and explosion in chemical plants, chemical storage and similar premises, December 2012. In: Lee's Loss Prevention in the Process Industries, Page 16/253, Third edition, Volume 1, Mannan, S., Ed. Elsevier Butterworth-Heinemann, Copyright 2005 Elsevier Inc. Inc. 3708 p. Volume 1 ISBN: 0.7506.7875.7

CANT, R.S., Direct Numeric Simulation of Premixed Turbulent Flames. Philosophical Transactions of the Royal Society London A, 357:3583-3604, 1999.

CANT, R.S., DAWES, W.N., SAVILL, A.M., Advanced CFD and Modeling of Accidental Explosions. Annual Review of Fluid Mechanics, 36:97-119, 2004.

CASSIDY, K., PANTONY, M. F., Major industrial risks - a technical and predictive basis for on and off site emergency planning in the context of UK legislation, Symposium Series No. 110, 1988, pages 75-95, Institute of Chemical Engineers, Hemisphere Publishing Corporation.

CANADIAN STANDARDS, CSA Z276-01, Canadian Standard for Liquefied Natural Gas (LNG) — Production, Storage, and Handling
Available:
http://shop.csa.ca/en/canada/petroleum-and-natural-gas-industry-systems/cancsa-z276-15/invt/27014702015
Access: 3 Jun 2016.

CODE OF FEDERAL REGULATION, 49 CFR 193, Liquefied Natural Gas Facilities: Federal Safety Standards, U.S. Department of Transportation, Pipeline and Hazardous Materials Safety Administration, Washington, D.C., October, 2011.
Available:
http://www.gpo.gov/fdsys/granule/CFR-2011-title49-vol3/CFR-2011-title49-vol3-part193
Access: 5 Mar. 2015.

CUMBER, P., Vessel Outflow Sensitivity to Composition, Journal of Loss Prevention in the Process Industries, 15 pp. 205–212, 2002.

DiNENO, P.J., Simplified radiation heat transfer calculations from large open hydrocarbon fires. Soc. Fire Protection Engrs., Ann. Mtg., 1982. In: In: Lee's Loss Prevention in the Process Industries, Page 16/253, Third edition, Volume 1, Mannan, S., Ed. Elsevier Butterworth-Heinemann, Copyright 2005 Elsevier Inc. Inc. 3708 p. Volume 1 ISBN: 0.7506.7875.7

EISENBERG, N.A., LYNCH, C.J., BREEDING, R.J., CG-D.136-75 and NTIS AD-015-245: Vulnerability Model: A Simulation System for Assessing Damage Resulting from Marine Spills. U.S. Coast Guard, 1975.

EUROPEAN COMMITTEE FOR STANDARDIZATION, EN 1473. Installation and Equipment for Liquefied Natural Gas – Design of Onshore Installations, Comité Européan Normalisation CEN 1997, 1997, 74 p.

ESTEVES, A. S.; CASADA, M., PAULA, H.M., REIS PARISE, J. A., International Standards and Regulations Pertinent to LNG Facilities (For Both Onshore and Offshore Applications), Definitions and Criteria for Evaluation of Exclusion and Safety Zones, June 2015.
Available: http://www.maxwell.vrac.puc-rio.br/Busca_etds.php?strSecao=resultado&nrSeq=25062@2
Access: June 3, 2016

ESTEVES, A. S.; REIS PARISE, J. A., Mathematical Modeling of Cryogenic Spills Onto Quiescent Sea Waters Followed by Pool Fires of Liquefied Natural gas (LNG). Applied Thermal Engineering, v. 59, n. 1-2, p. 587-598, 2013a.

ESTEVES, A. S.; REIS PARISE, J. A., Modeling of the Fluid Mechanics of Cryogenic Spills Onto the Sea and Radiation Fields from Subsequent Pool Fires During LNG Maritime Transportation, 22nd International Congress of Mechanical Engineering November 3-7, 2013b, Ribeirao Preto, SP, Brazil Copyright © 2013b by ABCM.

ESTEVES, A.S., Aspectos da cadeia de valor do GNL e modelagem matemática de derrames criogênicos e de incêndios em poça em seu transporte marítimo, PUC-Rio, Departamento de Engenharia Mecânica, Seminários de Doutorado, Disciplina MEC-2001/2002, 1.6. 2011.

ESTEVES, A.S. Mathematical Modeling of Cryogenic Spills and Pool Fires in the Liquefied Natural Gas (LNG) Maritime Transportation. Rio de Janeiro, 2010, 381 p. - PhD Thesis - Department de Mechanical Engineering, Pontifical Catholic University of Rio de Janeiro.
Available: http://www.maxwell.vrac.puc-rio.br/Busca_etds.php?strSecao=resultado&nrSeq=16726@2

Access: June 3, 2016
FAY, J.A., Model of spills and fires from LNG and oil tankers, J. Haz. Mat., 96 (2003) 171–188.
______, Model of Large Pool Fires. Journal of Hazardous Materials, B136:219-232, 2006.
______, Spread of Large LNG Pools on the Sea. Journal of Hazardous Materials, 140:541-551, 2007.
FEMA-Federal Emergency Management Agency, Handbook of Chemical Hazard Analysis Procedures, Publications Office, Washington DC, 1990, 520 p.
FERC, The Federal Energy Regulatory Commission, Notice of Availability of Staff's Responses to Comments on the Consequence Assessment Methods for Incidents Involving Releases from Liquefied Natural Gas Carriers. Washington, DC: Docket No. AD04-6-000, June 2004.
FINNEY, D. J., 1971**, Probit Analysis**, 3rd edition. London: Cambridge University Press. GEMS 1288209 to Federal Energy Regulatory Commission, Washington DC.
HESKESTAD, G., Fire Plumes, Flame Height, and Air Entrainment. In: Handbook of Fire Protection Engineering. National Fire Protection Association-NFPA, Society of Fire Protection Engineering-SFPE, DiNenno, P.J. Editor, 3rd ed., 2002, Section2:1-17, Quincy, MA.
______**.** Dynamics of the Fire Plume. Philosophical Transactions of the Royal Society London A, 356:2815-2833, 1998.
______. Luminous Heights of Turbulent Diffusion Flames. Fire Safety Journal, 5:103-1008, 1983.
HIGHTOWER, M., Suggestions on modeling LNG release from a ship, in: CLNG Workshop on LNG Pool Fire Modeling, Washington DC, 2007.
HISSONG, D.R., Keys to modeling LNG spills on water, J. H. Materials, 140 (2007) 465-477.
HOTTEL, H.C., Radiant-heat transmission, *Heat Transmission*, in Ch. 4 W. H. McAdams, McGraw-Hill, 3rd Ed., New York, 1954.
HOTTEL, H.C., SAROFIM, A.F., Radiative transfer. McGaw-Hill Book Company, New York, 1967, pp.520.
HOULT, D.P., **The Fire Hazard of LNG Spilled on Water**. Proceedings of the Conference on LNG Importation and Safety, 87, 1972a, Boston, MA.
______. **Oil Spreading on the Sea**. Annual Review of Fluid Mechanics, 4:341-368, 1972b
HOWELL, J. R.; MENGÜÇ, M. P., 2011, Radiative transfer configuration factor catalog: A listing of relations for common geometries. Journal of Quantitative Spectroscopy and Radiative Transfer, v. 112, n. 5, p. 910-912.
HYMES, I., The physiological and pathological effects of thermal radiation. U.K Atomic Energy Authority, Safety and Reliability Directorate, Culchetch, Warrington, SRD R 2715, 1983
ioMosaic Corp., Understand LNG Fire Hazards, An ioMosaic Corporation Whitepaper, Houston, Tex., 2007, 26 p**.**
JOHNSON, D.W., CORNWELL, J., Modeling the Release, Spreading, and Burning of LNG, LPG, and Gasoline on Water, Journal of Hazardous Materials, 140:535-540, 2007.
JUUL, N. H., 1982, View Factors in radiation between two parallel oriented cylinders of finite lengths. Journal of Heat Transfer, v. 104, n. 2, p. 384-388.
KAPLAN, W, Advanced Calculus, 2vol. 9th reprint, 2002.
KERN, D., Process Heat Transfer, McGraw-Hill Book Company, Inc., 1st Reprint, 1999, New York, NY.
KLETZ, T.A., Plant layout and location: methods for taking hazardous occurrences into account, Loss Prevention, 13, 147, (1980). In: Lee's Loss Prevention in the Process Industries, Page 16/253, Third edition, Volume 1, Mannan, S., Ed. Elsevier Butterworth-Heinemann, Copyright 2005 Elsevier Inc. Inc. 3708 p. Volume 1 ISBN: 0.7506.7875.7
KREISZIG, E., Advanced Engineering Mathematics, 8th ed. John Wiley & Sons, Inc., 1999, New York.
LAUTKASKI, R,. Validation of flame drags correlations with data from large pool fires. J Loss Prev. Process Ind. 5(3), 175-180, 1992.
LEHR, W.J., Foreword, my natural gas bias, J. H. Materials, 140 (2007) 411.
LEHR, W., SIMECEK-BEATTY, D., Comparison of Hypothetical LNG and Fuel Oil Fires on Water, Journal of Hazardous Materials, 107:3–9, 2004.
LUKETA-HANLIN, A. A Review of Large-Scale Spills: Experiments and Modeling. Journal of Hazardous Materials, (132):119-140, 2006.
MALVOS, H., RAJ, P.K., Thermal emission and other characteristics of large liquefied natural gas fires, Process Safety Progress. 26 (3) (September 2007) 237-247
MALVOS, H., RAJ, P.K., Details Of 35m Diameter LNG Fire Tests Conducted in Montoir, France In 1987 and Analysis of Fire Spectral and Other Data. The 2006 Spring National Meeting of the AIChE, Session T6005 LNG VI, Risk & Safety, Orlando, FL, April 2006.
MANNAN, M.S., CORMIER, B.R., LIAN, P., RANA, M., STARTZ, D., SUARDIN, J.A., WANG, J., ZHANG, Y., LNG pool fire modeling – White Paper, in: Mary Kay O'Connor Process Safety Center - **MKOPSC** (Ed.), LNG spread and pool formation considerations and models, Artie McFerrin Department of Chemical Engineering Texas A&M University System, College Station, Tex., 2008.
MANNAN, S., Lee's loss prevention in the process industries: Hazard identification, assessment and control. 3 Ed. USA: Elsevier Butterworth-Heinemann, 3708 p, 2005.
MARTINEZ, I., Radiative view factors. Disponível em:
http://webserver.dmt.upm.es/~isidoro/tc3/Radiation%20View%20factors.pdf
Access: 9 Jun 2014.
MECKLEMBURGH, J.C., (ed.) (1985). Process Plant Layout (London: Godwin). In: Lee's Loss Prevention in the Process Industries, Page 16/253, Third edition, Volume 1, Mannan, S., Ed. Elsevier Butterworth-Heinemann, Copyright 2005 Elsevier Inc. Inc. 3708 p. Volume 1 ISBN: 0.7506.7875.7
MELHEM, G. A., KALELKAR, A. S., OZOG, H., SARAF, S., "Managing LNG Risks: Separating the Facts from the Myths", ioMosaic Corporation white paper, 2006.
http://archives1.iomosaic.com/whitepapers/Managing%20LNG%20Risks.pdf.

MIZNER, G.A., EYRE, J.A., Large scale LNG and LPG pool fires, in: Proceedings of the Institution of Chemical Engineering Symposium, Series 71, Manchester, April, 1982.
MKOPSC, Mary Kay O'Connor Process Safety Center. Pool spreading description. In LNG Pool Fire Modeling White Paper, CLNG Workshop on LNG Pool Fire Modeling. Mary Kay O'Connor Process Safety Center, College Station, TX, September 2008.
MORTON, B.L., TAYLOR, G.I., TURNER, J.S. Proceedings of Royal Society London A, 234:1-23, 1956.
MOORHOUSE, D.J. Scaling Criteria Derived from Large Scale Experiments—the Assessment of Major Hazards. Institution of Chemical Engineers Symposium Series, 71:165–179, Manchester, UK, 1982a.
MOORHOUSE, D. J. Scaling criteria for pool fires derived from large-scale experiments. IChemE Symp. Ser. 71, 165-179, 1982b.
MOORHOUSE, D.J., PRITCHARD, M.J., Thermal Radiation Hazards from Large Pool Fires and Fireballs: a Literature Review. European Federation of Chemical Engineering 25, Institution of Chemical Engineers Symposium Series, 71:397–428, 1982, Manchester, UK.
MÖLLER, S.V., SILVESTRINI, J.H. Turbulência: Fundamentos. In: Cadernos de Turbulência - Turbulência Vol. 4. Anais da IV Escola de Primavera de Transição e Turbulência, IV EPTT, 231 p. ABCM, Pontifícia Universidade Católica do Rio Grande do Sul e UFRGS, Porto Alegre, RS, 2004.
MUDAN, K. S., Thermal radiation hazards from hydrocarbon pool fires. Progress in Energy and Combustion Science, v. 10, n. 1, p. 59 – 80, 1984.
MUDAN, K.S., Geometric View Factors for Thermal Radiation Hazard Assessment, Fire Safety Journal, 12, 2, pp. 89–96, 1987.
MUDAN, K.S., CROCE, P.A., Fire Hazard Calculations for Large Open Hydrocarbon Fires. In: Handbook of Fire Protection Engineering. National Fire Protection Association-NFPA, Society of Fire Protection Engineering-SFPE, 1st ed., 1988, Section 2, Quincy, Mass.
NFPA – National Fire Protection Association, Handbook of Fire Protection Engineering, Society of Fire Protection Engineering – SFPE, 2nd Ed., 1995, Quincy, Mass.
NFPA 59A-2006. Standard for the Production, Storage, and Handling of Liquefied Natural Gas (LNG), National Fire Protection Association, 1 Batterymarch Park, Quincy, MA, 02169-7471, 2006.
NOTARIANNI, K.A., EVANS, D.D., WALTON, W.D., MADRZYKOWSKI, D., LAWSON, J.R., Smoke Production from Large Oil Pool Fires. Proceedings of the Interflam 1993 Fire Safety International Fire Conference, Interscience Communications Ltd London, 111-119. March 1993, Oxford, UK.
NOVA SCOTIA DEPARTMENT OF ENERGY, Code of Practice for Liquefied Natural Gas Facilities, Version 1, July 13, 2005, July 2005,65 p.
Available:
http://energy.novascotia.ca/sites/default/files/Code-of-Practice-LNG-facilities.pdf
Access:
4 June 2016
OPSCHOOR, G., VAN LOO, R.O.M., PASMAN, H. J., Methods for calculation of damage resulting from physical effects of the accidental release of dangerous materials. In: International conference on hazard identification and risk analysis, human factors and human reliability in process safety, pages 21–32. Center for Chemical Process Safety, AIChE, 1992.
OPSCHOOR, G. The Spreading and Evaporation of LNG- and Burning LNG-Spills on Water. Journal of Hazardous Materials, 3:249-266, 1980.
OTTERMAN, A., Analysis of large LNG spills on water. Part 1: liquid spread and evaporation, Cryogenics (1975) 455-460.
PATEL, H., Emerging technologies for Natural Gas Importation, XXI Pan American Congress of Naval Engineering, ABS-American Bureau of Shipping, Montevideo, 2009.
PIOMELLI, U. Large-Eddy Simulation: Achievement and Challenges, Progress in Aerospace Sciences, 35(1-2):335-362, 1999.
PIETERSEN, C.M., Analysis of the LPG-incident in San Juan IXHUATEPEC, Mexico City, 19 November 1984, MT-TNO, ref. 85-0222, May 1985.
POPE, S.B., Computations on Turbulent Combustion: Progress and Challenges. Proceedings of The Twenty-Third Symposium (International) on Combustion, The Combustion Institute, Pittsburgh, PA, 591 p., 1991.
PRITCHARD, M.J., BINDING, T.M. FIRE2: A New Approach for Predicting Thermal Radiation Levels from Hydrocarbon Pool Fires. Institution of Chemical Engineers Symposium Series, 130:491-505, 1992.
PRUGH, R.W., Quantitative Evaluation of Fireball Hazards, Process Safety Progress, Vol. 13, No. 2, pp. 83-91, April 1994,The American Institute of Chemical Engineers.
QUEST CONSULTANTS, INC. Modeling LNG Spills in Boston Harbor, 2001, 2003. In: ABS CONSULTING GROUP. Consequence Assessment Methods for Incidents Involving Releases from Liquefied Natural Gas Carriers. Washington, DC: May 2004, 56 p. Technical Report to The Federal Energy Regulatory Commission-FERC, 131-04 GEMS 1288209.
QIAO, Y., WEST, H.H., MANNAN, M.S., JOHNSON, D.W., CORNWELL, J.B. Assessment of the Effects of Release Variables on the Consequences of LNG Spillage onto Water Using FERC Models. Journal of Hazardous Materials, 130:155-162, 2006.
RAJ, P. K., Large hydrocarbon fuel pool fires: Physical characteristics and thermal emission variations with height. Journal of Hazardous Materials, v. 140, n. 1-2, p. 280-292, 2007a.
RAJ, P.K., LNG Fires: a Review of Experimental Results, Models and Hazard Prediction Challenges. Journal Hazardous Materials, 140:444-464, 2007b.
RAJ, P.K., LNG Fire Spectral Data and Calculation of Emissive Power, Journal of Hazardous Materials, 142(3):720-729, 2007c.
RAJ, P.K., Large LNG Fire Thermal Radiation—Modeling Issues and Hazard Criteria Revisited, AIChE Process Safety Progress, 24 (3):192-202, September 2005.

RAJ, P.K., MUDAN, K.S., MOUSSA, A.N., Experiments Involving Pool and Vapor Fires from Spills of LNG on Water. Report #CG-D-55e79, NTIS AD077073, U.S. Coast Guard (USCG), Washington, DC, 1979, p. 20590

RAJ, P.K. Calculations of Thermal Radiation Hazards from LNG Fires - A Review of the State-of-the-Art, Paper presented at the AGA Transmission Conference, ST. Louis, Missouri, Paper number 2, Session 18, May 18, 1977.

RAJ, P.K., ATALLAH, S. Thermal Radiation from LNG Fires, Advances in Cryogenic Engineering, 20:143-150, 1974.

RAUSCH, A.H., EISENBERG, C.J., LYNCH, C.L., Continuing development of the Vulnerability model (VM2), Department of Transportation of the United States Coast Guard, Washington D.C., Report no. CG-D-53-77, February 1977.

SAGAUT, P., Large Eddy Simulation for Incompressible Flows. Springer-Verlag, 2001, Berlin/Heildeberg.

SCHNEIDER, A.L., et al., U.S. Coast Guard Liquefied Natural Gas Research at China Lake, Gastech 78. Monte Carlo, France, 5-8 October 1978.

SFPE-Society of Fire Protection Engineers, Assessing Flame Radiation to External Targets from Pool Fires, In: SFPE Engineering Guide, Bethesda, MD, 2002, 1999.

SHOKRI, M., BEYLER, C.L., Radiation from Large Pool Fires. SFPE Journal of Fire Protection Engineering, 1(4), pp. 141-150, 1989, DOI:10.1177/104239158900100404

SIEGEL, R., HOWELL, J.R., Thermal Radiation Heat Transfer, 4th ed. Taylor and Francis, 2001, New York.

SILVA, L.F.S. Combustão e Turbulência. In: Cadernos de Turbulência - Turbulência Vol. 4. Anais da IV Escola de Primavera de Transição e Turbulência, IV EPTT, 231 p., ABCM 2004, Pontifícia Universidade Católica do Rio Grande do Sul e UFRGS, 27 de setembro a 1º de outubro de 2004, Porto Alegre, 2004.

SILVEIRA NETO, A.S. Fundamentos da Turbulência nos Fluidos, in: Cadernos de Turbulência – Turbulência Vol. 1. Anais da I Escola de Primavera de Transição e Turbulência, I EPTT, 272 p., ABCM 2002, Instituto Militar de Engenharia, 21 a 25 de setembro, Rio de Janeiro, 1998.

SLATTERY, J.C., Momentum, Energy, and Mass Transfer in Continua, McGraw-Hill Kogakusha, 1972, Tokyo.

SPARROW, E.M., A New Simpler Formulation for Radiative Angler Factors, Journal of Heat Transfer, ASME, 85, pp. 81–88, 1963.

SPARROW, E.M.J., CESS, R.D., Radiation Heat Transfer (Augmented Ed.). Hemisphere Publishing Corporation, Washington DC, 1978.

SNL (SNL National Laboratories), M.M. Hightower, L. Gritzo, A. Luketa-Hanlin, J. Covan, S. Tieszen, G. Wellman, M. Irwan, M. Kaneshige, B. Melof, C. Morrow, D. Ragland, Guidance on Risk Analysis and Safety Implications of a Large Liquefied Natural Gas (LNG) Spill Over Water, Report N° SAND2004-6258, December 2004 for the U.S. Department of Energy's National Nuclear Security Administration under Contract DE-AC04-94AL85000, Albuquerque, New Mexico and Livermore, Cal., 2004.

SNL-Sandia National Laboratories, Luketa-Hanlin, A., Hightower, M. M., Attaway, S., Breach and Safety Analysis of Spills Over Water from Large Liquefied Natural Gas Carriers, Report № SAND2008-3153, May 2008, for the U.S. Department of Energy's National Nuclear Security Administration under Contract DE-AC04-94AL85000, Albuquerque, New Mexico and Livermore, Cal., 2008a.

SNL-Sandia National Laboratories, Luketa-Hanlin, A., Hightower, M., On the Evaluation of Models for Hazard Prediction for Liquefied Natural Gas (LNG) Spills on Water, Albuquerque, NW, 2008b.

SNL-Sandia National Laboratories, Luketa, A., Recommendations on the Prediction of Thermal Hazard Distances from Large Liquefied Natural Gas Pool Fires on Water for Solid Flame Models, Report N° SAND2011-9415, December 2011, for the U.S. Department of Energy's National Nuclear Security Administration under contract DE-ACD4-94AL85000, Washington, DC, December, Albuquerque, New Mexico and Livermore, Cal., 2011.

STEWARD, F.R., Prediction of the Height of Turbulent Diffusion Buoyant Flames. Combustion Science and Technology, 2:203–212, 1970.

TIESZEN, S.R., NICOLETTE, V.F., GRITZO, L.A., HOLEN, J.K., MURRAY, D., MOYA, J.L., Vertical structures in pool fires: Observation, Speculation, and Simulation, SNL National Laboratories, Albuquerque, NM, SAND96-207, November 19, 1996.

THOMAS, P.H., The size of flames of natural fires, Ninth Symposium on Combustion, Academic Press, New York, p. 844-859, 1963.

THOMAS, P.H., Fire spread in wooden cribs: Part III, The effect of wind. Boreham Woods, England: Fire Research Station, June 1965, Fire Research Note No. 600.

TMS-Technology & Management Systems, Inc., Spectrum of Fires in a LNG Facility - Assessments, Models and Consideration in Risk Evaluations. Burlington, Mass. The U.S. Department of Transportation Pipeline & Hazardous Materials Safety Administration, 2006, Final Technical Report, 99 p.

The Netherlands Organization of Applied Scientific Research (TNO), Methods for the calculation of physical effects (TNO "Yellow Book"), Eds.: C.J.H. van den Bosch and R.A.P.M Weterings, Third edition, The Hague, The Netherlands, 1st Print 1997, 2nd Print 2005, The Hague, pp.3.1-3.126.

The Netherlands Organization of Applied Scientific Research (TNO), Methods for the determination of possible damage to people and objects resulting from releases of hazardous materials (TNO "Green Book"), CPR 16E, Eds: C. J. H. van den Bosch et al., The Hague, 1992.

U.S. 49 CFR 192 Sub Parts 2057 and 2059, Transportation of Natural and Other Gas by Pipeline: Minimum Federal Safety Standards. October 1, 2011.
Available:
http://www.gpo.gov/fdsys/granule/CFR-2011-title49-vol3/CFR-2011-title49-vol3-part192
Access: 5 Mar. 2015.

U.S. DOT 49 CFR Part 193, Liquefied Natural Gas Facilities: Federal Safety Standards, U.S. Department of Transportation, Pipeline and Hazardous Materials Safety Administration, Washington, D.C., October, 2011.
Available:

http://www.gpo.gov/fdsys/granule/CFR-2011-title49-vol3/CFR-2011-title49-vol3-part193
Access: 5 Mar. 2015.
USCG 33 CFR 165.30, 20 - Regulated Navigation Areas and Limited Access Areas, U.S. Coast Guard, U.S. Department of Homeland Security
Available:
http://www.gpo.gov/fdsys/granule/CFR-2010-title33-vol2/CFR-2010-title33-vol2-part165
Access: 3 Mar. 2015.
WARNATZ, J., MAAS, U., DIBBLE, R. W. Combustion – Physical and Chemical Fundamentals, Modeling and Simulation, Experiments, Pollutant, Formation, 2nd ed. 1999, Springer-Verlag, Berlin/Heidelberg.
WAYNE, F. D., An economical formula for calculating atmospheric infrared transmissivities. Journal of Loss Prevention in the Process Industries, v. 4, n. 2, p. 86 – 92, 1991.
WELKER, J. L.; SLEIPCEVICH, C. M, Bending of wind-blown flames from liquid pools, Fire Technol., 2, p. 127, 1966.
WIEBELT, J. A.; RUO, S. Y., Radiant-interchange configuration factors for finite right circular cylinder to rectangular planes. International Journal of Heat and Mass Transfer, v. 6, n. 2, p. 143-146, 1963.
WILLIAMS, F.A. Combustion Theory: The Fundamental Theory of Chemically Reacting Flow Systems (Combustion Science & Engineering). 2nd ed. Benjamin/Cummings Publishing Company, Inc., 680 p., 1985, San Francisco, Cal.
WOODWARD, J. L.; PITBLADO, R. M., LNG Risk Based Safety - Modeling and Consequence Analysis, Wiley and AIChE, 2010, pp. 374.
WORLD BANK (The World Bank), 1988, Techniques for assessing industrial hazards: A manual, World Bank Technical, Paper Number 55, ISBN 0253-7454, the International Bank for Reconstruction and Development, 1818 H Street, NW, Washington, D.C. 20433, 1988.
XIAO, H., GOLLNER, M.J., ORAN, E.S., From fire whirls to blue whirls and combustion without pollution, Departments of Aerospace Engineering and Fire Protection Engineering, University of Maryland, College Park, Paper ssubmitted on 4 May 2016, Ed. Cornell University Library.
Available in: https://arxiv.org/abs/1605.01315. Access: 23 Feb. 2017
ZUKOSKI, E.E., Properties of Fire Plumes. In: Combustion Fundamentals of Fire, G. Cox Editor, 101–219, Academic Press, 1995, London.

Revision 2 – Approved for issue
November 26, 2017

AE/JAP/AC/EC/ae

…oo0oo…